NASA Contractor Report 174900

Iron-Rich Low-Cost Superalloys

(NASA-CR-174900) IRON RICH LOW COST SUPERALLOYS Ph.D. Thesis. Final Report (Connecticut Univ.) 169 p HC A08/MF A01 CSCL 11F
N85-26962
Unclas
G3/26 21336

Steven F. Wayne

The University of Connecticut
Storrs, Connecticut

May 1985

Prepared for
Lewis Research Center
Under Grant NAG 3-271

National Aeronautics and
Space Administration

IRON-RICH LOW-COST SUPERALLOYS

Steven Falko Wayne, Ph.D.

The University of Connecticut, 1985

An iron-rich low-cost superalloy has been developed in conjunction with United Technologies Research Center under the NASA program, Conservation of Strategic Aerospace Materials. The alloy, when processed by conventional chill casting, has physical and mechanical properties that compare favorably with existing nickel and cobalt-based superalloys while containing significantly lower amounts of strategic elements. The composition of the alloy is Cr(15)-Mn(15)-Mo(2)-C(1.5)-Si(1.0)-Nb(1.0)-Fe(bal.), and it can be produced with chromite ore deposits located within the United States.

Studies were also made on the properties of Cr(20)-Mn(10)-C(3.4)-Fe(bal.), a eutectic alloy processed by chill casting and directional solidification (D.S.) which produced an aligned microstructure consisting of M_7C_3 fibers in an γ-Fe matrix. This good alignment vanishes when molybdenum or aluminum is added in higher concentrations. Thermal expansion of the M_7C_3 (M=Fe, Cr, Mn) carbide lattice was measured up to 800° C and found to be highly anisotropic, with the a-axis being the predominant mode of expansion.

Repetitive impact-sliding wear experiments performed with the Fe-rich eutectic alloy showed that the directionally solidified microstructure greatly improved the alloy's wear resistance as compared to the chill-cast microstructure and conventional nickel-base superalloys.

Studies on the molybdenum cementite phase have proven that the crystal structure of the ξ phase is not orthorhombic. The molybdenum cementite has a monoclinic cell (space group C2/m) a=10.870, b=7.761, c=6.563 Å and β=120.1° with a volume approximately one-fourth the size of the previously proposed cell. The crystal structure of the ξ phase is made up of octahedra building elements consisting of four Mo and two Fe-atoms and trigonal prisms consisting of four Fe and two Mo-atoms. The voids are occupied by carbon atoms. The previous chemical formula for the molybdenum cementite "$MoFe_2C$" is now clearly seen to be $Mo_{12}Fe_{22}C_{10}$.

FOREWORD

This dissertation topic was conceived by Professor Hans Nowotny who provided me with the inspiration and technical support to make this work possible. His personal commitment to my education will always be cherished.

The cooperation of Drs. David D. Pearson and Frank Lemkey of United Technologies Research Center, who both shared in the alloy development task, is greatly appreciated. The support of Dr. Joseph Stephens, the COSAM program manager at NASA-Lewis Research Center, is gratefully acknowledged. I also wish to thank Dr. Tom Buljan of GTE Laboratories for providing me with encouragement during the final stages of the dissertation.

The portion of this work regarding the crystal structure of molybdenum cementite was made possible by the contributions of Mr. Lewis Schmidt, Mr. Cliff Schuman, Dr. Paul Moews, Professor Edward Kostiner and, especially, Mr. Mike Rapposch.

I am also thankful for the input from Professors Arthur McEvily and Stephen Rice, which enriched the quality of the thesis.

TABLE OF CONTENTS

IRON-RICH LOW-COST SUPERALLOYS

I. Introduction

Over the last thirty years, successful development of high-strength nickel and cobalt-based superalloys has met the needs of the automotive and aerospace industry. For this reason, there has been little interest in developing iron-base alloys for the higher temperature gas turbine engine components [1]. However, there is an increasing awareness of the United States' dependency on imported elements used in cobalt-based superalloys. For example, the aircraft engine industry relies heavily on cobalt, chromium, columbium and tantalum. Today, we are almost totally dependent on foreign sources for these elements, and many supply interruptions resulting from political disturbances in many countries have been experienced [2]. In order to reduce the U. S. dependence on these so-called strategic elements, NASA has formed COSAM (Conservation of Strategic Aerospace Materials). A joint program (under COSAM) has been established involving the University of Connecticut, United Technologies Research Center and NASA-Lewis Research Center. This program provides the impetus for investigation into cast and aligned eutectic iron-based superalloys. The role of each program member is shown in Figure 1 and allows for interaction between UCONN and the facilities of UTRC and NASA.

The potential for the aligned Fe-Cr-Mn-Al-C alloys to substitute for "strategic" superalloys has been determined by Lemkey et al. [3]. Figure 2 shows stress to rupture life for the alloy Fe-20Cr-10Mn-3.2C which compares favorably with other current Fe, Co and Ni based superalloys [1]. Interestingly, modification of this iron-based superalloy

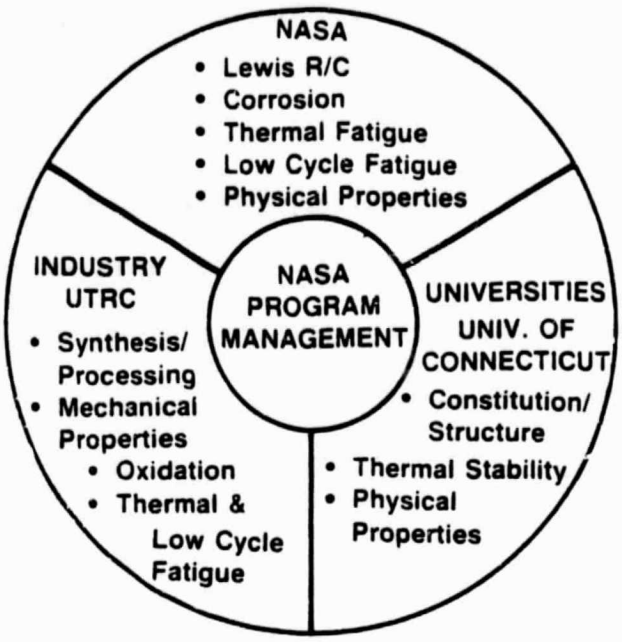

Fig. 1 The Roles of the Participants in the Cooperative Iron-Base Alloy Development Program [1]

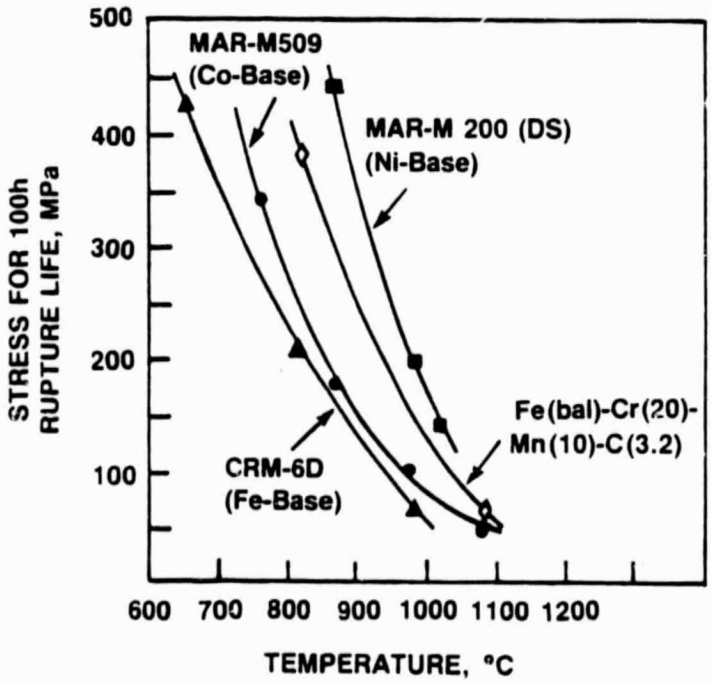

Fig. 2 Rupture Stress vs. Temperature Data for Iron-, Nickel- and Cobalt-Based Superalloys [1]

is also envisioned as a candidate material for Stirling engine cylinder and regenerator housing components which furthermore require the alloy to have a good hydrogen compatibility.

The purpose of this investigation was to evaluate the constitution of iron-based superalloys. The alloy development task was shared with UTRC, where alloy synthesis and mechanical properties were performed. This dissertation, by determining the constitution of each new alloy, evaluated the role of alloying elements on phase stability. The alloy selections are made from the multicomponent system, Fe-Cr-Mn(Mo)-Al(Si)-C(N), which is aimed towards an austenitic iron solid solution matrix reinforced by finely dispersed or aligned carbide phases. It should be mentioned that the Cr additions to this alloy system can be obtained from chromite ore deposits located in the western part of the United States [4]. The alloy iteration flow chart is shown in Figure 3 and is designed to identify a substitute low-cost iron-based superalloy, containing low quantities of strategic elements [5].

The second chapter of this dissertation which relates to the alloy development task, concentrates on the Fe-Mo-C system and structural-chemical aspects of the molybdenum cementite, the so-called ξ carbide that is a frequently occurring phase in the multi-component iron alloys.

The final part of this dissertation focuses on the Fe(bal)-Cr(20)-Mn(10)-C(3.4) eutectic superalloy processed by means of directional solidification. The M_7C_3 carbide phase stability, microhardness, thermal expansion and crystallographic relation to the gamma iron matrix was determined. Furthermore, impact-sliding wear tests were done with the eutectic superalloy to compare the chill cast and aligned microstructural conditions.

Fe-Mn-Cr-Al-C ALLOY ITERATION FLOW CHART

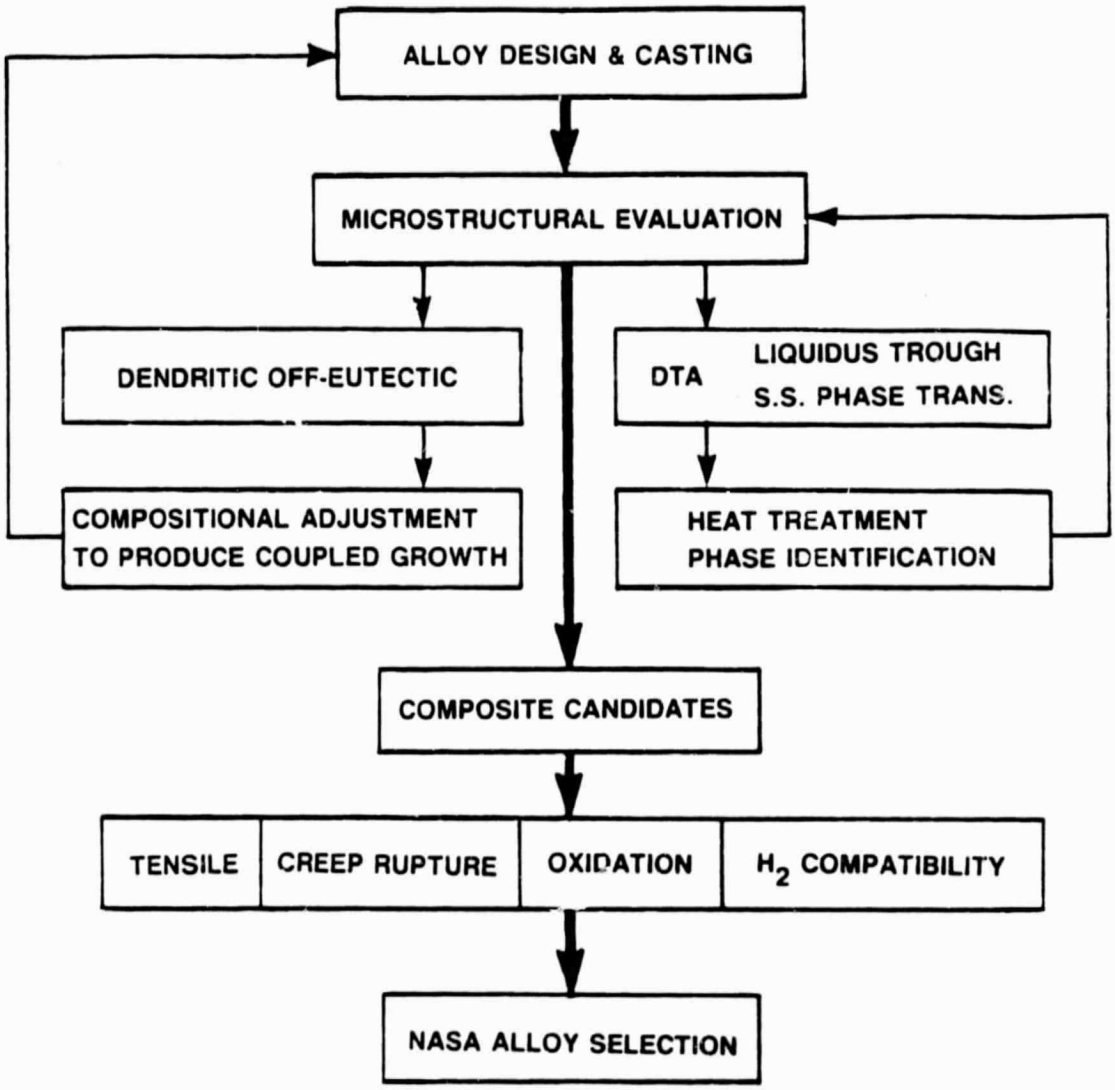

Fig. 3 Alloy Development Flow Chart [5]

II. Review of the Literature

A. Background

A major goal in the development of a low-cost iron-base superalloy is characterization of the metallic and carbide-phase stabilities. It is the aim of this investigation to achieve a duplex structure which contains an austenitic matrix (γ-phase) and an M_7C_3 carbide. In many cases, aligned eutectics are produced with the M_7C_3 as an aligned carbide phase [3,6], and are termed in situ composites. The importance of phase stability for Fe-Co-Cr-C aligned eutectics was seen by van den Boomgaard when the ultimate tensile stress dropped at 900°C (after an anneal at 950°C) due to the transformation of the M_7C_3 carbide into the $M_{23}C_6$ carbide [6].

B. Fe-Mn-C and Fe-Cr-C Systems

It is well known from previous investigations that the binary metal {Fe,Mn,Cr}-carbon systems and the ternaries have a strong tendency for carbide formation [3]. Isothermal sections have been calculated from thermochemical data based on the assumption of regular solid solutions of the carbides: $(Fe,Mn)_{23}C_6$; $(Fe,Mn)_3C$; $(Fe,Cr)_{23}C_6$, $(Fe,Cr)_3C$ and $(Fe,Cr)_7C_3$ [7,8]. Figure 4 contains isothermal sections of the Fe-Mn-C system at 600°C and 1100°C. The main observation is that the $\gamma + M_3C + M_{23}C_6$ phases are shifted to increased amounts of Mn at the higher temperature. At about 1000°C, the M_3C forms as a complete series of solid solutions between Fe_3C and Mn_3C, with the $Fe_{\sim 2}Mn_{\sim 1}C$ phase detected by Shimma [9]. The M_7C_3 carbide does not coexist with the M_3C between 600 and 1100°C because of the presence of the $(Fe,Mn)_5C_2$ carbide which has a large range of Mn/Fe substitution [10,11].

Studies in the Fe-Cr-C system, up to 1 w%C and 29 w%Cr, have found $M_{23}C_6$, M_3C and M_2C_3 to be stable carbides [12]. Furthermore, the $M_{23}C_6$ is in equilibrium with α and γ, whereas M_3C and M_7C_3 exist with γ only. These carbides are stoichiometric with the exception of the cementite phase $(Fe,Mn)_3C$ in the Fe-Mn-C system [13]. The transformation behavior of M_7C_3 to $M_{23}C_6$ and M_3C to M_7C_3 has been examined in a high carbon chromium steel [14,15]. In these systems, the Cr_7C_3 is a highly stable phase; however the Fe_7C_3 has been shown to be metastable [16]. The Mn_7C_3 carbide has a stability which can be placed between chromium and iron carbides.

A recent application of the chromium carbide stability has been applied to the development of aligned eutectic microstructures [17,18,19]. These composite materials are formed <u>in situ</u> and consist of a solid solution matrix reinforced with the directionally solidified carbide phase. Thus considerable attention must be paid to the eutectic equilibrium, which is shown in Fig. 5 for an isopleth taken at 17% Cr [3]. Just above 1200°C, at 3-4 wt.% carbon, exists the monovariant eutectic trough which couples the M_7C_3 and γ phases.

C. <u>Carbon-Free Fe-Cr-Mn Alloys</u>

In order to develop an alloy with a γ phase matrix, the equilibria between the metallic phases have to be established first. Kirchner et al. have examined the ferrite-austenite equilibrium for the temperature range of 750°C to 950°C [20]. Figure 5 contains the isothermal sections from the Fe-Cr-Mn system taken at 700°C and 1000°C [3]. Solid solution formation between the σ phases was proposed by Potůček [21] and the presence of $\gamma + \sigma$ phase in Fe rich Fe-Cr-Mn alloys at 650°C was evidence for continuous transition regions. The work of Lemkey et al. [3] established that there is a homogeneous transition region between σ(Fe-Cr)

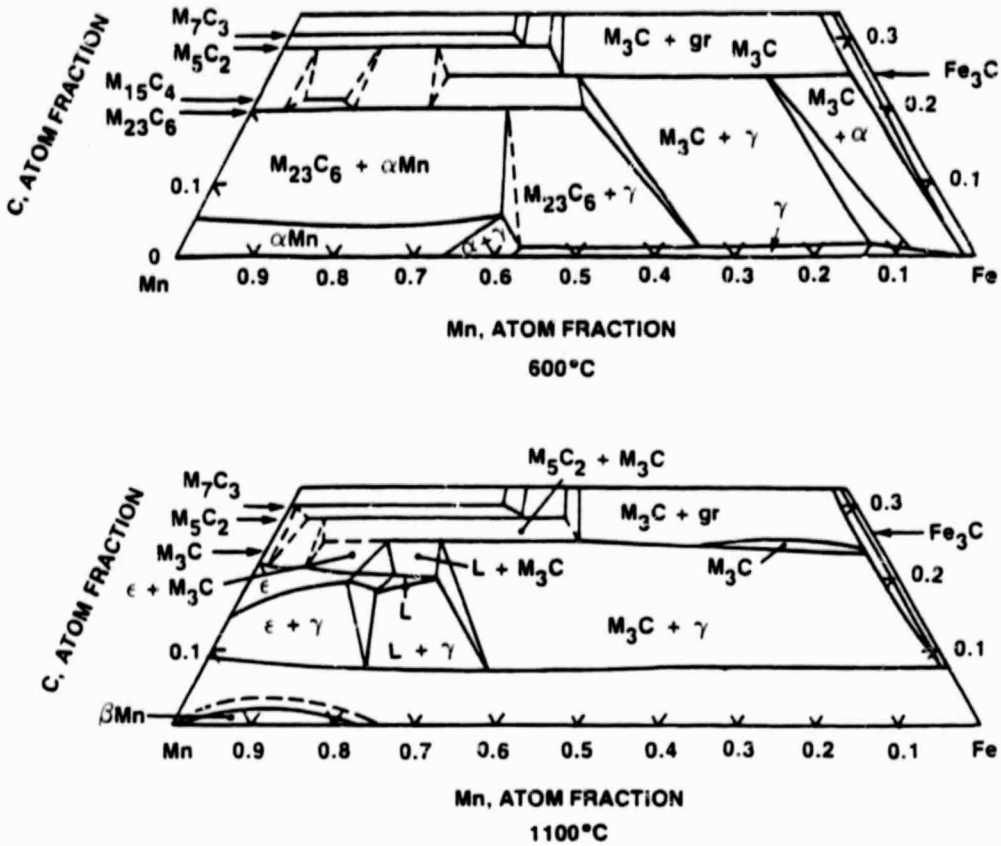

Fig. 4 Isothermal Sections of Fe-Mn-C System Taken at 600°C and 1100°C [13]

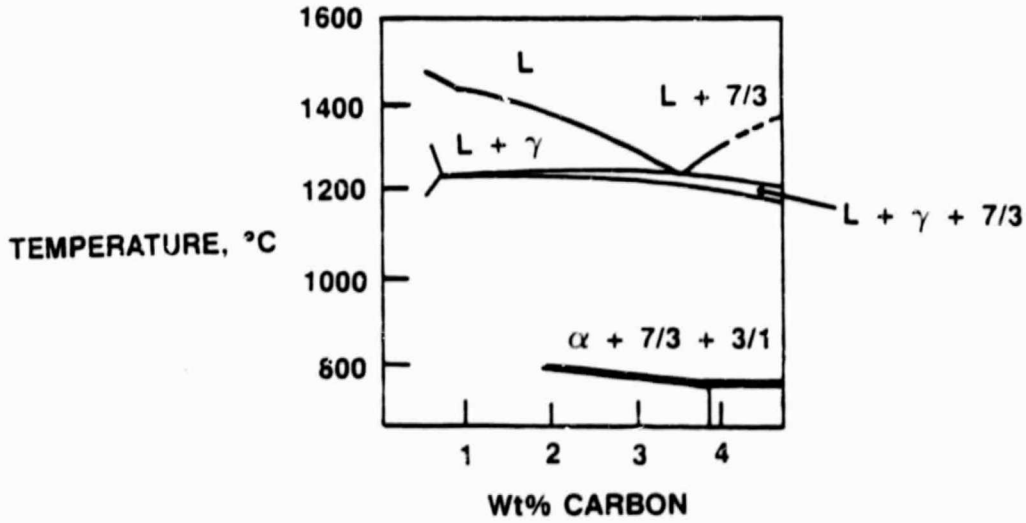

Fig. 5 Section of Fe-Cr-C Phase Diagram (Isopleth) Taken at 17% Cr [3]

and σ(Mn-Cr) phases in which the lattice parameters change in a fairly linear fashion. At 1000°C, the Fe-Cr-Mn system reveals that the γ phase is readily stabilized by small additions of Mn. Lowering the temperature to 700°C (Fig. 6) alters the equilibria; a higher amount of Mn (ca 10%) is needed to stabilize the γ phase. Then, γ occurs up to 60 a/o as a single phase. Interestingly, the Cr addition by itself does not stabilize the γ-Fe at 700°C. The result of this is that Cr becomes a strong carbide former.

D. Fe-Mo-C System and the ξ Carbide

The constitution of the binary systems Fe-C, Mo-C and Fe-Mo are now well known [22,23,24]. The earliest work on the ternary system was done by Takei, who found M_6C and cementite (Fe_3C) at 700°C [25]. Kuo showed that MC, M_2C and $M_{23}C_6$ were also stable at 700°C and by annealing he discovered the ξ molybdenum-iron carbide (molybdenum cementite) [26]. The work of Satô confirmed the ξ carbide and $M_{23}C_6$ after 500 hr anneal at 700°C [27].

There is good agreement that iron or iron-solid solutions coexist with Mo_2C at 700 and 1000°C [27-30]. The first partial system, Fe-Mo-Mo_2C, has been explored by Fraker et al. [31] and Ettmayer et al. [32] who found an η carbide having a composition around Fe_3Mo_3C. In contrast to Bowman et al. [28] and Aldén et al. [29] who at 700°C find the existence of one ternary carbide, Sato et al. [24] report the occurrence of two ternary carbides (the ξ carbide and the τ carbide). The latter is the metastable τ carbide which has an ordered $Cr_{23}C_6$ type, structure [27]. According to the phase diagram established by Jellinghaus [33], the ξ carbide (frequently named $MoFe_2C$) is the stable ternary phase below 700°C. At 1000°C, Campbell et al. [34] describe both τ and ξ

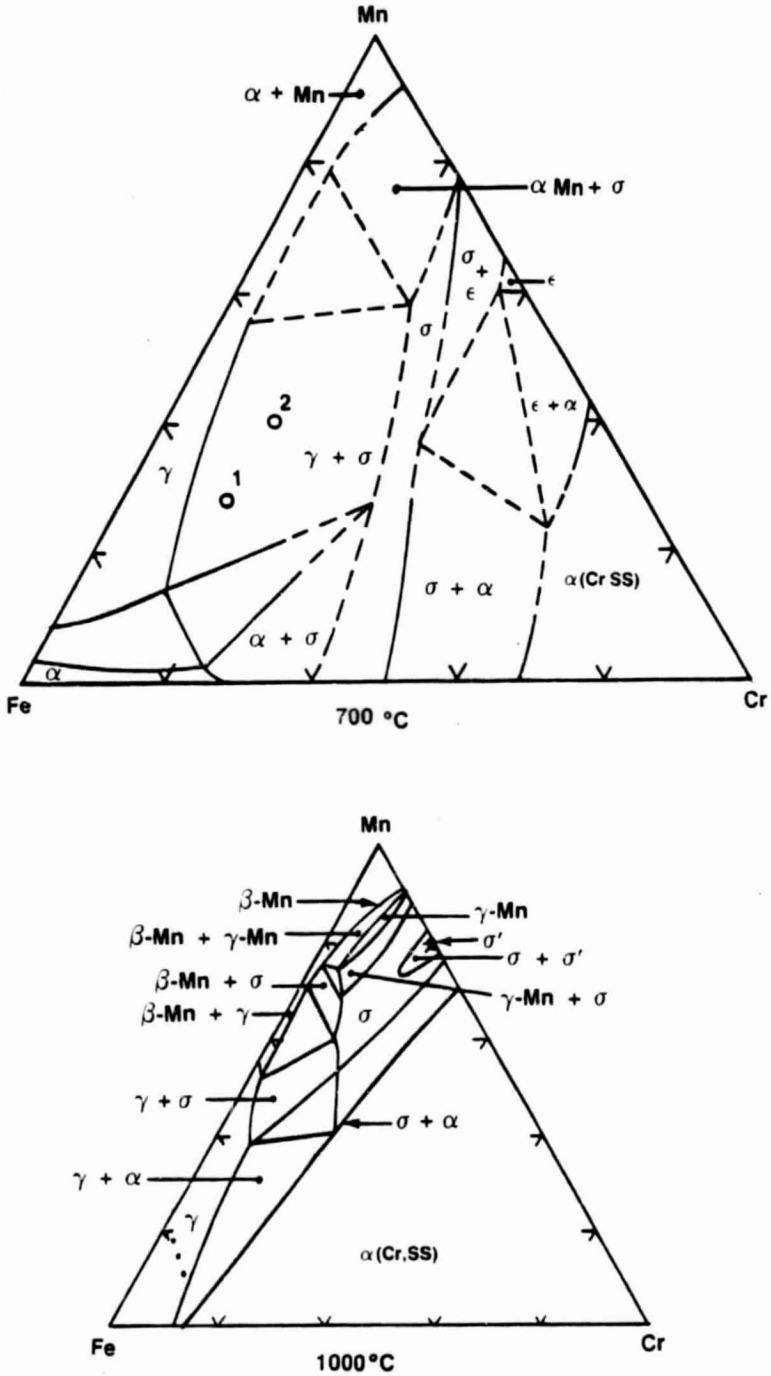

Fig. 6 Isothermal Sections of Fe-Cr-Mn Taken at 700°C and 1000°C [31]

carbide phase as stable while Bungardt et al. [35] and Harvig et al. [30] indicate $MoFe_2C$ is the only stable phase. The work by Nishizava [36], and Wada et al. [37] at 900°C and 1000°C indicates Fe_3C, $MoFe_2C$, M_2C and M_6C as stable phases, although Bungardt did not detect the M_2C carbide at 1000°C or 1100°C [35]. Recent work has shown that formation of $MoFe_2C$ proceeds easily by sintering but vanishes in arc-melted samples, only to return after anneal (300 h, 1000°C) [38]. Molybdenum cementite has been observed directly in a molybdenum modified AISI 4130 steel; the kinetics of the carbide precipitation was recently discussed in detail [39]. According to this investigation, the presence of the ε phase can easily be missed in low-alloy steels because of the tiny particle size and the structural similarity of the powder pattern to Fe_3C. It is clear that due to the metastable equilibria of the phases in the Fe-Mo-C system inconsistencies exist in the reported literature.

E. Fe-Cr-Mo-C System

An investigation of this system with carbon contents up to 2.5 wt.% at 1100°C has been performed by Staska et al. [40] who report the occurrence of the carbides M_6C, $M_{23}C_6$, M_3C, M_7C_3 and $MoFe_2C$. When the carbon content is increased to 3 wt.%, and particularly when molybdenum increases to 10 wt.%, the M_6C (η carbide) becomes predominant [41]. These authors express the opinion that the molybdenum cementite appears to have a composition closer to the η carbides. Some interesting quantitative data were also given for the metal-metal substitution in the M_7C_3 carbide in which 13 wt.% Mo, 22-43 wt.%Cr were found in $(Fe,Cr,Mo)_7C_3$. Two 4-phase spaces at 1100°C were determined (γ + M_6C +M_3C + M_7C_3) and (γ + M_6C + $M_{23}C_6$ + M_7C_3) for the region 12 wt.%Cr, 14wt.%Mo and 2.5 wt.%C [40]. Bungardt et al. have studied the γ unit cell behavior as Mo content varied in low carbon steels and found $M_{23}C_6$, M_6C and ferrite.

F. Fe-Cr-Mn-C System and Eutectic Equilibria

Based on the eutectic equilibria in the Fe-Cr-C system [42], literature data on the ternaries, the work of Gupta [43] and new results, Lemkey et al. have proposed an Fe-Cr-Mn-C phase diagram shown in Fig. 7. The addition of Mn to the 3 wt.% Fe-Cr-C system is seen to mainly stabilize the γ phase field. This figure shows, with a dotted line, the projection of the monovariant trough on the isothermal section at 1000°C in the γ + 7/3 phase field. The eutectic point is seen to move with increasing amounts of Mn.

Based on the observation that Mn acts as a γ stabilizer, the primary and secondary crystallizations within 30 wt.% Cr + Mn and up to 4 wt.% carbon will mainly depend on competition between the M_7C_3 and M_3C carbides. The M_3C carbide, in the Fe-Cr-Mn-C system occurs as cementite $(Fe,Mn)_3C$ and $(Fe,Cr)_3C$ [3]. Interestingly, the M_3C carbide which forms at 1000°C, changes to $M_{23}C_6$ after annealing at 700°C to form $Fe_{11.5}Mn_{8.6}Cr_{2.9}C_6$. Also of interest is the presence of $M_{23}C_6$ carbides which occur with increased amounts of chromium. Lemkey et al. have also investigated the $M_{23}C_6$ section (M = Fe,Mn,Cr) at 800°C which is shown in Figure 8. There is good evidence here that chromium additions stabilize the M_7C_3; however, at high concentrations the $M_{23}C_6$ carbide coexists. The M_7C_3 to $M_{23}C_6$ transformation was also the subject of a detailed investigation by Beech et al. [14].

G. Fe-Cr-Mn-Mo-C System

Gupta has explored this quinary system at 50 at.% Fe and 30 at.% carbon at 700°C, 1000°C and 1100°C [43] with strong emphasis on the M_7C_3 carbide. The isothermal M_7C_3 (M = Fe,Cr,Mn,Mo) sections are shown in Figures 9, 10, and 11 and show that in the carbide, chromium can be

readily substituted by Fe and Mn. Molybdenum, on the other hand, favors the competing M_2C carbide and Gupta determined the maximum solubility of Mo in M_7C_3 to be $M_{6.5}Mo_{0.5}C_3$ (M = Fe,Cr,Mn).

The role of molybdenum is further seen in Figures 9-11 with the frequent occurrence of the molybdenum cementite. Based on a large number of samples, Gupta observed that Mo-cementite occurred more frequently in the sintered than arc-melted state and exhibited a narrow but detectable homogeneous range in the presence of manganese and chromium. The ξ phase was found to dissolve up to 10 mole % chromium carbide and 20 mole % manganese carbide with 50 at.% Fe.

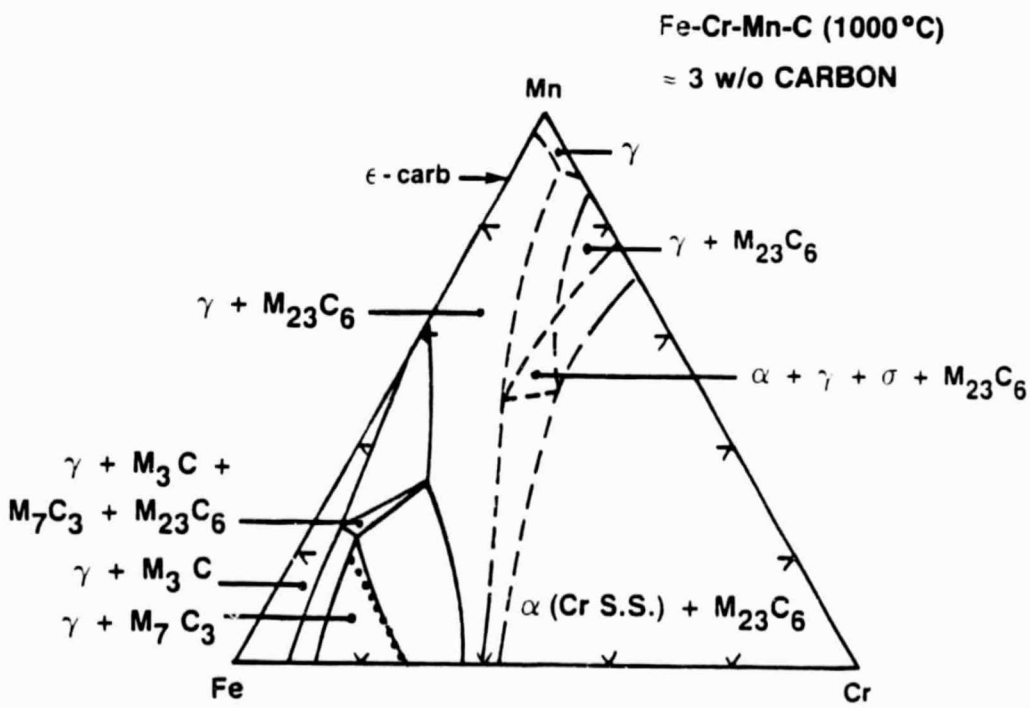

Fig. 7 Isothermal Section of Fe-Cr-Mn-C at 1000°C, ~3 wt.% Carbon [3]

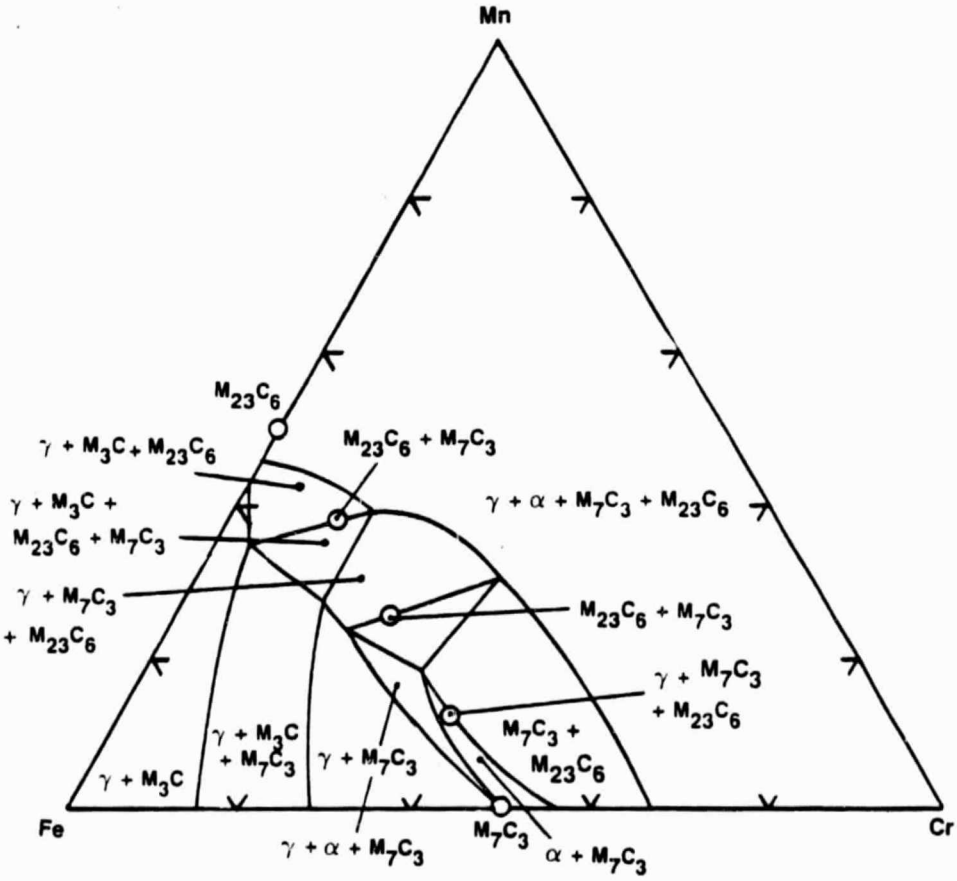

Fig. 8 Isothermal Section for Nominal Composition of $M_{23}C_6$ (M = Fe,Cr,Mn) at 800°C [43]

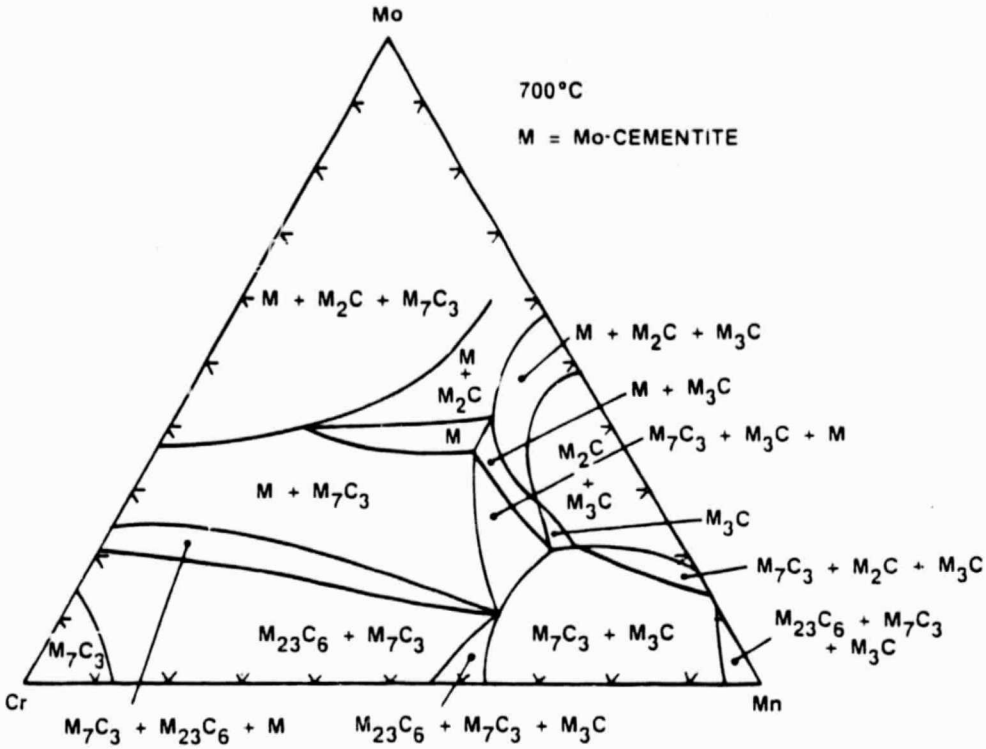

Fig. 9 Isothermal Section for Nominal Composition of M_7C_3 (M = Fe,Cr,Mn,Mo) After Arc Melting and Annealing at 700°C for 170 Hours [43]

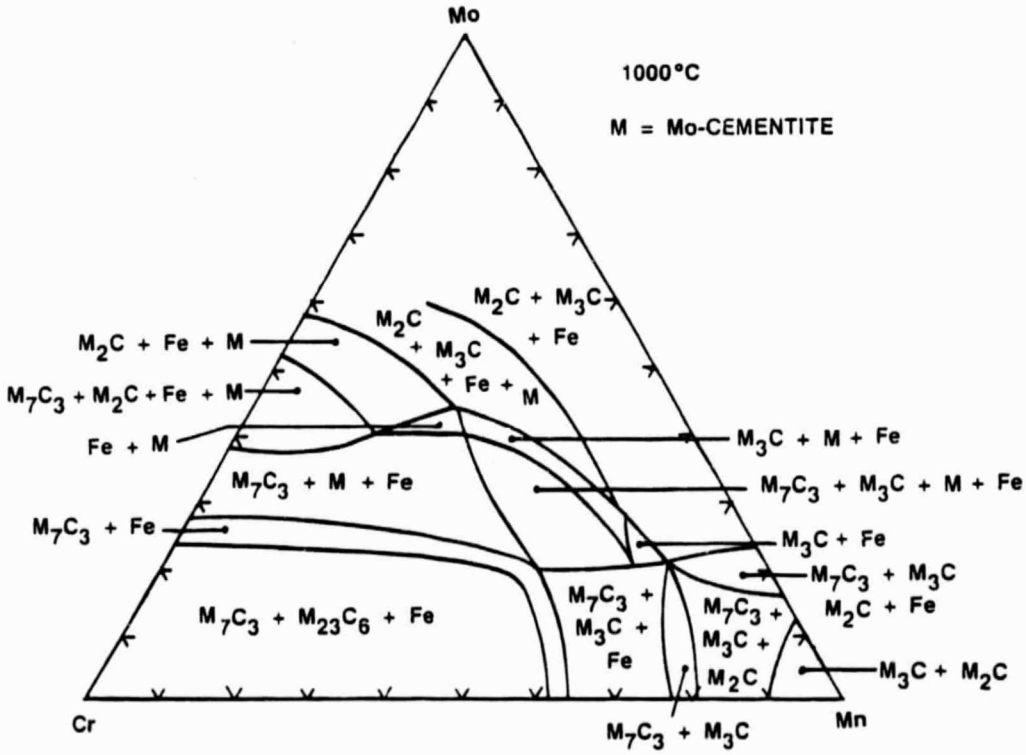

Fig. 10 Isothermal Section as Figure 9, 1000°C Anneal for 50 Hours [43]

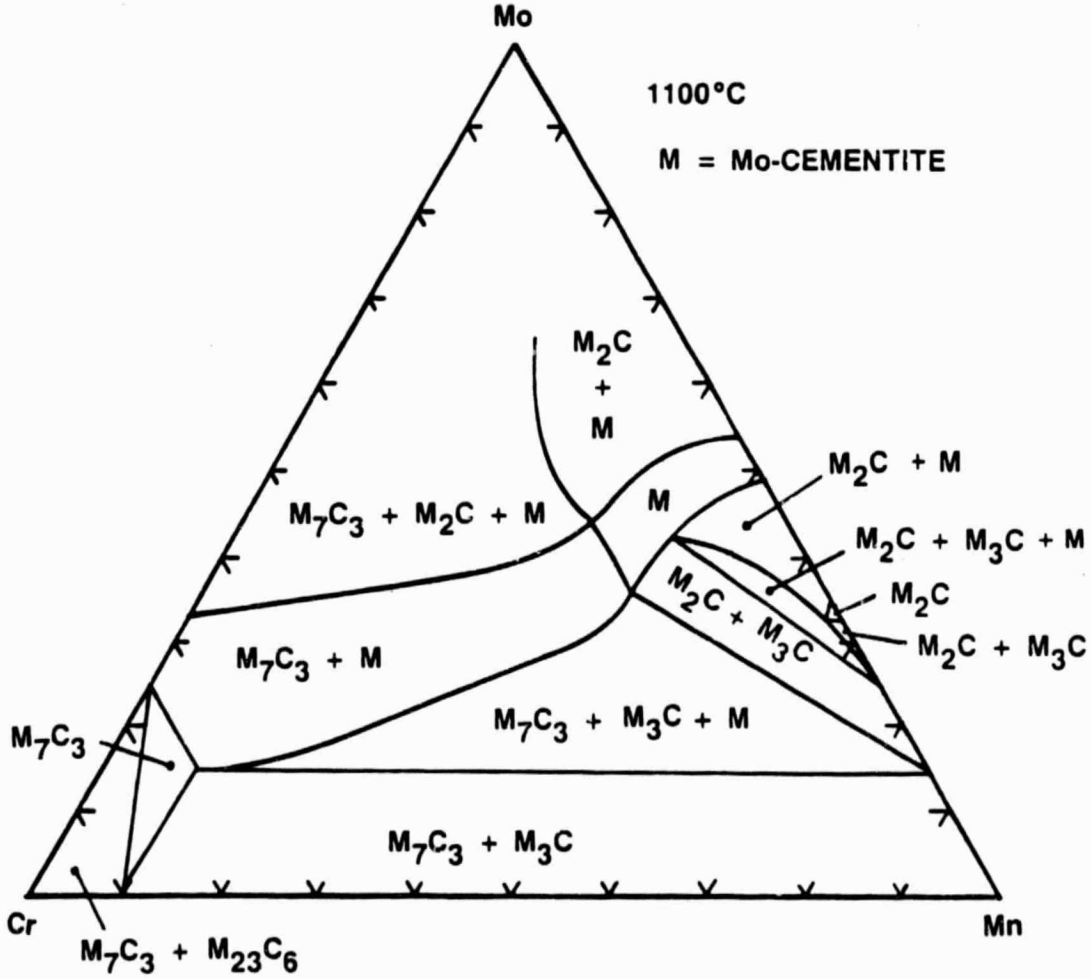

Fig. 11 Isothermal Section as Figure 9, 50 at .% Fe at 1100°C [43]

III. Results

A. Selection and Constitution of Alloys

The results presented in this section are made up of contributions from United Technologies Research Center and this thesis work. The UTRC data consists of alloy casting details, cycle oxidation, stress rupture, and creep test results. This dissertation deals specifically with the phase stability for each alloy as the compositions were adjusted to achieve the demanding high-temperature properties.

Table 1 lists the first twelve candidate alloys based on the Fe-Cr-Mn(Mo)-Al-C(N) multicomponent system. The alloys were produced by induction melting under argon cover and casting into both copper chill and ceramic (Al_2O_3 + SiO_2) shell molds [44]. Micrographs were taken from each casting and the volume fraction determined of the dispersed carbide phase (Table 1).

The phases of eleven of the first twelve alloy candidates cast in chill molds were examined by X-ray powder diffraction. The alloys were converted to powder by diamond filing and examined using Co-K_α radiation in a small diameter Debye-Scherrer camera. The dispersed carbide phase was isolated by dissolution of each alloy in an alcoholic bromine solution. The filtered and dried extraction was examined using Cr-K_α radiation. The results of these analyses are presented in Table 2 where the phases present in each alloy are reported with their respective lattice parameters calculated from the back reflection lines of smallest

TABLE 1

Composition of Alloy Candidates
(Percentage by Weight)

Alloy No.	Fe	Mn	Cr	Mo	Al	C	N	Point Count Vol. % Carbides	Vol. Anal. % Carbides
NASAUT 1	bal	10	20	-	-	1	-	9.9	10.3
NASAUT 2	bal	15	15	-	-	1	-	6.5	5.3
NASAUT 3	bal	10	15	-	5	1	-	-	5.8
NASAUT 4	bal	15	12	3	-	1	-	-	8.5
NASAUT 5	bal	15	10	4	2	1	-	16.7	4.9
NASAUT 6	bal	10	-	10	2	1	-	9.3	9.3
NASAUT 7	bal	15	5	10	-	1	-	17.6	17.6
NASAUT 8	bal	10	-	4	2	1	-	4.6	4.7
NASAUT 9	bal	15	10	-	2	-	1	-	--
NASAUT 10	bal	10	15	-	-	1	-	-	7.6
NASAUT 11	bal	10	12	3	-	1	-	17.8	4.2
NASAUT 12	bal	15	15	-	2	1	1	-	7.4

TABLE 2

Phase Identification

Alloy No.	Matrix		Carbides					
	Phase	Lattice Parameter (a)Å	Phase	Lattice Parameter (a)Å		Phase	Lattice Parameter (a)Å	(c)Å
NASAUT 1 (A81-344)	γ	3.62	$M_{23}C_6$	10.555	>	M_7C_3	13.82	4.54
NASAUT 2 (A81-345)	γ + minor α	3.601 2.57	$M_{23}C_6$	10.56	<	M_7C_3	13.95	4.50
NASAUT 3 (A81-346)	γ + equal amt. α	3.646 2.86	no $M_{23}C_6$	-		M_7C_3	13.49	4.50
NASAUT 4 (A81-405)	γ	3.60	$M_{23}C_6$	-	+	no M_7C_3 unknown constituent		
NASAUT 5 (A81-349)	γ + trace α	3.594 -	$M_{23}C_6$ (small amt.)	10.64	<	βMn(C)	6.39	
NASAUT 6 (A81-350)	γ + minor α	3.61 -	$(Mo,Fe,Mn)_2C$	a=2.9855 c=4.7048	>	unknown constituent		

TABLE 2 (continued)

Phase Identification

Alloy No.	Matrix		Carbides					
	Phase	Lattice Parameter (a)Å	Phase	Lattice Parameter (a)Å		Phase	Lattice Parameter (a)Å	(c)Å
NASAUT 7 (A81-354)	γ	3.61	unknown constituent		<	βMn(C)	6.43	
NASAUT 8 (A81-355)	γ	3.61	M_2C	a=2.975 c=4.705			poor film	
NASAUT 10 (A81-444)	γ	3.5996+)	$M_{23}C_6$	10.55	<	M_7C_3	13.95	4.505
NASAUT 11 (A81-347)	γ	3.61	$M_{23}C_6$	10.64				
NASAUT 12 (A81-384)	α + minor γ	2.86 3.60	$M_{23}C_6$	10.58	>	M_7C_3	13.95	4.505
					≥	M_2C minor	-	

+) γ in extracted carbide 3.640Å

interplanar spacings. The 0.2% offset yield and tensile strengths of the candidate alloys in the as-cast condition were determined at room temperature and 788°C. The data are reported in [44] and reveal that NASAUT 3 is strongest at room temperature, but weakens off markedly at elevated temperature. NASAUT 9 was abandoned due to a very low yield strength, although this alloy displayed a favorable resistance to fracture in Charpy impact tests.

Cyclic oxidation testing at 870°C was performed on all candidate alloy modifications [44]. Disks 0.385" in diameter were cut from chill cast bars and surface ground to a thickness of 0.145". A hole was drilled (0.062" diameter) through each sample and all samples were polished through 600 grit paper. Each sample was cleaned in methanol, weighed, and its surface area calculated. Samples were suspended above an 870°C vertical tube furnace on a platinum wire. Each cycle consisted of lowering the sample into the furnace for 55 minutes, then withdrawing, and allowing 5 minutes to cool to room temperature before the start of the next cycle. Every 20 cycles the samples were removed from the wires and their weights recorded. The weight changes per unit surface area for each alloy tested for 200 cycles (hrs) are presented graphically in Fig. 12. The importance of both chromium and aluminum in combination is noted.

Modifications (e.g., Mn, Cu, Ni) of these candidate alloys were prepared each with 1.5w/oC and numbered as -A, -B, -C etc. to the original composition. Table 3 presents the stress rupture data for the alloys and identifies NASAUT 1, 2, and 4 as having the greatest resistance to rupture. Figure 13 contains the cyclic oxidation data for candidate alloys containing aluminum as this was thought to form the adherent

COMPOSITION W/O

ALLOY NO.	Mn	Cr	Mo	Al	C	N
NASAUT 1	10	20	—	—	1	—
NASAUT 2	15	15	—	—	1	—
NASAUT 3	10	15	—	5	1	—
NASAUT 4	15	12	3	—	1	—
NASAUT 5	15	10	4	2	1	—
NASAUT 6	10	—	10	2	1	—
NASAUT 7	15	5	10	—	1	—
NASAUT 8	10	—	4	2	1	—
NASAUT 9	15	10	—	2	—	1
NASAUT 10	10	15	—	—	1	—
NASAUT 12	15	15	—	2	1	1

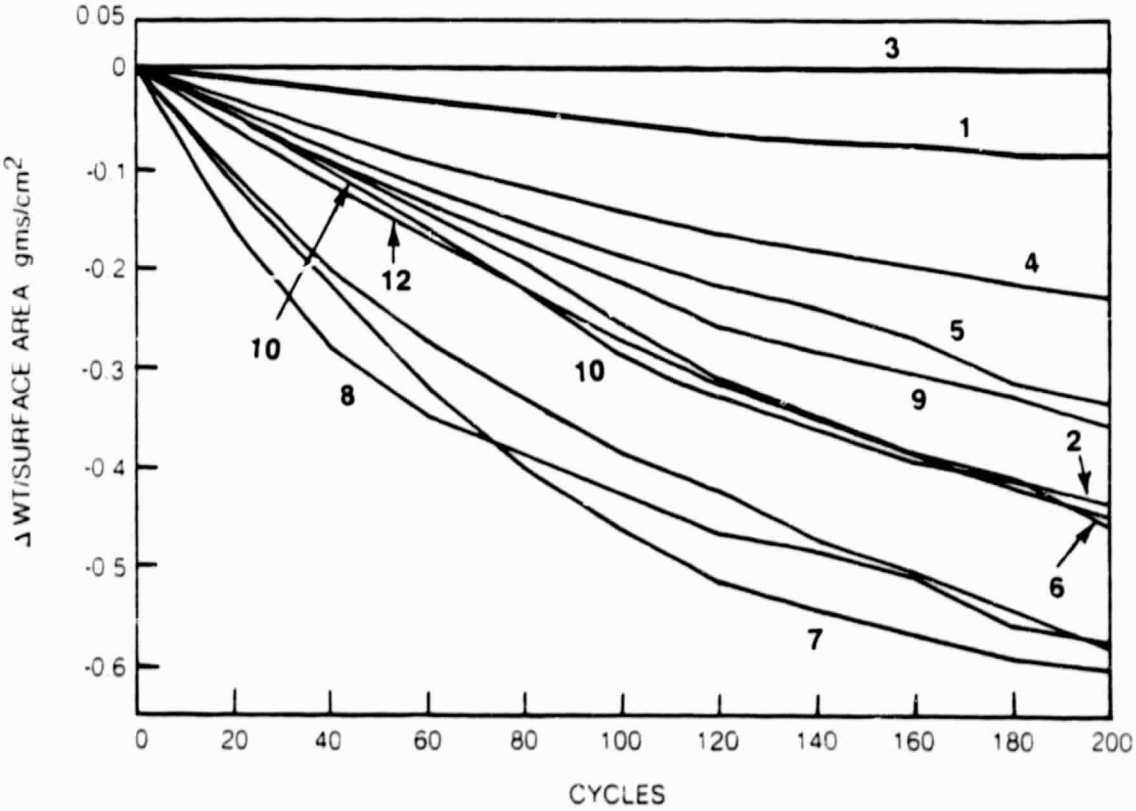

Fig. 12 Cyclic Oxidation of Candidate Alloys [44]

TABLE 3

Stress Rupture Data for Candidate Alloys [44]

Alloy Ident.	Composition (w/o) Mn	Cr	Mo	Al	C		Lab Number	Temp °C	Stress ksi	Time to Rupture hrs	RA %	Elong %
1	10	20			1.5		543-04	777	25→35	445*1	56.4	21.4
1	10	20			1.0		543-01		35	3.6	45.1	23.8
1	10	20			1.5		543-02		35	24.0	54.9	22.1
1A	10	20		2.5	1.5		642-02		30	10.6	4.9	8.5
2	15	15			1.0		408-03		25	5.1	45.7	35.6
2	15	15			1.5		541-02		25→35	123.1*2	53.7	23.8
3	10	15		5	1.5		491-03		25	0.1	62.7	52.5
3	10	15		5	1.5		491-04		25	0.1	50.6	37.6
3A	15	15		5	1.5		641-03		25	0.2	54.9	32.7
3B	10	15		5	1.5	5Ni	646-02		25	0.9	39.0	31.8
3C	10	15		5	1.5	5Cu	637-03		25	0.4	8.5	8.0
4	15	12	3		1.0		410-03		25	24.8	76.1	23.5
4	15	12	3		1.5		539-01		25→30	137.4*3	64.6	21.9
4A	15	12	3	5	1.5		640-02		25	0.1	63.4	51.3
5	15	10	4	2	1.5		535-02		25	24.2	50.6	29.9
5	15	10	4	2	1.5		535-03		25	27.6	-	-
6	10		10	2	1.0		414-03		25	44.2	30.1	16.0
6	10		10	2	1.5		534-01		30	6.0	37.8	12.2

TABLE 3 (continued)

Stress Rupture Data for Candidate Alloys [44]

Alloy Ident.	Composition (w/o) Mn	Cr	Mo	Al	C		Lab Number	Temp °C	Stress ksi	Time to Rupture hrs	RA %	Elong %
6A	10		10	5	1.5		639-03		25	25.3	47.6	27.3
7	15	5	10		1.5		530-02		25	52.2	70.4	28.7
7	15	5	10		1.5		530-04		25	43.2	57.3	31.1
8	10		4	2	1.5		528-01		25	0.8	49.3	40.5
8	10		4	2	1.5		528-02		25	10.8	31.3	18.1
10	10	15			1.0		445-03		25	2.8	35.5	35.8
10	10	15			1.0		445-04		25	19.1	84.1	36.0
12	15	15		2	1.0	1N	411-03		25	46.3	8.6	9.8
12	15	15		2	1.5	1N	589-01		25	31.2	25.6	16.0

*1 205.1 hrs @ 25 ksi
200.1 hrs @ 30 ksi
39.8 hrs @ 35 ksi

*2 67.7 hrs @ 25 ksi
31.3 hrs @ 30 ksi
24.1 hrs @ 35 ksi

*3 67.1 hrs @ 25 ksi
70.3 hrs @ 30 ksi

COMPOSITION W/O

ALLOY NO.	Mn	Cr	Mo	Al	C	Cu
NASAUT 1	10	20	—	—	1.5	—
NASAUT 1A	10	20	—	2.5	1.5	—
NASAUT 3	10	15	—	5	1.5	—
NASAUT 3C	10	15	—	5	1.5	5
NASAUT 4A	15	12	3	5	1.5	—
NASAUT 6	10	—	10	2	1.5	—
NASAUT 6A	10	—	10	5	1.5	—

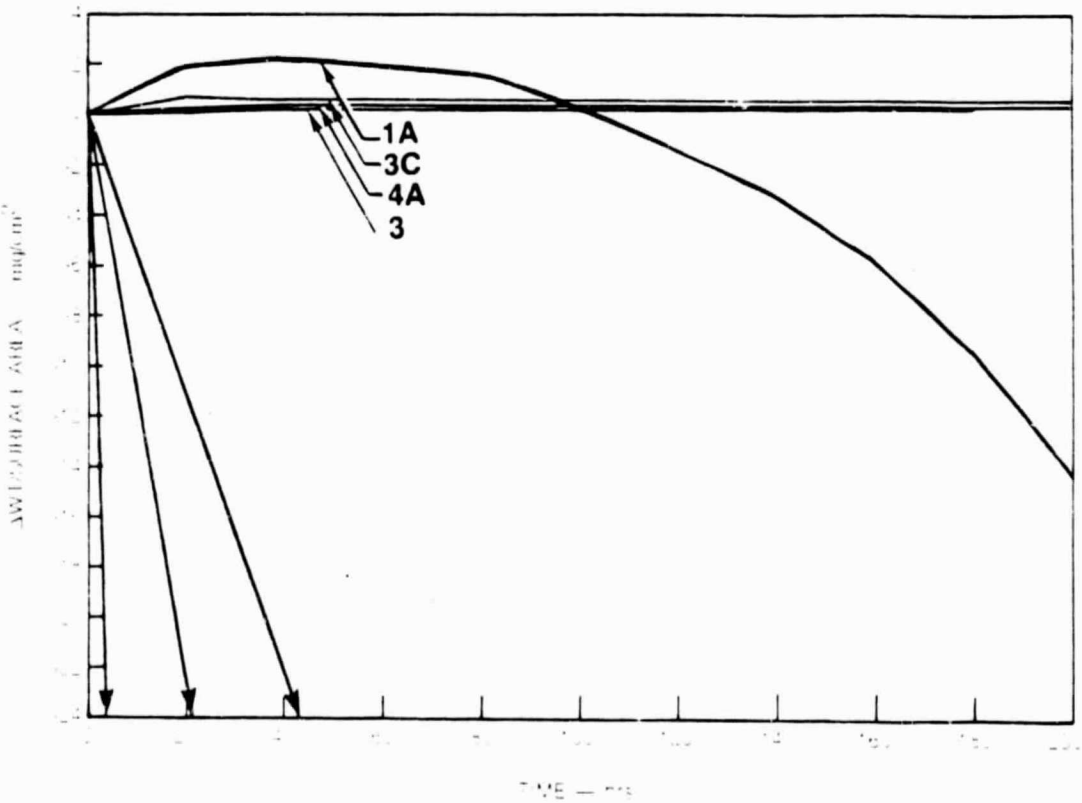

Fig. 13 Cyclic Oxidation of Modified Candidate Alloys [44]

Al_2O_3 phase, thus protecting the alloy. It is clear that NASAUT 4A, 3 and 3C offer superior cyclic oxidation resistance. The addition of 0.5w/oC (Table 3) to the alloys resulted in significant increases in room temperature strength; however, this was not true at elevated temperatures. Alloys NASAUT 7, 8, and 12 were found to have high strengths but were poor with respect to oxidation kinetics, and thus were eliminated as candidates.

The phase stability within candidate alloys is shown to vary as the compositions are adjusted to achieve strength, oxidation and rupture criteria. Table 4 presents the strongest lines from extracted carbide phase equilibria for NASAUT 2 with M_7C_3 and $M_{23}C_6$ phases coexisting.

Table 5 lists the evaluation of a powder pattern of NASAUT 3 with the M_7C_3 carbide appearing as the stable phase. Table 2 shows this Al containing alloy to have equal amounts of α-Fe and γ-Fe, with the lattice parameters of the M_7C_3 carbide the smallest (a=13.49Å, c=4.50Å) as compared to other alloys. Increased amounts of Mn, in combination with Mo + Al additions were found to stabilize the β-Mn(C) phase as seen for NASAUT 5 (Table 6). Evidence for the effects of Cr on phase stability is found with NASAUT 6 (Table 7) in which the removal of chromium from the system formed the $(Mo, Fe, Mn)_2C$ carbide. The importance of the Cr/Mn ratio is seen in NASAUT 10 which formed M_7C_3 + $M_{23}C_6$ (Table 8). As the carbide extraction was not complete, trace amounts of the desired γ-Fe phase were obtained at the carbide interface and the lattice parameter (see Table 2) of this γ-Fe was measured to be a=3.64$_0$Å, somewhat larger than the conventional matrix lattice parameters. The comparison to NASAUT 2 shows that the Cr/Mn ratio can stabilize the α-Fe and/or γ-Fe phase. The $M_{23}C_6$ carbide in Table 9 exists with the γ-Fe matrix

TABLE 4

NASAUT 2, Extracted Carbides, Cr-Kα Radiation

Intensity	θ	$\sin^2\theta$ obs.	$\sin^2\theta$ calc.	$M_{23}C_6$	M_7C_3
f	29.1	0.23652	0.2353	(420)	
f	32.2	0.28396	0.2823	(300)(221)	$(50\bar{5}1)(20\bar{2}2)$
st	34.4	0.31918	0.3176	(310)	$(42\bar{6}1)$
m	66.9	0.84607	0.8469	(820)(660)	
m^-	70.0	0.88302	0.8822	(555)(751)	
st	72.0	0.90451	0.9040		$(60\bar{6}3)$
st	76.1	0.94229	0.9415		$(6,4,\bar{10},2)$
st	79.1	0.96424	0.9623		$(10,0,\bar{10},1)$
st	80.5	0.97276	0.9720		$(61\bar{7}3)$ $(6,6,\bar{12},0)$

TABLE 5

NASAUT 3, Extracted Carbides, Cr-Kα Radiation

Intensity	θ	$\sin^2 \theta$ obs.	$\sin^2 \theta$ calc.	M_7C_3
m	30.3	0.25455	0.25130 0.25200 0.25750	$(41\bar{5}1)$ $(42\bar{6}0)$ (0002)
m	32.9	0.29583	0.28730 0.29350	$(50\bar{5}1)$ $(20\bar{2}2)$
st	34.3	0.31756	0.3143	$(42\bar{6}1)$
m	39.5	0.40459	0.3953 0.4015	$(43\bar{7}1)$ $(40\bar{4}2)$
m	41.2	0.43387	0.4320	$(44\bar{8}0)$
m^-	53.3	0.64284	0.6383	$(80\bar{8}1)$
m	58.3	0.72388	0.7110 0.7255	$(7,3,\bar{10},0)$ $(62\bar{8}2)$
st	71.9	0.90400	0.9040	$(60\bar{6}3)$

TABLE 5 (continued)

NASAUT 3, Extracted Carbides, Cr-Kα Radiation

Intensity	θ	$\sin^2 \theta$ obs.	$\sin^2 \theta$ calc.	M_7C_3
st	76.0	0.94197	0.9415	$(6,4,\bar{10},2)$
st	78.8	0.96227	0.9623	$(10,0,\bar{10},1)$
st	80.3	0.97190	0.9670 0.9720	$(61\bar{7}3)$ $(6,6,\bar{12},0)$

TABLE 6

NASAUT 5, Extracted Carbides, Cr-Kα Radiation

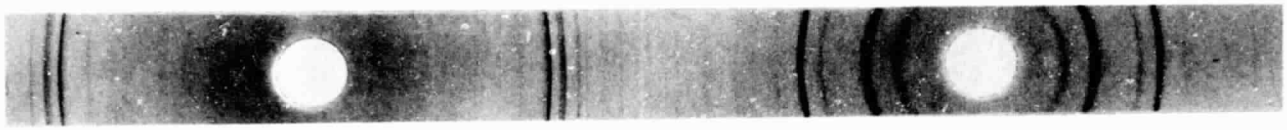

Intensity	θ	$\sin^2 \theta$ obs.	$\sin^2 \theta$ calc.	βMn(C)
f	32.0	0.28081	0.27835	(300)(221)
st	32.6	0.29027	0.28913	(300)(221)
f^+	34.0	0.31269	0.31349	(310)
m	34.6	0.32245	0.32126	(310)
W	36.5	0.35548	0.35338	(311)
f*	37.6	0.37227	0.37114	
f*	39.8	0.40940	0.40593	
f	42.0	0.44773	0.44976	(321)
w	49.5	0.57822	0.57827	(330)(411)
w	53.3	0.64890	0.64252	(420)

*unidentified

TABLE 6 (continued)

NASAUT 5, Extracted Carbides, Cr-Kα Radiation

Intensity	θ	$\sin^2 \theta$ obs.	$\sin^2 \theta$ calc.	βMn(C)
f*	63.7	0.80369	-	
st^+	66.0	0.83456	0.83527	(510)
m	68.7	0.86805	0.86740	(511)(333)
st	74.6	0.92948	0.93165	(520)
m^-	78.7	0.96161	0.96378	(521)

*unidentified

TABLE 7

NASAUT 6, Extracted Carbides, Cr-Kα Radiation

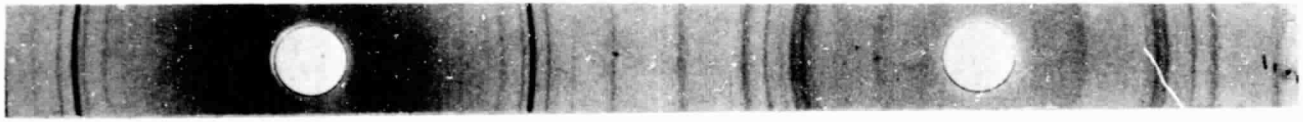

Intensity	θ	$\sin^2 \theta$ obs.	$\sin^2 \theta$ calc.	$(Mo,Fe,Mn)_2C$
w	26.4	0.19770	0.1965	$(10\bar{1}0)$
w	29.3	0.23949	2.2371	(0002)
st	30.6	0.25912	0.2558	$(10\bar{1}1)$
m*	32.7	0.29186	-	
w*	36.0	0.34549	-	
m	41.2	0.43387	0.4336	$(10\bar{1}2)$
m	50.2	0.59026	0.5895	$(11\bar{2}0)$
w	50.6	0.59712	0.5895	$(11\bar{2}0)$
f*	52.8	0.634[illegible]6	-	

*unidentified

TABLE 7 (continued)

NASAUT 6, Extracted Carbides, Cr-Kα Radiation

Intensity	θ	$\sin^2 \theta$ obs.	$\sin^2 \theta$ calc.	$(Mo,Fe,Mn)_2C$
m	58.6	0.72855	0.7301	$(10\bar{1}3)$
w	59.0	0.73473	0.7301	$(10\bar{1}3)$
m*	61.6	0.77378	-	
f*	63.9	0.80645	-	
m	65.2	0.82406	0.8266	$(11\bar{2}2)$
m	66.6	0.84772	0.8453	$(20\bar{2}1)$
w*	67.8	0.85723	-	
f*	71	0.89400	-	
f*	71-5-72	0.90191	-	
m	76.6	0.94629	0.9486	(0004)
f*	77	0.94940	-	

*unidentified

TABLE 8

NASAUT 10, Extracted Carbides, Cr-Kα Radiation

Intensity	θ	$\sin^2\theta$ obs.	$\sin^2\theta$ calc.	M_7C_3	$M_{23}C_6$	γFe
w	29.2	0.23801	0.2356		(420)	
w	30.3	0.25455	-	(42$\bar{6}$0)(41$\bar{5}$1)(0002)		
w	32.2	0.28396	0.2829		(422)	
st	33.1	0.29822	0.2970	(20$\bar{2}$2)(50$\bar{5}$1)		
st	34.4	0.31919	0.3182	(42$\bar{6}$1)	(333)(511)	
w	38.0	0.37904	0.3772		(440)	
w	39.0	0.39604	0.3961			(200)
w	40.0	0.41318	0.4125		(531)	
w⁻	41.2	0.43387	0.4316	(44$\bar{8}$0)		
w	58.4	0.72544	-	(62$\bar{8}$2)(7,3,$\bar{10}$,0)		

TABLE 8 (continued)

NASAUT 10, Extracted Carbides, Cr-Kα Radiation

Intensity	θ	$\sin^2 \theta$ obs.	$\sin^2 \theta$ calc.	M_7C_3	$M_{23}C_6$	γFe
f	60.2	0.75302	0.7543		(800)	
m	62.8	0.79106	0.7922			(220)
m^-	63.3	0.79811	0.8015		(644)	
m^+	67.0	0.84733	0.8486		(660)(822)	
m	70.0	0.88302	0.8840		(555)(751)	
m^+	72.1	0.90553	-	$(60\bar{6}3)$		
st^-	76.1	0.94229	-	$(6,4,\overline{10},2)$		
m	79.2	0.96489	-	$(10,0,\overline{10},1)$		
st	80.7	0.97388	-	$(61\bar{7}3)$ $(6,6,\overline{12},0)$		

TABLE 9

NASAUT 11, Extracted Carbides, Cr-Kα Radiation

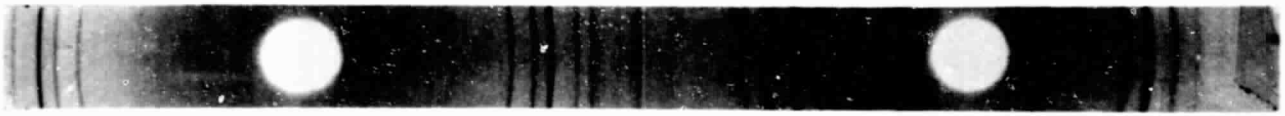

Intensity	θ	$\sin^2 \theta$ obs.	$\sin^2 \theta$ calc.	$M_{23}C_6$
m	28.95	0.23430	0.23196	(420)
m	32.0	0.28081	0.27835	(422)
st	34.0	0.31269	0.31349	(333)(511)
m⁻	37.5	0.37059	0.37114	(440)
m⁻	39.6	0.40631	0.40593	(531)
f	40.3	0.41834	0.41753	(600)
f	42.9	0.46338	0.46372	(620)
w	45.6	0.51047	0.51031	(622)
w	59.5	0.74240	0.74227	(800)
m	62.5	0.78679	0.78866	(644)

TABLE 9 (continued)

NASAUT 11, Extracted Carbides, Cr-Kα Radiation

Intensity	θ	$\sin^2 \theta$ obs.	$\sin^2 \theta$ calc.	$M_{23}C_6$
st	66.0	0.83456	0.83506	(660)(822)
m	68.7	0.86805	0.86985	(555)(751)
m,d	78.7	0.96160	0.96263	(911)

TABLE 10

NASAUT 12, Extracted Carbides, Cr-Kα Radiation

Intensity	θ	$\sin^2\theta$ obs.	$\sin^2\theta$ calc.	$M_{23}C_6$	M_7C_3
f*	23.8	0.1628			
w*	25.15	0.1806	0.1806		$(10\bar{1}0)$
w*	27.5	0.2132	0.2132		(0002)
m	29.0	0.2350	0.2339 0.2344	(420)	$(10\bar{1}1)$
vw	30.2	0.2530	-		$(42\bar{6}0)(41\bar{5}1)(0002)$
m	32.2	0.2839	0.2813	(422)	
m⁻	32.8	0.2934	-		$(50\bar{5}1)(20\bar{2}2)$
st	34.4	0.3192	0.3164	(333)(511)	$(42\bar{6}1)$
m	37.8	0.3756	0.3750	(440)	

*unidentified

TABLE 10 (continued)

NASAUT 12, Extracted Carbides, Cr-Kα Radiation

Intensity	θ	$\sin^2 \theta$ obs.	$\sin^2 \theta$ calc.	$M_{23}C_6$	M_7C_3
vwd*	38.7	0.3909	0.3938		$(10\bar{1}2)$
m^-	39.9	0.4114	0.4102	(531)	
wd	40.5	0.4218	0.4219	(600)	
wd	46.0	0.5174	0.5157	(622)	
m*	47.5	0.5436	0.5418		$(11\bar{2}0)$
m*	54.25	0.6586	-		$(10\bar{1}3)$
w^-	58.3	0.7238	-		$(62\bar{8}2)(7,3,\bar{10},0)$
st^-	60.3	0.7545	0.7500	(800)	$(11\bar{2}2)$
w	61.8	0.7767	0.7757		$(20\bar{2}1)$
w^+	63.3	0.7981	0.7970	(644)	
st	66.7	0.8435	0.8438	(660)(822)	
st^-	69.7	0.8796	0.8790	(555)(751)	

*unidentified

TABLE 10 (continued)

NASAUT 12, Extracted Carbides, Cr-Kα Radiation

Intensity	θ	$\sin^2\theta$ obs.	$\sin^2\theta$ calc.	$M_{23}C_6$	M_7C_3
m	71.9	0.9035	0.9045		$(60\bar{6}3)$
st	75.6	0.9382	0.9376	(840)	$(64\bar{6}2)$
m	78.9	0.9629	0.9639		$(10.0,\bar{10},1)$
st⁻	80.4	0.9722	0.9728	(911)	$(61\bar{7}3)$

and has a lattice parameter (a=10.64Å) that compares favorably with NASAUT 5. Increasing the amount of Mn to achieve Cr/Mn = 1, removing the Mo and adding Al with nitrogen produces $M_{23}C_6$,M_7C_3 and an unidentified phase all coexisting with α-Fe and a minor amount of γ-Fe (see Tables 2 and 10).

B. Modified Alloy Phase Stability

The phase stabilities of the modified alloys listed in Table 3 were also inspected by powder X-ray diffraction. With the addition of 2.5 w/o Al to NASAUT 1 only the M_7C_3 carbide (a = 13.96_6Å and c = 4.496Å) was observed. The lattice parameter of the γ-iron matrix was unchanged. The addition of 5.0 w/o Al to NASAUT 4 also promoted a structural change in the carbide from $M_{23}C_6$ to M_7C_3 as well as a destabilization of the γ-iron matrix. The cubic lattice parameter for the α-iron present was calculated at 2.86_7Å and 3.66_3Å for the γ-iron coexisting with α-Fe. The addition of more aluminum (5 w/o vs. 2 w/o) in NASAUT 6 resulted in essentially the same phases with the previously unknown constituent identified as traces of M_7C_3. The lattice parameters of the hexagonal M_2C phase decreased slightly and the γ-Fe phase expanded to a = 3.665Å.

The additions of 5 w/o of the gamma stabilizing elements, Mn, Ni, and Cu to NASAUT 3, which previously contained about equal amounts of γ and α Fe, resulted in the expected transformation. The lattice parameters of the γ phases were found to be: a = 3.64_5Å for the Mn addition and a = 3.63_1Å for the Ni addition, with a value for the Cu addition somewhat between those found for Mn and Ni. The extracted carbides from these three gamma stabilized alloys showed virtually no change in the measured lattice parameters of the M_7C_3 between the unmodified NASAUT 3 alloy and those of the gamma stabilized versions.

On the basis of strength and oxidation resistance, two alloys NASAUT 1 & 4 were identified as promising candidates to be examined more fully . Alloy iterations with small additions of both aluminum and silicon were examined extensively as these were thought to improve the alloy surface stability. The compositions of the modifications to both NASAUT 1 (eight modifications) and NASAUT 4 (seven modifications) are described in Table 11 [44]. The extracted carbide phase and filings from the matrix phase were identified by X-ray diffraction, and the structure and lattice parameter results for all alloy modifications are presented in Table 12 for NASAUT 1 modifications and Table 13 for NASAUT 4 modifications. The two alloys chosen for more complete mechanical and physical characterization, NASAUT 1G and NASAUT 4G, both exhibit γ iron matrix with dispersed M_7C_3 and $M_{23}C_6$ + NbC carbide phases. The X-ray diffraction data for the extracted carbides of NASAUT 4G are presented in Table 14.

In the course of this study of iron base alloys of nominal composition 10-15 w/o Mn, up to 20 w/o Cr, 10 w/o Mo, 5 w/o Al and 1.5 w/o C, bal. Fe, it was found that mainly a duplex structure γ (austentite) + M_7C_3 occurs. In the case of Mo-containing alloys, the gamma (γ competes with ferrite (α), as does M_7C_3 with $M_{23}C_6$ and M_2C. Interestingly, the extracted carbide product of an alloy with 15 w/o Mn, 10 w/o Cr, 4 w/o Mo, 2 w/o Al and 1.5 w/o C has been shown to consist of a phase having the β-Mn type structure and a minor amount of $M_{23}C_6$ [45]. The matrix of the above alloy was almost all γ and only traces of α were present. There is a complete fit in indexing for the carbides and the intensities of the reflections of the β-Mn type carbide compare perfectly to those expected for the β-Mn type structure. Considering the lattice parameter,

TABLE 11

Composition of Alloy Candidates [44]
(percentage by weight)

Alloy No.	Mn	Cr	Mo	Al	C	Si	Nb
NASAUT 1	10	20	-	-	1.5	-	-
1A	10	20	-	2.5	1.5	-	-
1B	10	20	-	1.0	1.5	-	-
1C	10	20	-	1.5	1.5	-	-
1D	10	20	-	2.0	1.5	-	-
1E	10	20	-	1.5	1.5	1.0	-
1F	10	20	-	2.5	1.5	1.0	-
1G	10	20	-	-	1.5	1.0	-
1H	10	20	-	0.5	1.5	1.5	-

TABLE 11 (continued)

Composition of Alloy Candidates [44]
(percentage by weight)

Alloy No.	Mn	Cr	Mo	Al	C	Si	Nb
NASAUT 4	15	12	3	-	1.5	-	-
4A	15	12	3	5	1.5	-	-
4B	15	12	-	1.5	1.5	-	1.0
4C	15	12	-	2.5	1.5	-	1.0
4D	15	12	-	3.5	1.5	-	1.0
4E	15	12	3	1.5	1.5	-	1.0
4F	15	12	3	0	1.5	1.0	-
4G	15	12	3	0	1.5	1.0	1.0

TABLE 12

Phase Identification of Modifications to NASAUT 1

Alloy No.	Matrix		Matrix	
	Phase	Lattice Parameter, Å	Phase	Lattice Parameter, Å
NASAUT 1	γ(major)	3.62	$M_{23}C_6$	a = 10.555
			+ M_7C_3	a = 13.82 c = 4.54
NASAUT 1A	γ(major)	3.629	M_7C_3	a = 13.96_6 c = 4.496^6
NASAUT 1B	γ(major) α(minor)	3.625 2.866	M_7C_3	a = 13.94_1 c = 4.529^1
NASAUT 1C	γ(major) α(minor)	3.618 2.853	M_7C_3	a = 13.93_5 c = 4.521^5
NASAUT 1D	α(major) γ(minor)	2.854 3.608	M_7C_3	a = 13.92_2 c = 4.51^2
NASAUT 1E	γ(major) α(minor)	3.628 2.867	M_7C_3	a ≃ 13.94 c ≃ 4.529

TABLE 12 (continued)

Phase Identification of Modifications to NASAUT 1

Alloy No.	Matrix		Matrix	
	Phase	Lattice Parameter, Å	Phase	Lattice Parameter, Å
NASAUT 1F	γ(equal) α(equal)	3.625 2.879	M_7C_3	a = 13.94 c = 4.529
NASAUT 1G	γ(major)	3.58	M_7C_3	a = 13.94 c = 4.510
NASAUT 1H	γ(major) α(minor)	3.62	M_7C_3	similar to 1G

TABLE 13

Phase Identification of Modifications to NASAUT 4

Alloy No.	Matrix		Carbides	
	Phase	Lattice Parameter, Å	Phase	Lattice Parameter, Å
NASAUT 4	γ(major)	3.60	$M_{23}C_6$	
NASAUT 4A	γ(major)	3.66_3	M_7C_3	$a = 14.06_0$
	α(minor)	2.86_7		$c = 4.521_6$
NASAUT 4B	γ(major)	3.625	M_7C_3	
	α(v. minor)	2.875	+ NbC	
NASAUT 4C	γ(major)	3.633	M_7C_3	
	α(minor)	2.878	+ NbC	
NASAUT 4D	γ(major)	3.633	M_7C_3	
	α(minor)	2.862	+ NbC	
NASAUT 4F	γ(major)	3.62	$M_{23}C_6$	
			+ unknown constituent	
NASAUT 4G	γ(major)	3.61	$M_{23}C_6$	$a = 10.61_4$
			+ NbC	$a = 4.43_3$

TABLE 14

X-ray Identification of Extracted Phases in
NASAUT Alloy 4G (A82-262)

Int.	θ	$\sin^2\theta_{obs.}$	$\sin^2\theta_{calc.}$	Phase	Index
st	26.6	0.20049	0.20020	NbC	(111)
m	28.9_5	0.23430	0.23294	$M_{23}C_6$	(420)
mst	31.2	0.26835	0.26699	NbC	(200)
m	32.0	0.28081	0.27953	$M_{23}C_6$	(422)
vst	34.15	0.31513	0.31447	$M_{23}C_6$	(333)(511)
m^-	37.7	0.37396	0.37270	$M_{23}C_6$	(440)
m^-	39.8	0.40774	0.40764	$M_{23}C_6$	(531)
f	40.3	0.41834	0.41929	$M_{23}C_6$	(600)
w	45.7_5	0.51309	0.51245	$M_{23}C_6$	(622)

TABLE 14 (continued)

X-ray Identification of Extracted Phases in
NASAUT Alloy 4G (A82-262)

Int.	θ	$\sin^2\theta_{obs.}$	$\sin^2\theta_{calc.}$	Phase	Index
m	47.0	0.53488	0.53398	NbC	(220)
st	58.9	0.73319	0.73423	NbC	(311)
w	59.6	0.74393	0.74541	$M_{23}C_6$	(800)
m	62.8	0.79106	0.79197	$M_{23}C_6$	(644)
m	63.4	0.79951	0.80098	NbC	(222)
st	66.2	0.83715	0.83855	$M_{23}C_6$	(822)(660)
mst	69.0	0.87157	0.87352	$M_{23}C_6$	(555)(751)
w	74.8	0.93126	0.93176	$M_{23}C_6$	(840)
mst	79.3	0.96553	0.96670	$M_{23}C_6$	(911)

$(Fe,Mn,Cr)_{23}C_6$ $a \simeq 10.61_4$ Å

NbC $a \simeq 4.43_3$ Å

which was determined to be: a = 6.39_5Å, it is obvious that there is a carbide formed rather than an intermetallic. Indeed, the cell parameter is much larger than that for β-Mn (a = 6.32Å), but essentially smaller than for the complex carbide Mo_3Al_2C (a = 6.86_0Å) [46], another "filled up" ordered β-Mn type structure.

Carbides [47] and nitrides [48] with completed β-Mn parent lattices, named π-phases, have been observed earlier. Thus, in alloys of compositions Fe (26.4-65.6 w/o), Cr (48.4-7.3 w/o), W (23.6-26.1 w/o) and C (0.8-0.95 w/o), π-carbide forms after quenching from 1400°C. Goldschmidt [47] could not detect the π-phase in corresponding carbon-free alloys Cr-Fe-W or Cr-Fe-Mo. A π-nitride was first reported by Evans et al. [48]. The ratio of interstitial atom to metal atom of 1/5 indicates a complete filling of the octahedral voids in 4a) of space group $P4_132$. According to the data for the Fe-Cr-W-π-phase one must assume a partial filling only, and this is also true for the newly observed Fe-Mn-Cr-Mo-Al-π-carbide. In both of these cases, the amount of tungsten and molybdenum is rather small, 7.5 and 2 a/o, respectively.

Manganese itself favors the β-Mn structure, which tendency is further enhanced by iron and aluminum. This can be seen from the large domain of the β-Mn solid solutions in the ternary system: Mn-Fe-Al [49]; furthermore molybdenum and aluminum form (in the presence of carbon) the filled-up ordered β-Mn type structure [46], which means yet another stabilization of the β-Mn array. From an EDX analysis of the extracted carbide it was clearly seen that chromium, molybdenum and aluminum preferentially enter the carbide (or carbides), while manganese distributes equally within the matrix and the carbide. The concentration of iron in the π-carbide is roughly one-half of that in the matrix.

According to the lattice parameter of the $M_{23}C_6$ carbide (a $\simeq$ 10.62Å) there is less iron and manganese incorporated, thus decreasing the cell parameter (partially compensated by molybdenum). At any rate, the amount of $M_{23}C_6$ in the extracted product does not appear to change the distribution between π and γ significantly. With no carbon in the matrix [3] the ratio of carbon to metal in the π-carbide is much lower than 1/5; that means that only a partial filling occurs according to the approximate formula $(Fe_{2.0}Mn_{0.7}Cr_{1.0}Mo_{0.4}Al_{0.9})C_x$ ($x \simeq 1/3$). The composition of the π-carbide (Fe-Cr-W) comes close to $(Fe,Cr,W)_5C_x$ ($x \simeq 1/4$).

Table 15 shows the π phase and $M_{23}C_6$ carbide extracted from alloy 15 w/o Mn, 10 w/o Cr, 4 w/o Mo, 2 w/o Al, 1 w/o C, bal-Fe. The π-carbide (Fe-Mn-Cr-Mo-Al) also occurred in the extraction of alloy of composition 15 w/o Mn, 5 w/o Cr, 10 w/o Mo, and 1.5 w/o Al, bal. Fe with a lattice parameter of a $\simeq$ 6.43Å. The major constituents have not been identified, however. One phase appears to be related to the χ-phase, a partially filled α-Mn type structure. Such a phase actually occurs in Fe-Cr-W-C alloys in addition to the π-carbide and γ [47]. The existence of the χ-phase in Fe-Cr-Mo and Fe-Cr-Mo-C alloys has also been described by Takeda et al. [50], and by Andrews et al. [51].

Because of the high thermochemical stability of Mo_2C, this carbide frequently occurs in Mo-containing steels. With respect to the solubility of Mo_2C for iron (carbide) there is some discrepancy. According to Surovoi et al. [52], Mo_2C dissolves some iron. For a formula $(Fe_{0.05}Mo_{0.95})_2C$ the cell parameters were reported to be: a = 3.000; c = 4.719Å, indicating an approximately unchanged a, but a significantly smaller c-parameter than in the case of pure Mo_2C. In a

TABLE 15

Extracted Carbide, Alloy 15w/o Mn, 10 w/o Cr, 4 w/o Mo, 2 w/o Al, 1 w/o C, bal. Fe; Cr-Kα

Int.	$\sin^2\theta_{obs.}$	$\sin^2\theta_{calc.}$	Phase	Index
f^+	0.2321	0.2327	$M_{23}C_6$	(420)
f	0.2808	0.2792	$M_{23}C_6$	(422)
st	0.2903	0.2888	π	(221)(300)
f^+	0.3127	0.3141	$M_{23}C_6$	(311)(511)
m	0.3224	0.3209	π	(310)
w	0.3555	0.3530	π	(311)
f	0.3723	0.3723	$M_{23}C_6$	(440)
f	0.4094	0.4072	$M_{23}C_6$	(531)
f	0.4477	0.4493	π	(321)

TABLE 15 (continued)

Extracted Carbide, Alloy 15w/o Mn, 10 w/o Cr, 4 w/o Mo, 2 w/o Al, 1 w/o C, bal. Fe; Cr-Kα

Int.	$\sin^2\theta_{obs.}$	$\sin^2\theta_{calc.}$	Phase	Index
w	0.5782	0.5776	π	(330)(411)
w	0.6489	0.6418	π	(420)
f	0.8037	0.8023	π	(430)(500)
st	0.8346	0.8343	π	(510)(431)
m	0.8681	0.8664	π	(333)(511)
st$^+$	0.9295	0.9306	π	(520)
m$^+$	0.9616	0.9627	π	(521)

phase diagram iron-molybdenum-carbon, calculated for 1000°C by Uhrenius et al. [53], a small amount of Mo/Fe substitution in Mo_2C has been taken into account. A recent compilation by Holleck [54] does not reveal the existence of an iron containing Mo-subcarbide. It was found, however, that alloys with 2 a/o Fe in Mo_2C were homogeneous [55], although the change of the cell parameters was indeed small. It was assumed that the decrease of the average metal size may be partially compensated by more carbon in the interstices. On the other hand, manganese and chromium (carbides) dissolve in Mo_2C up to ca. 15 (800°C) and 70 mol% (1350°C) respectively, referring to Mn_7C_3 [56], and Cr_7C_3 [54].

Investigating carbides in M-50 tool steel, Bridge et al. [57] derived for the M_2C carbide a formula $(Mo_{0.71}Fe_{0.14}Cr_{0.15})_2C$ based on the assumption that the M_2C only involves these metals. No lattice parameters, however, have been reported.

In extracted products of chromium-free alloys with 10 w/o Mn, 10(4) w/o Mo, 2 w/o Al, 1 w/o C, bal. Fe, M_2C carbide occurs as major constituent. First based on a hexagonal cell, the parameters were found to be : a = 2.984_5 (2.975) and c = 4.704_8 (4.705) Å, significantly smaller than those for pure Mo_2C (a = 3.027, c = 4.742Å) [58], reflecting mainly considerable Mo/Mn or Mo/Mn,Fe substitution in the M_2C carbide. An EDX analysis of the extracted carbide (85.5 a/o Mo, 9.3 a/o Fe and 5.0 a/o Mn) also indicates some substitution of molybdenum by iron and manganese in the M_2C carbide although a minor amount of γ is present.

Parthé et al. [59] have shown that Mo_2C is pseudohexagonal only and described the cell as orthorhombic (space group Pbcn) with the parameters: a = 4.72_4; b = 6.00_4; and c = 5.19_0Å. Rudy et al. [60] later on found that there are two Mo_2C modifications (one hexagonal and one

orthorhombically distorted) with the stability of these depending on temperature and carbon concentration. The powder pattern of the extracted carbide of the alloy mentioned above is unambiguously indexed with the orthorhombic cell (see Table 16). The lattice parameters were determined to be: a = 4.708; b = 5.931 and c = 5.159Å; a corresponds to c_{hex}, b to $2a_{hex}$, and c to $a_{hex}\sqrt{3}$. As mentioned before, the extracted products contain M_2C and some γ (austenite) with a relatively large parameter (3.68Å) which turns out to be essentially larger than the cell parameter of the matrix of the alloy as cast. Thus inspection of the filings of the alloy leads to a parameter of a = 3.61_5Å. This phenomenon was observed with other Fe-Mn-Cr-Mo-Al-C alloys also. It can be understood by assuming that the matrix area near the carbides is highly saturated by carbon and the other γ-stabilizers. As a result of this, a higher chemical resistance toward the extracting agent (bromine-methanol) results.

C. Stress Rupture Properties

As previously mentioned, the stress rupture behaviors of NASAUT 1 and 4 were the best of the initial 12 alloy candidates. NASAUT 1 had the best stress rupture strength with a total accumulated time to failure of 445 hrs at 777°C (205.1 hrs at 25 ksi, 200.1 hrs at 30 ksi, and 39.8 hrs at 35 ksi). NASAUT 4, containing $M_{23}C_6$ carbides, withstood 70.3 hrs at 30 ksi after a previous exposure of 67.1 hrs at 25 ksi. The rupture ductility (% RA) of these two alloys was also greater than 50% as described in more detail in Tables 17 and 18 for NASAUT 1 and NASAUT 4 modifications, respectively. The addition of aluminum, which is a strong α ferrite former in the matrix was clearly observed. Since minor (1-1.5 w/o) silicon additions were as successful in promoting cyclic

TABLE 16

Extracted Carbide of Alloy 10 w/o Mn, 10 w/o Mo, 2 w/o Al, 1 w/o C bal. Fe; Cr-Kα+

Intensity	$\sin^2\theta_{obs.}$	$\sin^2\theta_{calc.}$	Index orthorh.	Index pseudohex.
		{0.1972	(002)	
w	0.1977	{0.1986	(021)	$(10\bar{1}0)$
w	0.2395	0.2367	(200)	(0002)
st	0.2591	{0.2564	(102)}	$(10\bar{1}1)$
		{0.2578	(121)}	
m	0.2919	0.2906		γ(111)
w,c	0.3455	0.3465	(022)	
m	0.4330	{0.4339	(202)}	$(10\bar{1}2)$
		{0.4353	(221)}	
m	0.5903	0.5930	(023)}	$(11\bar{2}0)$
w	0.5971	0.5971	(040)}	

+ without very weak lines of an unidentified constituent
c = coincidence

TABLE 16 (continued)

Extracted Carbide of Alloy 10 w/o Mn, 10 w/o Mo, 2 w/o Al, 1 w/o C bal. Fe; Cr-Kα+

Intensity	$\sin^2\theta$ obs.	$\sin^2\theta$ calc.	Index orthorh.	Index pseudohex.
m	0.7270	0.7297	(302)}	
m	0.7312	0.7320	(321)}	$(10\bar{1}3)$
m	0.7738	0.7750		γ(220)
m	0.8241	0.8275	(223)}	
w	0.8320	0.8343	(240)}	$(11\bar{2}2)$
m	0.8477	0.8433	(104)}	
w	0.8572	0.8524	(142)}	$(20\bar{2}1)$
m,d	0.9439	0.9488	(400)	(0004)

+ without very weak lines of an unidentified constituent
d = diffuse

TABLE 17

Stress Rupture Data for Modifications to NASAUT 1 [44]

Alloy #	Composition						Lab #	Temp °C
	Mn	Cr	Mo	Al	C	Si		
1	10	20	-	-	1.5	-	543-04	777
1	10	20	-	-	1.5	-	543-02	
1B	10	20	-	1.0	1.5	-	111-01	
1B	10	20	-	1.0	1.5	-	111-02	
1C	10	20	-	1.5	1.5	-	155-01	
1C	10	20	-	1.5	1.5	-	155-02	
1D	10	20	-	2.0	1.5	-	164-01	
1D	10	20	-	2.0	1.5	-	164-02	
1A	10	20	-	2.5	1.5	-	642-03	
1E	10	20	-	1.5	1.5	1.0	178-01	
1E	10	20	-	1.5	1.5	1.0	178-02	
1F	10	20	-	2.5	1.5	1.0	177-01	
1F	10	20	-	2.5	1.5	1.0	177-02	
1G	10	20	-	-	1.5	1.0	259-01	
1G	10	20	-	-	1.5	1.0	259-02	
1H	10	20	-	.5	1.5	1.5	275-01	
1H	10	20	-	.5	1.5	1.5	275-02	

TABLE 17 (continued)

Stress Rupture Data for Modifications to NASAUT 1 [44]

Alloy #	Stress	Hrs to Failure	% RA	% Elong.
1	25→35	445*1	56.4	21.4
1	35	24.0	54.9	22.1
1B	30	15.3	15.1	10.6
1B	30	8.4	11.9	9.9
1C	30	4.4	37.0	23.1
1C	30	6.6	32.7	14.9
1D	30	12.4	13.1	11.3
1D	30	16.8	15.1	14.6
1A	30	10.6	4.9	8.5
1E	25→30	77.7*2	5.8	8.7
1E	30	1.6	20.4	14.6
1F	30	0.1	41.5	23.1
1F	25	0.1	47.4	37.4
1G	30	54.1	37.2	46.8
1G	30	100.4	18.6	16.0
1H	30	3.8	20.4	16.5
1H	30	9.2	15.5	10.6

*1 205 hrs at 25 ksi; 200 hrs at 30 ksi; 40 hrs at 35 ksi
*2 50 hrs at 25 ksi; 27.7 hrs at 30 ksi

TABLE 18

Stress Rupture Data for Modifications to NASAUT 4 [44]

Alloy #	Composition							Lab #	Temp °C
	Mn	Cr	Mo	Al	C	Si	Nb		
4	15	12	3	-	1.5	-	-	539-01	777
4A	15	12	3	5	1.5	-	-	640-02	
4B	15	12	-	1.5	1.5	-	1.0	175-01	
4B	15	12	-	1.5	1.5	-	1.0	175-02	
4C	15	12	-	2.5	1.5	-	1.0	171-01	
4C	15	12	-	2.5	1.5	-	1.0	171-02	
4D	15	12	-	3.5	1.5	-	1.0	165-01	
4D	15	12	-	3.5	1.5	-	1.0	165-02	
4E	15	12	3	1.5	1.5	-	1.0	242-01	
4E	15	12	3	1.5	1.5	-	1.0	242-02	
4F	15	12	3	-	1.5	1.0	-	265-01	
4F	15	12	3	-	1.5	1.0	-	265-02	
4G	15	12	3	-	1.5	1.0	1.0	262-01	
4G	15	12	3	-	1.5	1.0	1.0	262-02	

TABLE 18 (continued)

Stress Rupture Data for Modifications to NASAUT 4 [44]

Alloy #	Stress	Hrs to Failure	% RA	% Elong.
4	25→30	137.4*1	64.6	21.9
4A	25	0.1	63.4	51.3
4B	25	9.9	55.6	33.6
4B	25	26.9	38.8	29.2
4C	25	7.9	54.2	36.5
4C	25	17.3	21.7	15.3
4D	25	6.8	69.9	36.7
4D	25	4.3	53.9	23.6
4E	25→30	52.3*2	46.9	19.3
4E	25→30	51.0*3	44.9	25.6
4F	30	20.9	50.2	32.8
4F	30	10.3	55.9	30.4
4G	30	5.6	58.1	44.2
4G	30	3.9	63.7	32.2

*1 67 hrs at 25 ksi
70 hrs at 30 ksi

*2 49 hrs at 25 ksi
3.3 hrs at 30 ksi

*3 49 hrs at 25 ksi
2.0 hrs at 30 ksi

oxidation resistance at 870°C as aluminum, it was particularly interesting to observe the retention of both the γ-austenite matrix structure and stress rupture properties with these small additions of Si. Furthermore, the presence of a fine niobium carbide in the matrix of NASAUT 4G indicated that higher elevated temperature strength could be obtained by heat treatment optimization.

D. Alloy Modifications

The instability of the M_7C_3 carbide in NASAUT 4G as measured by the decomposition product, $M_{23}C_6$, was found in X-ray analyses of extracted carbides. This alloy was exposed either for long periods, e.g. 500 hrs at 650°C, or for shorter periods, e.g. 24 hrs at 1093°C. There was observed a decrease in hardness and stress rupture life after elevated temperature exposure. This concern for increased M_7C_3 stability prompted further alloy modifications to increase the Cr/Mn ratio in the carbide and thereby increase the peritectic temperature from which $M_{23}C_6$ is produced as well as to increase the hardness of the M_7C_3 carbide. The alloy modifications to NASAUT 4G are listed in Table 19 and include addition of boron, nickel, and aluminum nitride, as well as variations in Si, Cr, Mn, Nb and C levels [44]. These modifications were made to ensure that a gamma matrix would result.

The cast microstructures of NASAUT 4G-A and 4G-Al, containing equal amounts of Cr and Mn but differing in niobium content by 0.5 wt.%, were similar to that of NASAUT 4G except for the amount of interdendritic carbides, MC type. Their matrix phases were all γ-iron (fcc) as determined by X-ray powder diffraction patterns of filings. The extracted phases consisted of M_7C_3 + MC + traces of an unidentified phase. NASAUT 4G-B (containing 0.1 wt.% B) also exhibited a gamma-iron matrix and the

TABLE 19

NASAUT 4G Composition Modifications [44]

	Fe	Mn	Cr	Mo	Al	C	Si	Nb	N	B	Ni
NASAUT 4G	bal(wt%)	15	12	3	-	1.5	1.0	1.0	-	-	-
NASAUT 4G-A	bal	15	15	2	-	1.5	1.0	0.5	-	-	-
NASAUT 4G-A1	bal	15	15	2	-	1.5	1.0	1.0	-	-	-
NASAUT 4G-B	bal	15	12	3	-	1.5	1.0	1.0	-	0.1	-
NASAUT 4G-C	bal	15	12	3	0.5	1.5	1.0	1.0	.26	-	-
NASAUT 4G-S	bal	15	12	3	-	1.5	3.0	1.0	-	-	-
NASAUT 4G-D	bal	10	20	3	-	1.5	1.0	1.0	-	-	-
NASAUT 4G-E	bal	15	15	3	-	2.0	1.0	1.0	-	-	-
NASAUT 4G-F	bal	-	30	3	-	1.5	1.0	1.0	-	-	5.0
NASAUT 4G-G	bal	-	30	3	-	2.0	1.0	1.0	-	-	5.0

extracted carbides were similar to NASAUT 4G-A as seen in Table 20. The extracted M_7C_3 (M = Cr,Mn,Fe) phase had a larger cell than 4G-A, i.e. a = 14.028_6Å and c = 4.55_5Å although less chromium was present. A lesser amount of MC (M = Nb,Mo) phase (a = 4.390_8Å) was observed as compared to M_7C_3.

Difficulties were experienced in retaining nitrogen in NASAUT 4G-C castings and no nitrides were observed as precipitates in the gamma matrix from optical microscopy inspections.

NASAUT 4G-A was modified by small additions of 0.1-1.0 wt.% hafnium, 0.1-1.0 wt.% yttrium, and 0.1-1.0 La+Ce (mischmetal). These alloys, prior to examination in cyclic oxidation were also characterized by X-ray diffraction and optical microscopy to document their phases and microstructures. The results of X-ray diffraction experiments on filings and extracted carbides from each of these alloys is presented in Table 21.

Each of the modifications to NASAUT 4G was given an aging heat treatment (100 hrs at 650°C) and creep tested in air at 788 and 843°C. The results are presented in Table 22. The boron containing modification, NASAUT 4G-B, tested at 788°C/35 ksi indicated a slight decrease in rupture life but increased rupture ductility; i.e., 45% RA and ~ 26% elongation, compared with NASAUT 4G. The modifications, 4G-A and 4G-A1, examined to establish the effect of increased Cr/Mn ratio at test conditions of 788°C/30-35 ksi and 843°C/20-25 ksi resulted in improved rupture life with respect to the base, NASAUT 4G [44].

The stability of the M_7C_3 carbide, as evidenced by the transformation to $M_{23}C_6$ in elevated temperature testing of alloys with increased Cr/Mn content, was however disappointing. Carbides extracted from

TABLE 20

Indexed Carbide Powder Patterns from NASAUT 4G-B
(A82-621) using Cr-Kα Radiation

Int.	θ	$\sin^2\theta$ obs.	$\sin^2\theta$ calc.	Phase Index
vw*	18.8	0.1038		
f	22.3	0.1440	0.1423	M_7C_3 $(40\bar{4}0)$
m,b	27.0	0.2061	0.2042	MC (111)
st			0.2492	M_7C_3 $(42\bar{6}0)$
	30.0	0.2550	0.2511	M_7C_3 $(41\bar{5}1)$
			0.2574	M_7C_3 (0002)
w+	31.6	0.2745	0.2722	MC (200)
m+	32.2	0.2839	0.2866	M_7C_3 $(50\bar{5}1)$
m	32.9	0.2950	0.2930	M_7C_3 $(20\bar{2}2)$
vst, b	34.0	0.3135	0.3133	M_7C_3 $(42\bar{6}1)$
w*	35.3	0.3339		
f+	37.2	0.3655	0.3641	M_7C_3 $(22\bar{4}2)$
w	38.3	0.3841	0.3844	M_7C_3 $(60\bar{6}1)$
m	39.2	0.3994	0.3933	M_7C_3 $(43\bar{7}1)$
			0.3997	M_7C_3 $(40\bar{4}2)$

*unidentified

TABLE 20 (continued)

Indexed Carbide Powder Patterns from NASAUT 4G-B
(A82-621) using Cr-Kα Radiation

Int.	θ	$\sin^2\theta$ obs.	$\sin^2\theta$ calc.	Phase Index
m*	40.9	0.4287	0.4267	M_7C_3 $(44\bar{8}0)$
f	41.9	0.4460		
f	45.5	0.5087	0.5066	M_7C_3 $(42\bar{6}2)$
w	47.6	0.5453	0.5445	MC (220)
f	49.1	0.5713	0.5710	M_7C_3 $(71\bar{8}1)$
m*	52.9	0.6361	0.6333	M_7C_3 $(80\bar{8}1)$
vf	56.0	0.6873		
m	58.1	0.7207	0.7197	M_7C_3 $(62\bar{8}2)$
m,d	59.9	0.7485	0.7486	MC (311)
w,d	64.3	0.8119	0.8167	MC (222)
w*	65.5	0.8280	0.8289	M_7C_3 $(64\bar{1}\bar{0},1)$
w*	67.9	0.8584		
w	70.6	0.8897		
st	71.5	0.8993	0.8992	M_7C_3 $(60\bar{6}3)$
st	75.0	0.9330	0.9331	M_7C_3 $(64\bar{1}\bar{0},2)$
st,d	77.5	0.9531	0.9534	M_7C_3 $(10,0\bar{1}\bar{0},1)$
st,d	78.5	0.9602	0.9602	M_7C_3 $(66\bar{1}\bar{2},0)$
			0.9615	M_7C_3 $(61\bar{7},3)$

* unidentified

TABLE 21

Phase Identification of Hf, Y, and MM*
Modifications to NASAUT 4G-A

Specimen No.	Modification (wt%)	Matrix Phase (Å)	Carbide Phase (Å)
A83-001	-	all γ	M_7C_3 + MC
A83-012	0.1 Hf	mainly γ, trace α	M_7C_3 + MC
A83-013	0.5 Hf	"	"
A83-014	1.0 Hf	"	"
A83-005	0.1 Y	mainly γ, trace α	M_7C_3 + MC
A83-007	0.5 Y	γ(a=3.628) + α(a=2.872)	
A83-008	1.0 Y	mainly γ, trace α	"
A83-027	0.1 MM	mainly γ, some α	M_7C_3 + MC
A83-037	0.5 MM	mainly γ	"
A83-039	1.0 MM	mainly γ	"

* MM is Mischmetal (La + Ce)

TABLE 22

Creep/Stress Rupture Data for NASAUT 4G Modifications [44]

Alloy	Sample	Heat Treat °C hrs	Test Temp °C	Stress ksi	Rup. Life hrs	LMP C=20	RA %	Elong. %
4G-A	612-01	650/100	788	30	>334.7	>43.0	uploaded	to 35 ksi
4G-A	612-01	650/100→ 788/335	788	35	20.2	>40.7	8.8	15.6
4G-A	612-03	650/100	788	40	97.9	40.9	17.1	10.5
4G-A	612-02	650/100	843	20	142.4	44.5	50.6	24.0
4G-B	621-02	650/100	788	35	7.1	39.8	45.0	25.9
4G	625-02	650/100	788	35	17.9	40.6	35.2	18.1
4G-A1	001-02	650/100	788	30	215.6	42.8	uploaded	to 35 ksi
4G-A1	001-02	650/100	788	35	272.0		15.1	7.7
4G-A1	646-02	650/100	788	35	46.2	41.4	33.8	16.5
4G-A1	001-01	650/100	843	20	161.9		uploaded	to 25 ksi
4G-A1	001-01	650/100	843	25	324.3	44.6	3.9	5.6
4G-E	646-03	650/100	788	35	79.3	41.8	32.5	15.3
4G-E	001-03	650/100	843	25	433.5	45.5	10.1	5.8

NASAUT 4G-A and 4G-Al creep-tested at 843°C for 142.4 hrs and 324.3 hrs, respectively, indicated only the presence of $M_{23}C_6$ and MC, as presented in Table 23. Thus, although the rupture properties of NASAUT 4G have been improved, the M_7C_3 carbide was not fully stabilized at the elevated temperatures examined. Increasing the carbon level from 1.5 to 2.0 wt.% for NASAUT modification, 4G-E, resulted in further improvements in rupture life. This chemistry change was not expected to affect the $M_7C_3 \rightarrow M_{23}C_6$ transformation temperature but resulted in an increase in volume percent M_7C_3 initially present in the castings.

E. Investigations Within the Ternary System Iron-Molybdenum-Carbon

The aim of this study was essentially two-fold. Addition of molybdenum to the alloys according to low-cost Fe-Mn-Cr-C was found to be critical for the production of duplex microstructure $\gamma + M_7C_3$, which has been shown in detail previously [61]. Secondly, molybdenum steels or molybdenum-chromium steels, such as 2 1/4Cr-1 Mo are important commercial materials. It is interesting that only very recently [62] more attention has been given to the precise phase equilibria and the identification of phases as well as the kinetics of the precipitation of the various carbides. Astonishingly, no major effort has been made with respect to the precise identification of the so-called ξ-phase (named also molybdenum cementite with a formula specified as "$MoFe_2C$" [38]). It is obvious that because of the complex crystal structure of this phase, and because of the great similarity of the powder pattern of "$MoFe_2C$" with Fe_3C, most prior studies did not elaborate on the Mo-cementite and its influence on the microstructure and precipitation

TABLE 23

Indexed Carbide Powder Patterns from NASAUT 4G-A (A82-612-02)
Exposed 142.4 hrs at 1550°F (Cr-Kα)

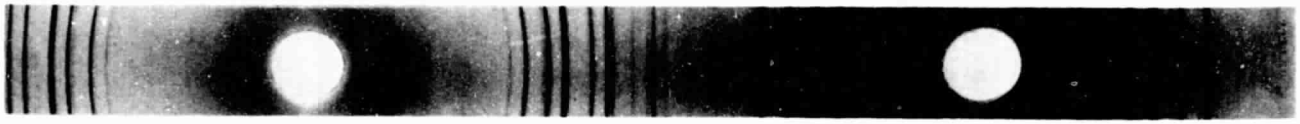

Intensity	θ_{obs}	$\sin^2\theta_{obs}$	Index	Phase	$\sin^2\theta_{calc}$
f	25.8	0.1894	(400)	$M_{23}C_6$	0.1876
m^-	26.9	0.2047	(111)	MC	0.2030
m^+	29.0	0.2350	(420)	$M_{23}C_6$	0.2345
w	31.4	0.2715	(200)	MC	0.2708
m^+	32.0	0.2808	(422)	$M_{23}C_6$	0.2814
vst	34.1	0.3143	(333)(511)	$M_{23}C_6$	0.3165
m	37.8	0.3757	(440)	$M_{23}C_6$	0.3752
m	39.9	0.4115	(531)	$M_{23}C_6$	0.4104
m^-	40.5	0.4218	(600)	$M_{23}C_6$	0.4221
w	43.1	0.4669	(620)	$M_{23}C_6$	0.4690
w	45.15	0.5026	(533)	$M_{23}C_6$	0.5042
m	45.9	0.5157	(622)	$M_{23}C_6$	0.5159

MC; a = 4.40_2Å, M = Nb, Mo

$M_{23}C_6$; a = 10.57_8Å, major amount, M = Cr,Fe,Mn

TABLE 23 (continued)

Indexed Carbide Powder Patterns from NASAUT 4G-A (A82-612-02)
Exposed 142.4 hrs at 1550°C (Cr-Kα)

Intensity	θ_{obs}	$\sin^2\theta_{obs}$	Index	Phase	$\sin^2\theta_{calc}$
w	47.2	0.5384	(220)	MC	0.5415
f	50.5	0.5954	(551)	$M_{23}C_6$	0.5980
vf	54.1	0.6562	(642)	$M_{23}C_6$	0.6566
m^+	59.9	0.7485	(311)	MC	0.7446
m^+	63.0	0.7939	(644)	$M_{23}C_6$	0.7973
f	64.1	0.8092	(222)	MC	0.8123
vst	66.3	0.8384	(660)(822)	$M_{23}C_6$	0.8442
st	69.2	0.8739	(555)(751)	$M_{23}C_6$	0.8794
f	70.2	0.8853	(662)	$M_{23}C_6$	0.8911
m^-	75.05	0.9334	(840)	$M_{23}C_6$	0.9380
m^+	80.0	0.9698	(911)	$M_{23}C_6$	0.9732

MC; a = 4.40_2Å, M = Nb, Mo

$M_{23}C_6$; a = 10.57_8Å, major amount, M = Cr,Fe,Mn

effects [62]. Craig developed a computerized X-ray diffraction technique in order to discriminate Mo-cementite and cementite powder pattern in the presence of both carbides [62]. An expanded diffractogram showing the major peaks of the Mo-cementite can be seen in Figure 14. The investigations so far on the Mo-cementite usually refer to the paper by Dyson and Andrews [63], who reported an indexing of an X-ray powder pattern and some confirmation of these findings by means of electron diffraction technique. The identity of the molybdenum cementite of formula $MoFe_2C$ with the first observation by Kuo [26] was without any doubt. As seen during this work, however, it was clearly shown that the orthorhombic indexing given by Dyson et al [63] cannot be the base for the true cell. The same is true for the proposed space groups. From the present work it is evident that the preparation of pure or almost pure molybdenum cementite is relatively easy and, as was already shown, one can even obtain single crystals from this complex carbide. In these experiments the powder patterns also taken from the crushed single crystal materials could unambiguously be shown to be the same carbide phase. See Table 24 which shows the correct indexing of the powder pattern of the Mo-cementite. Again it should be mentioned that the cell parameters of the Mo-cementite and those given by Dyson and Andrews cannot be simply related [63].

Another point coming out of this work deals with the composition or formula of the Mo-cementite. From wavelength dispersive X-ray analysis (WDX) now also performed on single crystal materials, one must conclude that the amount of carbon in the complex carbide is smaller than 25 at%. The metal/carbon atomic ratio first appeared to be roughly 4.5 instead of 3. A similar observation was also made by Craig. [62] The single

TABLE 24

Powder Data "Mo-Cementite" Cr-Kα(or referred to Cr-Kα)

Index	$\sin^2\theta \times 10^3_{obs}$ (a)	$\sin^2\theta \times 10^3_{obs}$ (b)	$\sin^2\theta \times 10^3_{obs}$ (c)	$\sin^2\theta \times 10^3_{calc}$
(110)($\bar{1}$10)	--	--	--	37.12
(001)	40.5	40.6	--	40.70
($\bar{2}$01)	--	50.9_7	--	50.7_4
($\bar{1}$11)	--	53.2_9	--	53.1_8
(200)	--	--	--	59.3_2
(020)	--	--	--	89.1_8
(111)	--	--	--	102.4_6
($\bar{3}$11)	--	120.5	--	122.5_4
($\bar{2}$02)	--	--	--	123.5_6
(021)	129.7	130.4	--	129.8_8
($\bar{2}$21)	--	138.1	--	139.9_2
(220)	148.3	147.8	150.7	148.4_8
(201)				149.3
($\bar{1}$12)				150.6_4
(310)	--	--	--	155.7_6
(002)	162.6	163.9	--	162.8
($\bar{3}$12)	170.7	171.5	--	170.7_2
($\bar{4}$01)	179.0	181.1	--	179.4_4

TABLE 24 (continued)

Powder Data "Mo-Cementite" Cr-Kα(or referred to Cr-Kα)

Index	$\sin^2\theta \times 10^3_{obs}$ (a)	$\sin^2\theta \times 10^3_{obs}$ (b)	$\sin^2\theta \times 10^3_{obs}$ (c)	$\sin^2\theta \times 10^3_{calc}$
$(\bar{4}02)$	--	--	--	203.0
$(\bar{2}22)$	212.8	213.8	211.2	212.7
(130)	215.0	216.0	217.1	215.4_4
$(\bar{1}31)$	--	--	--	231.5
(400)	237.7	238.8	238.8	237.2_8
(221)}				{238.4_6
(112)	249.1	250.9	252.1	247.2_0
(022)}		253.3		251.9_6}
$(\bar{4}21)$	268.6	270.4	270.0	268.5_8
(311)}				270.3_8
$(\bar{2}03)$	--	--	--	277.7_8
(131)	280.9	283.0	280.7	280.7_8
$(\bar{4}22)$	292.2	294.5	292.6	292.1_2
$(\bar{3}13)$	300.7	300.7	302.4	300.3_1
$(\bar{3}31)$}				300.8_6}
$(\bar{4}03)$	308.0	308.6	308.5	307.9_0
$(\bar{5}12)$}	310.0	313.7	311.1	309.4_4
$(\bar{5}11)$				310.5_4

TABLE 24 (continued)

Powder Data "Mo-Cementite" Cr-Kα(or referred to Cr-Kα)

Index	$\sin^2\theta \times 10^3_{obs}$ (a)	$\sin^2\theta \times 10^3_{obs}$ (b)	$\sin^2\theta \times 10^3_{obs}$ (c)	$\sin^2\theta \times 10^3_{calc}$
(202)	321.4	325.1	320.9	320.6_8
(420)	326.5		329.2	326.4_4
$(\bar{1}32)$	329.2	330.5	329.2	329.0_4
$(\bar{1}13)$}				329.5_0
(330)	334.0	330.5	--	334.0_8
$(\bar{3}32)$	--	--	--	349.0_4
(040)	--	359.2	357.5	356.6_4
(003)	366.9	368.6	367.6	366.3_0
$(\bar{2}23)$}				366.9_4
(401)	--	--	--	376.5_6
$(\bar{5}13)$	--	--	--	389.7_4
(510)	397.8	391.9	400.0	393.0_5
$(\bar{4}23)$				397.0_6
(041)				397.3_4
$(\bar{6}02)$	401.5	--	--	401.0_0
$(\bar{2}41)$	407.8	405.0	--	407.3_8
(222)	409.2	409.9	--	409.8_4
(240)	--	--	--	415.9_6

TABLE 24 (continued)

Powder Data "Mo-Cementite" Cr-Kα(or referred to Cr-Kα)

Index	$\sin^2\theta x10^3_{obs}$ (a)	$\sin^2\theta x10^3_{obs}$ (b)	$\sin^2\theta x10^3_{obs}$ (c)	$\sin^2\theta x10^3_{calc}$
($\bar{6}01$)	427.3	--	492.8	426.7_4
(132)	427.3	--	429.8	427.5
(331)	--	--	--	448.6_1
(023)				455.4_6
($\bar{6}03$)				456.6_6
(421)	466.2	469.3	466.2	465.7_0

TABLE 24 (continued)

Powder Data "Mo-Cementite" Cr-Kα(or referred to Cr-Kα)

Index	$Int._{obs}$ (b)	$\|S\|$ (d)	$Int._{obs}$ (e)	$Int._{calc}$
(110)($\bar{1}$10)	--	18		0.7
(00$\bar{1}$)	5	20	f	4.1
($\bar{2}$01)	--	13		1.1
($\bar{1}$11)	--	14		1.1
(200)	--	19		0.6
(020)	--	15		0.1
(111)	--	15		0.2
($\bar{3}$11)	--	15		0.1
($\bar{2}$02)	--	38		0.8
(021)	10	34		6.3
($\bar{2}$21)	--	24		0.7
(220)	--	38		1.2
(201)	<5	23		0.6
($\bar{1}$12)	--	22		0.6
(310)	--	16		0.1
(002)	<5	38		2.1
($\bar{3}$12)	5	41	w	2.8
($\bar{4}$01)	5	37	w	3.7

TABLE 24 (continued)

Powder Data "Mo-Cementite" Cr-Kα(or referred to Cr-Kα)

Index	$Int._{obs}$ (b)	$\|S\|$ (d)	$Int._{obs}$ (e)	$Int._{calc}$
$(\bar{4}02)$	--	42		0.4
$(\bar{2}22)$	10	226	mw	8.0
(130)	10	248	m	12.4
$(\bar{1}31)$	--	21		0.0
(400)	40	340	mst	19.4
(221)}		38		1.9}
(112)	25	199	m	9.6
(022)}		394		31.6}
$(\bar{4}21)$	70	353	m	18.0
(311)}		319		21.0}
$(\bar{2}03)$	--	49		0.4
(131)	--	397	m	25.1
$(\bar{4}22)$	--	381		20.1
$(\bar{3}13)$		344	st	12.9
$(\bar{3}31)$}		44		55.8}
$(\bar{4}03)$	--	45		30.7
$(\bar{5}12)$}		206		5.3}
$(\bar{5}11)$		297		13.3

TABLE 24 (continued)

Powder Data "Mo-Cementite" Cr-Kα(or referred to Cr-Kα)

Index	$Int._{obs}$ (b)	$\|S\|$ (d)	$Int._{obs}$ (e)	$Int._{calc}$
(202)	--	450	m	19.7
(420)	--	46		3.1
$(\bar{1}32)$		402	m	21.0
$(\bar{1}13)$}		53		4.1}
(330)	--	223		2.5
$(\bar{3}32)$	--	47		0.3
(040)	--	304		5.5
(003)		410	w^+	9.8
$(\bar{2}23)$}		350		12.9}
(401)	--	22		0.2
$(\bar{5}13)$	--	49		0.7
(510)		46		0.7
$(\bar{4}23)$		47		2.4
(041)		53		2.9
$(\bar{6}02)$	--	347		6.7
$(\bar{2}41)$	--	50		0.8
(222)	--	47		1.1
(240)	--	46		0.5

TABLE 24 (continued)

Powder Data "Mo-Cementite" Cr-Kα(or referred to Cr-Kα)

Index	$Int._{obs}$ (b)	$\|S\|$ (d)	$Int._{obs}$ (e)	$Int._{calc}$
($\bar{6}01$)		262		2.9
(132)		14		0.1
(331)		25		0.1
(023)		28		0.3
($\bar{6}03$)	--	29		0.1
(421)	--	297		8.9

(a) - observed in this work

(b) - D. J. Dyson and K. W. Andrews, J.I.S.I., t.191, 1964, p. 258.

(c) - J. C. Schuster, Ph.D. Thesis, Univ. of Vienna, 1977.

(d) - refers to structure factors taken from single crystal intensity data, S. F. Wayne, Ph.D. Thesis, Univ. of Connecticut, 1985.

(e) - observed intensity by (a), (c) and K. Kuo, J.I.S.I., t.173(1953); t.184(1956).

f - faint

w - weak

m - medium

st - strong

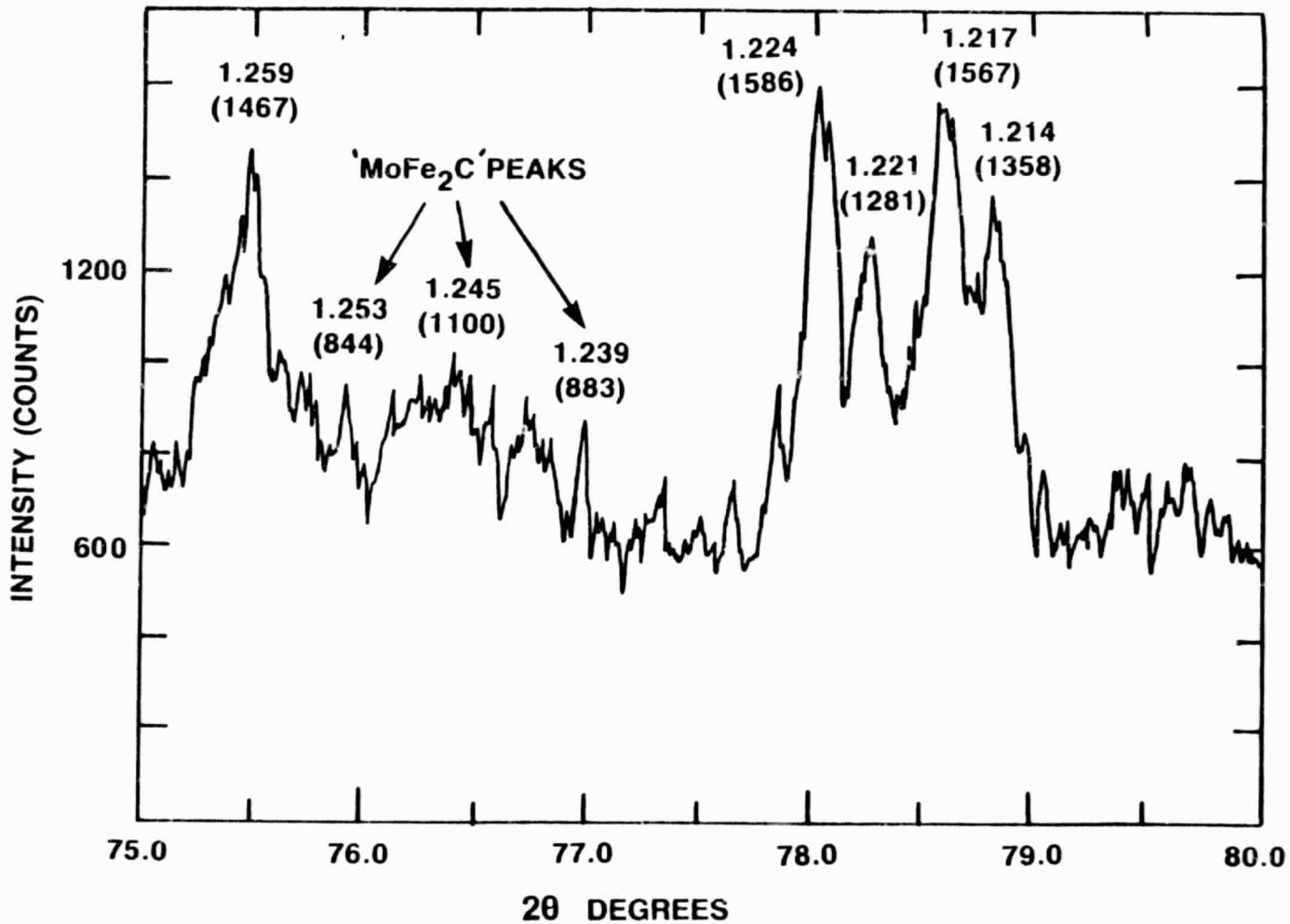

Fig. 14 X-Ray Intensity Profiles for Molybdenum Cementite (ξ carbide) and Cementite Phases, Numbers Represent D-Spacings [62]

crystal analysis also gave a hint for the atomic ratio of molybdenum and iron, which seems to be deviating somewhat from the proposed value, making a somewhat larger ratio (Mo/Fe = 0.523) likely. The discussion about the composition of the Mo-cementite continues in section F.

In the context of the precipitation kinetics, it is remarkable that the presence of niobium, or more specifically NbC in a molybdenum-niobium modified steel enhances the nucleation of the Mo-cementite. [62] One has to add at this point that improved properties of the iron base superalloys Fe-Mn-Cr-Mo-Al(Si)-C are obtained by means of small amounts of niobium [64].

The carbide transformations in high carbon-chromium-molybdenum steels were studied by Inoue and Matsumoto [65] who also determined the orientation relationship for the reactions $M_3C \rightarrow M_7C_3 \rightarrow M_{23}C_6 \rightarrow M_6C$. As the samples were prepared by rapid quenching from melts, no Mo-cementite has been found to occur. However there was no hint made for Mo-cementite in tempered samples at 600 and 700°C either (see Fig. 15).

Cr-Mo-steels, containing 4-14 w% Cr and 0.5-2 w% Mo with 0.1-0.2 w% C besides ca 0.5 w% Mn and up to 0.3 w% V have extensively been investigated with respect to the fringe-type alloy-carbide eutectoids [66]. The occurrence of the carbides M_3C, M_7C_3, $M_{23}C_6$ and M_2X at the fringes (fr.) as a function of $Mo/C_{fr.}$ and $(Cr + Mn)/C_{fr.}$ can be seen from Fig. 16. The M_2X carbide obviously corresponds to the subcarbide, which may have the formula $Mo_{5/3}Fe_{1/3}C$ or $MoCr_{2/3}Fe_{1/3}C$. No Mo-cementite was mentioned to be found in the fringes so far. Furthermore, these authors claim to have found an epitaxial behavior between the nontransformed austenite and the M_7C_3 carbide with (0001) plane of M_7C_3

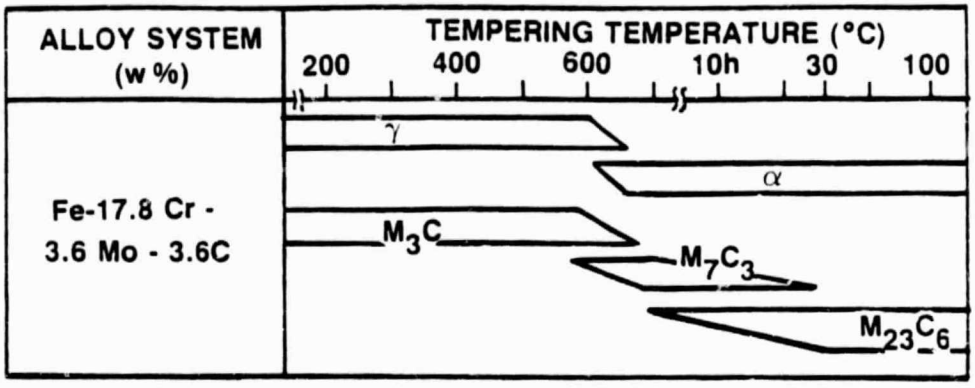

Fig. 15 Structural Changes in Cr-Mo Alloy Steel at Different Temperatures After Rapid Quenching From the Melt [65]

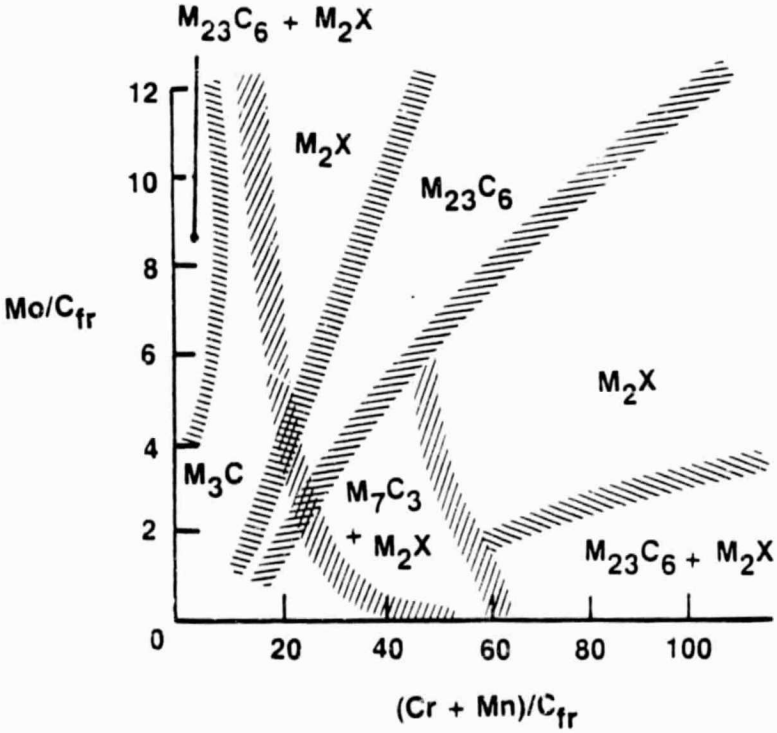

Fig. 16 Occurrence of M_2X, M_3C, M_7C_3 and $M_{23}C_6$ Fringes as a Function of Mo/Cr_{Fringe} $(Cr+Mn)/Cr_{Fringe}$ Ratios [66]

parallel to the (111) plane of γ. From these observations one may conclude that the growth direction $[10\bar{1}0]$ of M_7C_3 is prevailing.

Experiments have also been made studying the behavior of the M_7C_3 carbide after various heat treatments. In particular, an alloy of composition Cr(20)-Mn(10)-C(3.4)-Fe(bal) was selected for determining the stability of the M_7C_3 carbide. It is well known that the transformation of the M_7C_3 carbide into the $M_{23}C_6$ carbide may strongly influence mechanical properties [6]. The samples prepared by D. S. casting (10 cmh^{-1}), were encapsulated in evacuated quartz tubes and heated to 950°C, 1000°C and 1150°C, respectively. It turned out that after tempering at 1150°C for two weeks, no phase change occurred. At any rate, inspection by powder X-ray diffraction was made again on extracted material after 950°C (4 weeks) and the M_7C_3 carbide remained as the stable phase.

The microstructures (etched with Fry's reagent) of directionally solidified materials were found to change with increasing annealing temperatures and time (see Fig. 17). The duplex microstructures at 950°C were quenched into 20°C water, which resulted in the formation of some martensite in the matrix. At 950°C (4 weeks) the M_7C_3 carbide phase remains unchanged with well-defined pseudo-hexagonal morphology. At 1000°C and 1150°C, the samples were furnace-cooled and the γ-matrix was retained although some coarsening of the carbides is evident after two weeks at 1000°C. At 1150°C, the carbide morphology becomes globular after only one week, followed by further coarsening at two weeks. It is interesting that despite the various annealing times and temperatures, the M_7C_3 carbide microhardness increased from 2100 VHN to a maximum of 2650 VHN.

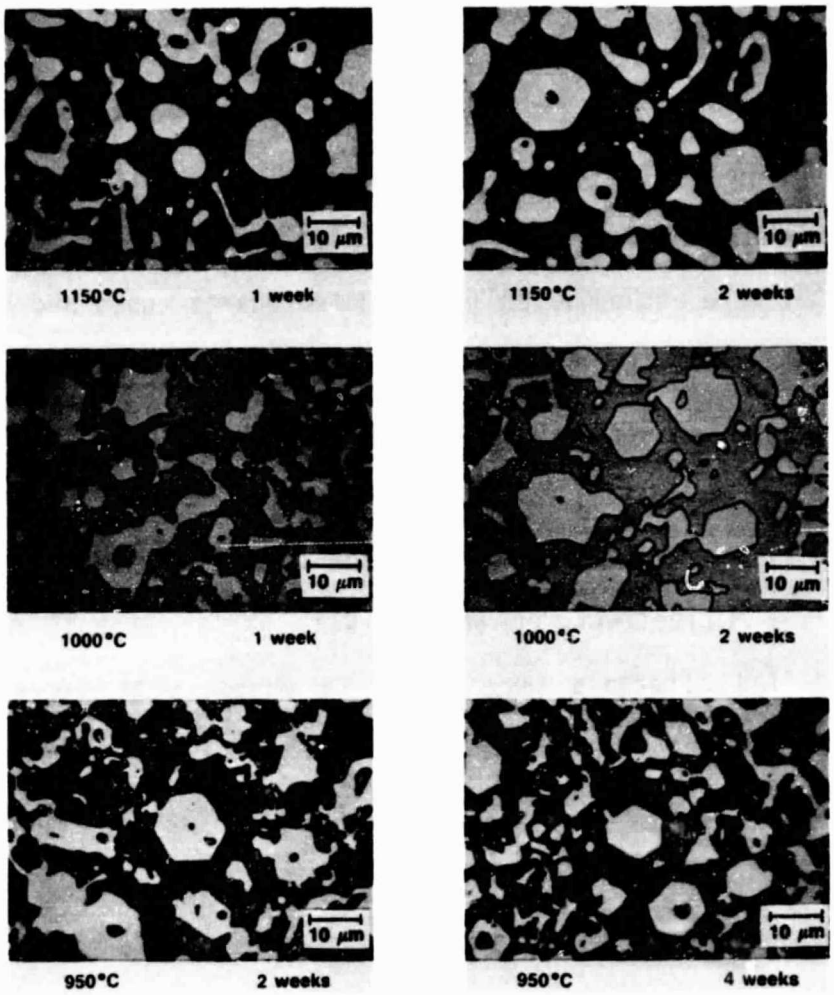

Fig. 17 Light Micrographs, Transverse Sections of Cr(20)-Mn(10)-C(3.4)-Fe(bal), D.S. at 10 cmh^{-1}, Annealed at 950, 1000 and 1150°C

F. Studies on the Molybdenum Cementite phase (ξ carbide)

From a study of the ternary system Fe-Mo-C, a relatively low melting area (1100-1150°C) was found close to the conjugation line "$MoFe_2C$"-Fe. Based on this experimental observation it was assumed that primary crystallization of the Mo-cementite takes place in this vicinity. Following such a concept, powder mixtures of 75.9w%Fe (71a%), 20w% Mo(11a%) and 4.1w%C (18a%) were sintered and placed in an alumina tube and heated to 1500°C (well into the liquid region) for one hour. The sample length of 10cm was exposed to a thermal gradient for 24 hrs with 1150°C as the target for growth of the Mo-cementite in the liquid. The sample was then quenched into 20°C water. While removing the sample from the alumina tube, the solidified bar immediately separated at one point exposing distinct crystals, later established to be the Mo-cementite. The crystals were then extracted in an alcoholic bromine solution and inspected by light microscopy and SEM/WDX analyses to determine the chemical composition. The WDX analysis again confirmed the approximate atomic metal ratio Mo:Fe≈0.5; however, the metal carbon ratio certainly is larger than 3 (Table 25). The single crystals of the Mo-cementite ξ carbide were then inspected with a Gondolfi camera to acquire a powder pattern which would be evaluated and compared to the data of Kuo and Dyson and Andrews (see Table 24). Once confirmed as the Mo-cementite phase, selected single crystals were crushed and placed in a fine focus Guinier X-ray camera (Cu-Kα) for precise evaluation of d spacing and lattice parameters as referred to a silicon internal standard.

The most symmetrical crystals were then mounted for precession camera work using Mo-Kα. Alignment of the crystals revealed a mirror

TABLE 25

WDX Analysis of Molybdenum Cementite Single Crystals (atomic concentrations)

	Location (*)				
Element	Area 1	Area 2	Area 3	Area 4	Area 5
C	.179	.197	.142	.177	.151
Fe	.569	.583	.590	.572	.583
Mo	.272	.285	.274	.277	.280

(*) 12 x 12 μm scanning area

plane and two 90° angles in the cell. Precession camera photographs were taken of the zero levels (see Figs. 18 and 19) which established the (0kl) and (h0l) reflections along the two unique directions. In order to record the upper level reflections, a cone axis photograph (Laue cone axis) was taken and is shown in Fig. 20. This figure provides information about the crystal symmetry, and the symmetry of each ring of the photograph is the Friedel symmetry of the corresponding level of the reciprocal lattice [71]. Figure 20 contains the zero level (smallest diameter ring) and upper levels 1, 2, 3, and 4. Based on the diameter of each ring, a value for ζ [71] was calculated and used to position the camera forward and obtain the upper-level precession photographs. The precession photographs were then indexed with the observed reflections intensity leading to the determination of the systematic absences in the cell. The conditions limiting possible reflections were for the general positions hkl: (h+k=2n), h0l: (h=2n), and for 0k0: (k=2n), thus the space group assignment was made to C2/m or C2/c each with the b axis unique. It should be noted that at this point it was not possible to discern between these monoclinic space groups because the same conditions are satisfied in each case; the C2/m was chosen, however, because of its higher symmetry. It was then possible to completely index the reflections (single crystal and Guinier data) and the resulting cell parameters for the monoclinic cell were derived: a = 10.870, b = 7.671, c = 6.563 Å and β = 120.1°.

The molybdenum cementite single crystal was then placed in a Picker four-circle diffractometer employing Mo-Kα radiation. This automated

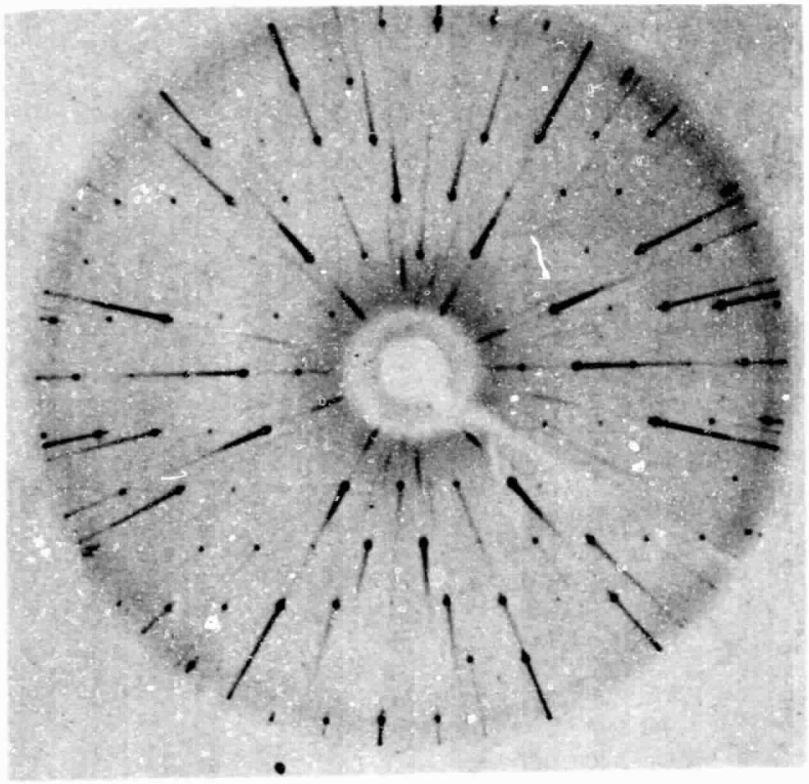

Fig. 18 Precession Camera Photograph of a Mo-Cementite Single Crystal, Zero Layer, (h0l) Reflections, Mo-Kα

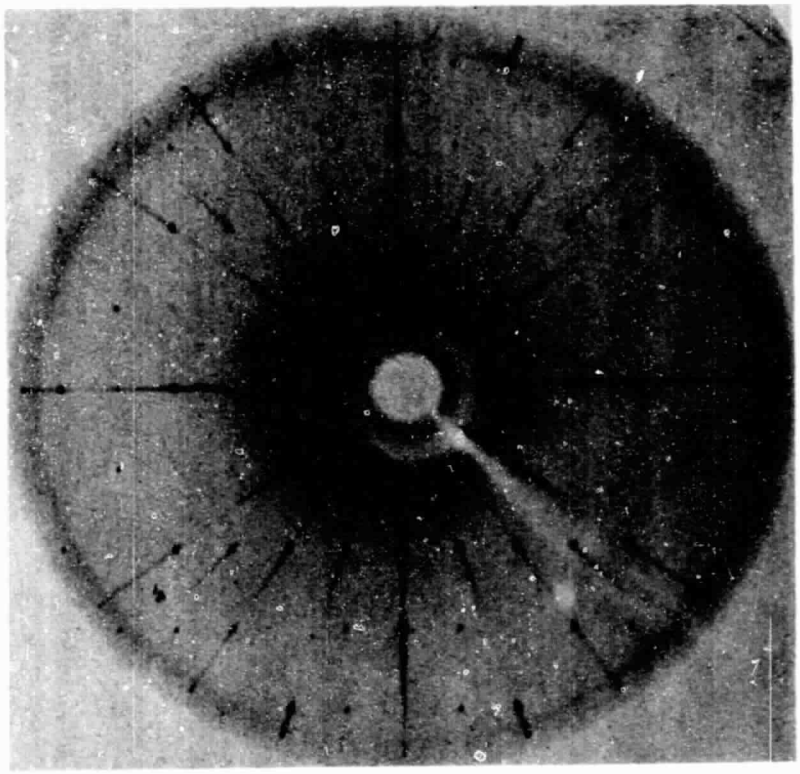

Fig. 19 As Fig. 18, (0kl) Reflections

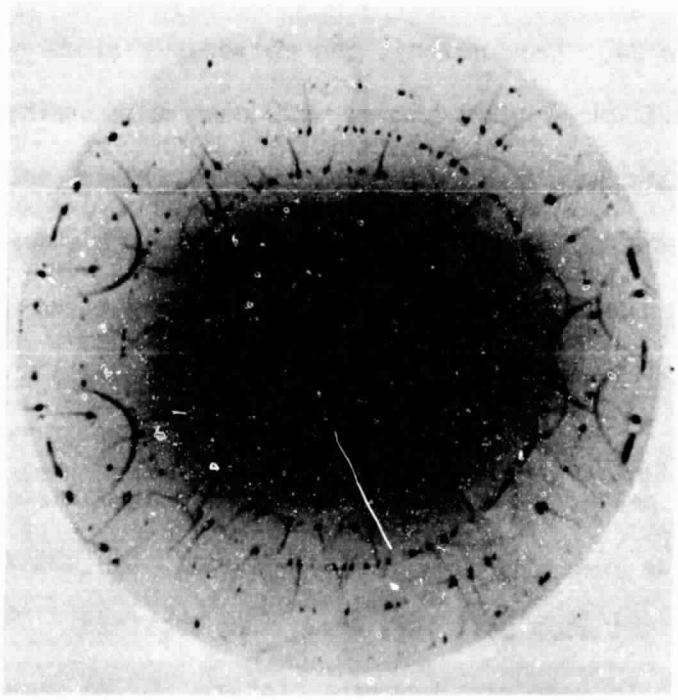

Fig. 20 Laue Cone Axis Photograph of a Mo-Cementite Single Crystal
Mo-Kα

diffractometer collected intensity data for ca 1200 reflections by performing a 2θ scan. As the size and shape of the crystal was small and irregular, an absorption correction was applied to the data set.

The raw intensities were placed into a series of crystallographic computer programs, from which a set of structure factors corrected for background were computed, thus removing the 2θ dependency. A Patterson map was then produced revealing the interatomic vectors between peaks whose intensity is proportional to the product of the number of electrons in each of the two atoms involved. The Patterson map was set up by uniformly "slicing" the UVW vector space (b axis unique) as u/48, v/24 and w/24. Knowing that the molybdenum atoms have an electron density of 1.5 times that of Fe, the heavy-atom method of locating Mo-Mo self vectors was applied. Subsequently, Mo-Fe and Fe-Fe vectors each having reduced Patterson map intensity were located. From such an approach, the "atomic" coordinates were derived and arrangements of (repeat units) were sought. Based on these positions, structure factors were then calculated and compared with the observed structure factors until the phases were determined. With good agreement between structure factors, an electron density (difference) map was produced and the remaining light atom positions were then obtained.

Prior to complete determination of the Mo-cementite crystal structure, some doubts existed as to the correct formula for this complex carbide. From the WDX data (Table 25) it turns out that the amount of carbon is definitely smaller than for "$MoFe_2C$".

The number of atoms in the Mo-cementite (ξ phase) can be inferred from the density, estimated to lie between Fe_3C (ρ = 7.71 g/cm^3) and

Mo_3Fe_3C (ρ = 9.00 g/cm^3). As there were not a sufficient number of single crystals for a measurement in a 2ml pycnometer, an estimated value was obtained by interpolation at both the density for Fe_3C and Mo_3Fe_3C. A formula of $Mo_3Fe_6C_2$ seemed to be appropriate. It became evident that in addition to the deficiency of carbon atoms from the stoichometric composition, there could be a mixing (substitution) of Fe and Mo atoms in some atomic positions.

The final reduction of the single crystal data led to a crystal structure solution which had a residual factor of about 6%. Table 24 represents the calculated intensities for the powder pattern of the Mo-cementite. Figure 21A shows the carbon atom which fills the trigonal prismatic void in the smaller metal (mainly Fe) environment. In the case of the larger (preferential Mo) atom environment (Figure 21B), the carbon occupies the octahedral voids. Figure 21C shows the bonding arrangement for the Fe1 centrosymmetric special positions in the crystal structure. This configuration can be described as a "trigonal anti-prism" with Fe1 as the center of symmetry. Figures 22A and 22B are the repeat layers that describe the structure. The X positions are voids which align themselves above or below the Fe1 atoms. The combination of these displaced layers is shown in Figure 23, which accurately depicts the assembled crystal structure. Interestingly, one edge of the tri-capped trigonal prism is shared between layers, whereby the octahedra share vertices (corners) only. Some of the octahedral caps appear to be shared between layers. The edge of the trigonal prism, with regard to the chemical composition of the molybdenum cementite phase, $M_{34}C_{10}$ ($Mo_{12}Fe_{22}C_{10}$), meets the requirements of ratio of metal/carbon larger

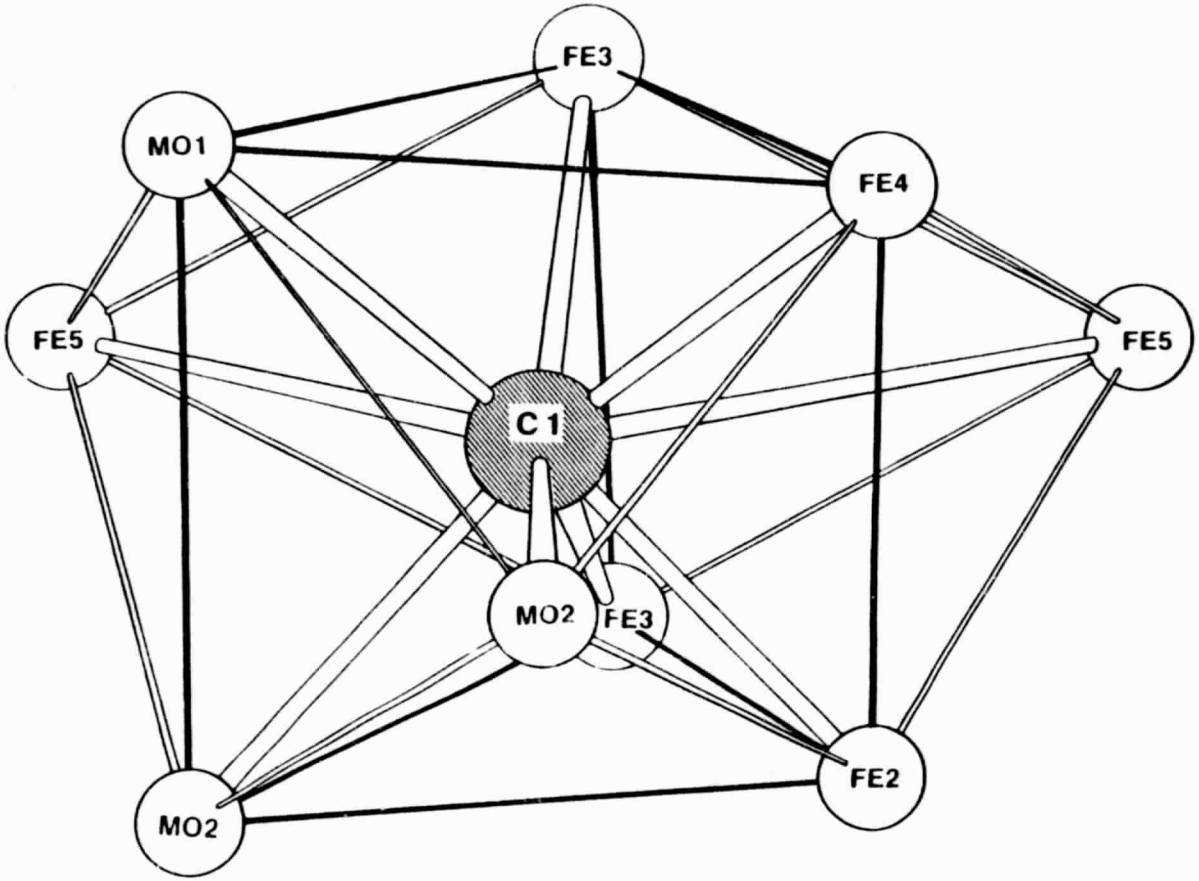

Fig. 21A Small Metal (Preferential Fe) Environment Showing Carbon Atom in Trigonal Prismatic Void

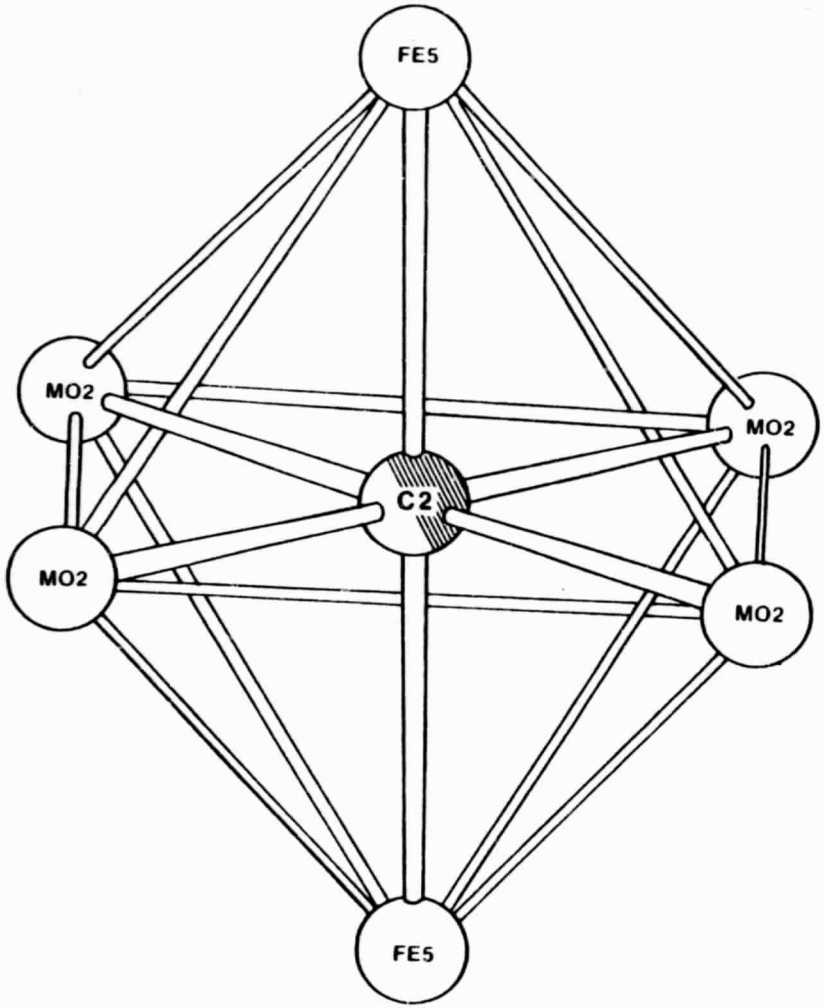

Fig. 21B Large Metal (preferential Mo) Environment Showing Carbon Atom in Octahedral Void

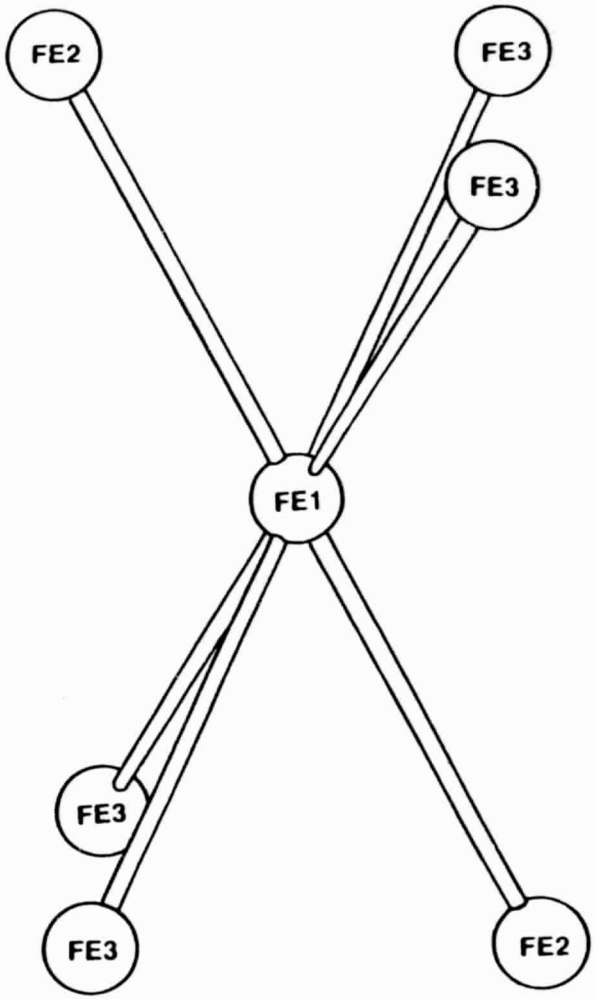

Fig. 21C Bonding Arrangement for the Fel Centrosymmetric Special Positions

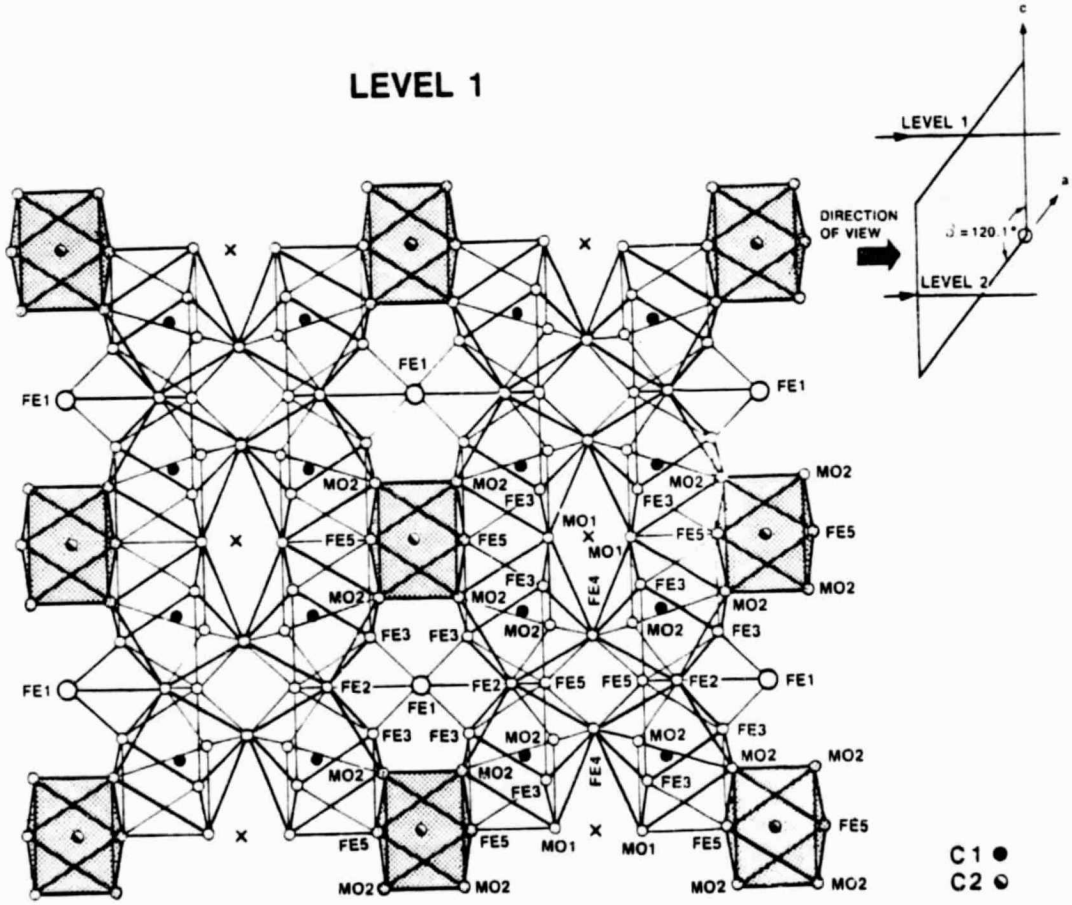

Fig. 22A Atomic Arrangement of Molybdenum Cementite (ξ carbide), Level 1

LEVEL 2

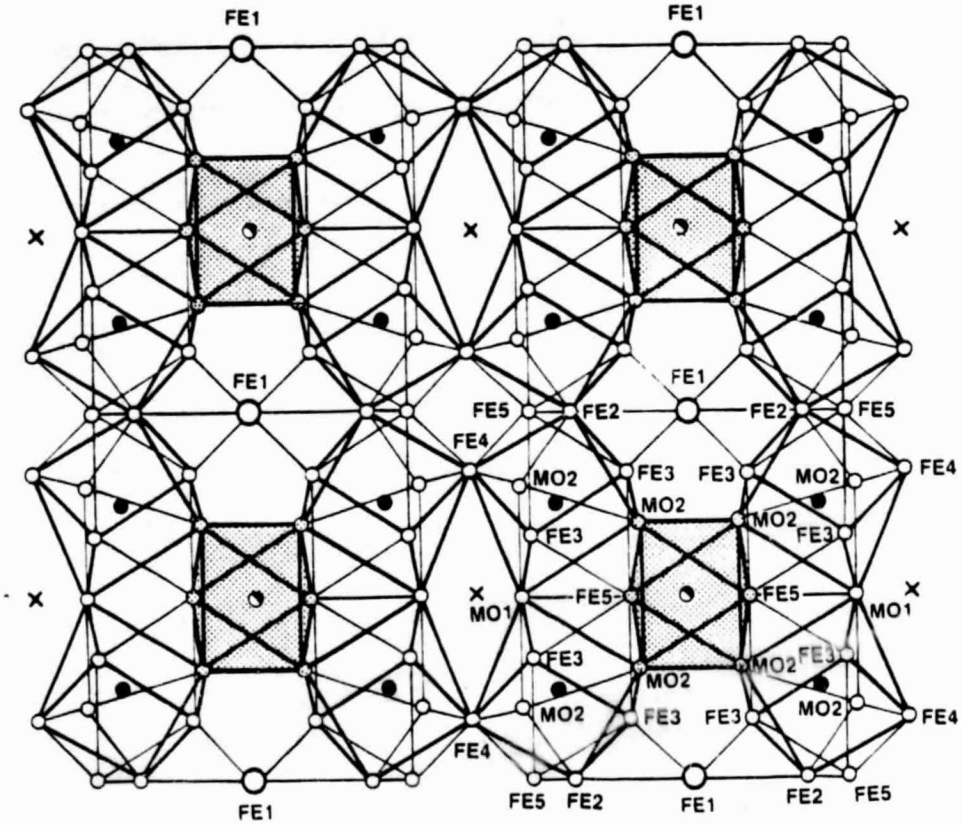

Fig. 22B As Fig. 21A, Level 2

CRYSTAL STRUCTURE FOR MOLYBDENUM CEMENTITE

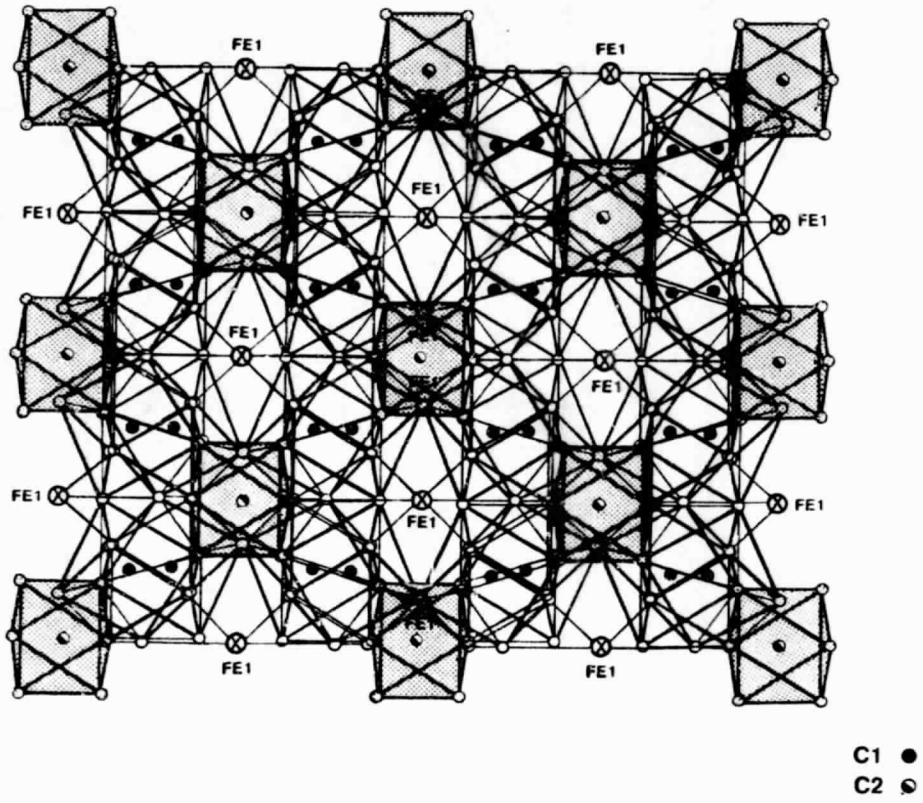

Fig. 23 Combined Atomic Arrangement (Level 1 plus Level 2), ξ Carbide

than 3 and Mo/Fe somewhat larger than 2. Furthermore, it is clear that an iron atom could not fit on the (0,0,0) carbon site. The question of a mixing of Fe and Mo atoms in some of the atomic positions is not necessary as a satisfactory residual was obtained with an ordered state.

Attempts to form large (1 cm^3) arc melted buttons of the ξ phase led to formation of the highly stable Mo_2C and α-Fe phases for various compositions (see Table 26). Figure 24A shows the arc melted and annealed microstructures of four compositions expected to produce the Mo-cementite phase. Powder X-ray diffraction of the arc-melted buttons revealed the stable Mo_2C phase in an α-Fe matrix. Subsequent vacuum encapsulation of the arc melted buttons and annealing at 900°C for one week produced changes in the duplex microstructures (see Fig. 24A). An interesting observation was made when the encapsulated samples were removed from the furnace when upon cooling, bright-metallic crystallites nucleated and grew on the inner tube surface, no doubt a result of vapor transport from the hot sample to the cooling tube surface. X-ray inspection of the particles from each composition surprisingly showed the strong presence of Fe_3C and highly crystallized α-Fe phases. Light microscope inspection of the nucleated crystals revealed needle-like shapes (whiskers) with some regularly faceted crystallites.

To better understand the Fe-Mo-C phase equilibria, melting point measurements were made for numerous compositions. These ternary alloy melting point measurements were made in a Pirani furnace and used in combination with the literature data (binary and ternary alloys) to construct a theoretical melting surface. The phase field of the Mo-cementite appears as a wide plateau existing at 1100-1150°C. Of

TABLE 26

Arc-Melted Alloy, Mo(45)-Fe(50.3)-C(4.7) Cr-Kα Radiation

Intensity	θ_{obs}	$\sin^2\theta$ obs	Index	Phase	$\sin^2\theta$ obs
vw	26.4	.1977	$(10\bar{1}0)$	Mo_2C	0.1970
vw	29.4	.2410	(0002)	Mo_2C	0.2333
mst	30.5	.2576	$(10\bar{1}1)$	Mo_2C	0.2553
vst	34.5	.3208	(110)	α-Fe	0.3198
vw	41.	.4304	$(10\bar{1}2)$	Mo_2C	0.4303
w^+	50.2	.5902	$(11\bar{2}0)$	Mo_2C	0.5909
m^-	53.0	.6378	(200)	α-Fe	0.6396
w^+	58.4	.7254	$(10\bar{1}3)$	Mo_2C	0.7220
m	64.8	.8187	$(11\bar{2}2)$	Mo_2C	0.8242
w	66.3	.8384	$(20\bar{2}1)$	Mo_2C	0.8462
vst	78.5	.9602	(211)	α-Fe	0.9594

α-Fe: $a = 2.86_4$ Å

Mo_2C: $a = 4.74_2$ Å

$c = 2.98_0$ Å

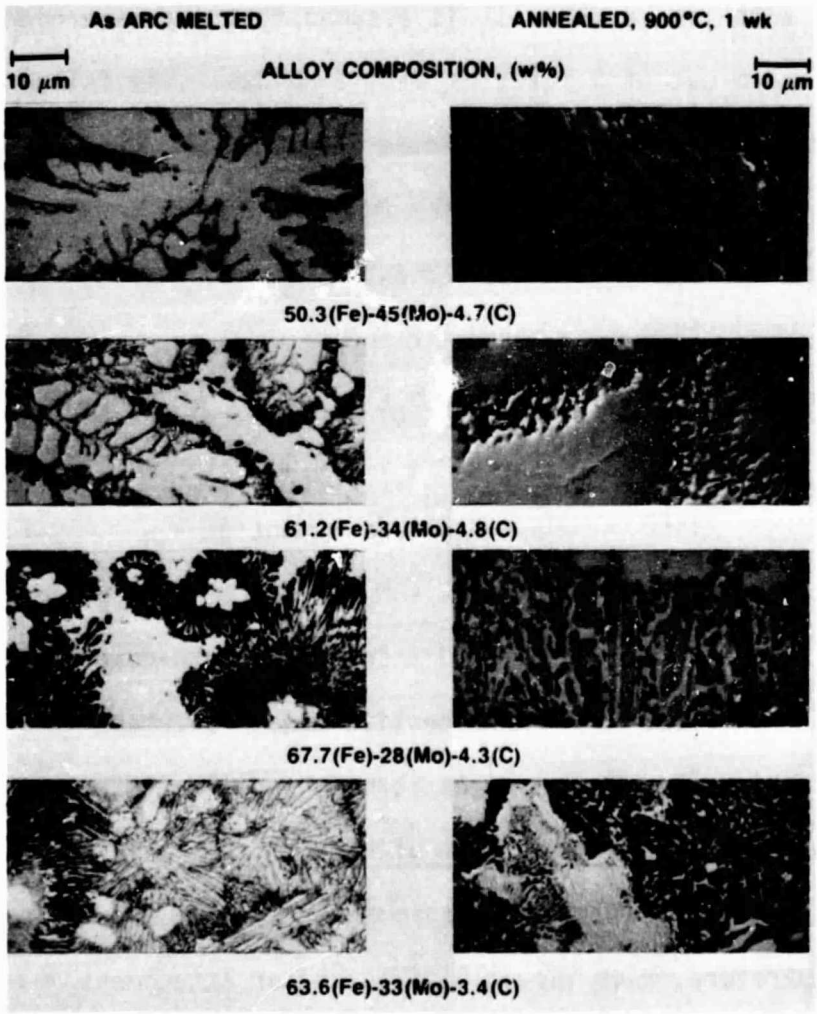

Fig. 24A Light Micrographs, of Arc-Melted and Annealed Microstructures of Four Fe-Mo-C Alloys

considerable importance is the observation that between the composition Fe_3C and Mo_2C exists the Mo-cementite field, and furthermore, the composition of the Mo-cementite lies close to the conjugation line between the very stable molybdenum carbide and γ-iron. Based on the most recent literature data for the binary systems Mo-Fe, Fe-C and Mo-C and the ternary combination [72], the liquidus surface is by and large consistent with Figure 24B. It is assumed that the τ-carbide ($Fe_{21}Mo_2C_6$) does not form out of a reaction with liquidus. The following reactions with liquidus (ℓ) are likely to take place:

1470°C	$\ell + M_2C = Mo(s.s.) + M_6C$
1410	$\ell + Mo(s.s.) = M_6C + \sigma$
1360	$\ell + \sigma = R + M_6C$
1270	$\ell + R = M_6C + \alpha$
1210	$\ell + \alpha = \gamma + M_6C$
1150	$\ell + M_6C$ = Mo-cementite + γ
1140	$\ell + M_2C = M_6C$ + Mo-cementite
1130	$\ell = M_2C$ + Cementite + Mo-cementite
1080	ℓ = Cementite + γ + Mo-cementite

τ-carbide ($Fe_{21}Mo_2C_6$) might form in a solid state (eutectoid) reaction.

G. Thermal Expansion of M_7C_3 and Fe-Based Superalloys

The X-ray camera used in this study was the Norelco X-86-NII High Temperature, High Vacuum Diffractometer Attachment made by the MRC manufacturing corporation. The camera contains a platinum ribbon element which is resistance heated in a vacuum (5×10^{-6} Torr) by an AC power source; Cu-Kα was used throughout this investigation. The diffractometer scanning rate was 1°/min with the maximum 2θ of 110 degrees.

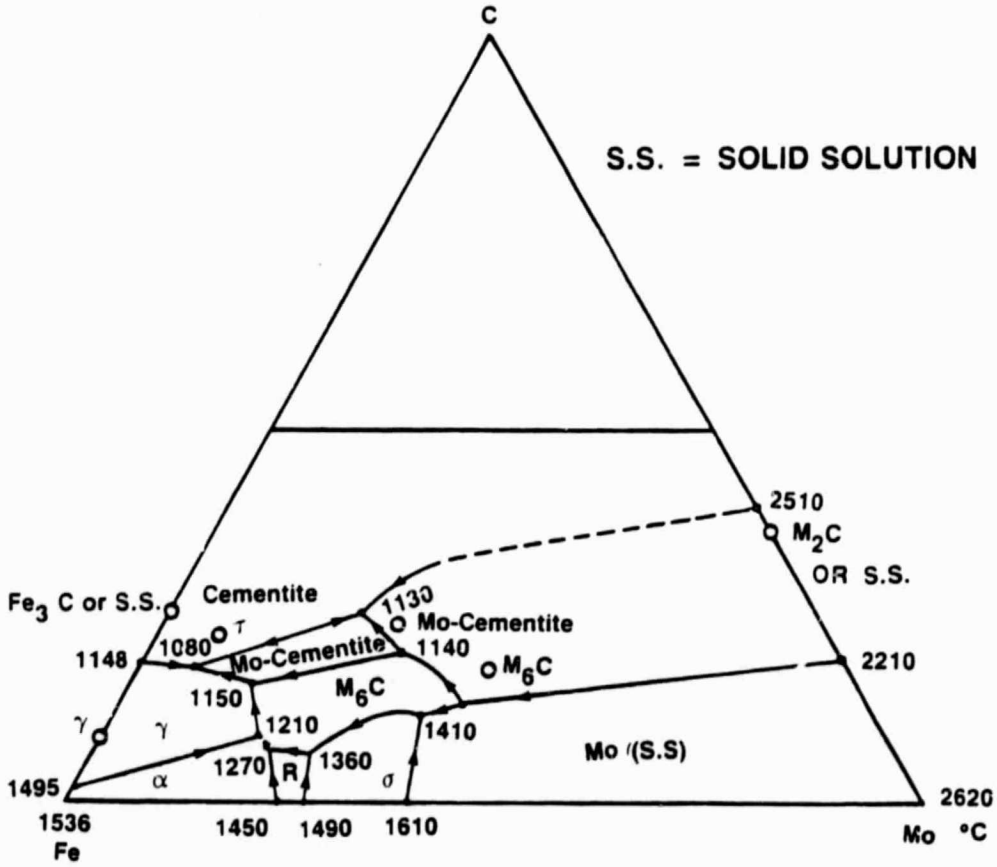

Fig. 24B The Liquidus Surface for the Fe-Mo-C System

Specimen temperature was monitored continuously by a chromel-alumel thermocouple with digital readout. The temperature stability of the heating element was found to be $\pm$ 2°C between 20°C and 1000°C.

The heating rate for each specimen was approximately 200°C/min with a one-hour stabilization period at each level of temperature. The procedure for thermal cycling in this work was as follows:

1) record reflections at room temperature without prior heating,
2) heat to desired temperature level, obtain data, and return to room temperature to ascertain that the sample is unchanged, etc.

The diffractogram data are then indexed with the final cell metrics (volume) determined by a computer program which uses satisfactorily indexed peaks to compute new cell parameters by least square refinement [67].

Thermal expansion coefficient measurements were made for extracted M_7C_3 carbides. The initial composition was 20w%Cr, 10w%Mn, 3.4w%C balance Fe. The bars were directionally solidified at 25 cmh^{-1}. As was shown previously, the carbide will be enriched in chromium, while manganese enters the austenite phase [61, 68]. Thus, for the above-mentioned initial composition, the carbide composition for chromium and manganese is to be 45 and 10w%, respectively, which compares well with EDAX analysis for these two elements [3]. The lattice parameters for the extracted M_7C_3 carbide was found to be a = 13.92 and c = 4.52 Å, values which are close to those for an arc melted alloy of composition $Fe_{11.5}Mn_{2.9}Cr_{8.6}C_6$ consisting of M_7C_3 and γ. It has to be mentioned that the evaluation of the c-axis always displays some scattering [68, 3].

The lattice parameters depending on temperature are shown in Fig. 25. The linear expansion for the a-axis and c-axis differ remarkably; this means that the thermal expansion of the M_7C_3 carbide is highly anisotropical. The thermal expansion coefficient is shown in Fig. 26. As compared to the thermal expansion of cementite (Fe_3C), the anisotropy of the M_7C_3 carbide is much more pronounced. Nevertheless, the linear (average) expansion coefficient lies between 8 to 11 x 10^{-6} deg^{-1} and is in the vicinity of cementite and $(Fe_{1-x}Mn_x)_3C$ [69].

Thermal expansion coefficient measurements were also carried out for the composite alloy Cr(20)-Mn(10)-C(3.4)-Fe (bal) in the chill cast state (Fig. 27). A value of 22.1 x 10^{-6} deg^{-1} was found for a solid sample which can be considered as a random distribution of the M_7C_3 carbide in the γ-matrix. It compares relatively well with an extrapolated thermal expansion coefficient for pure γ and austenite (having 0.81w% carbon) [70].

The M_7C_3 carbide extraction, which was done as previously described [68] was examined by SEM. From Fig. 28 one can clearly see the oriented bundles of the M_7C_3 fibers. The conclusion can be made that the length of the fibers may go up to 500 µm or more. In order to find out the orientation of these carbides particularly relative to the matrix, an isolated carbide fiber was rotated in an X-ray powder camera with the growth direction perpendicular to the X-ray beam. The powder pattern which resulted is shown in Fig. 29A; the evaluation is listed in Table 27. The strong preferred crystallographic orientation is obvious. The indices (equator) are seen to be of the (hkio) type as expected. This is evidence for c-axis alignment of the M_7C_3 in the growth direction of

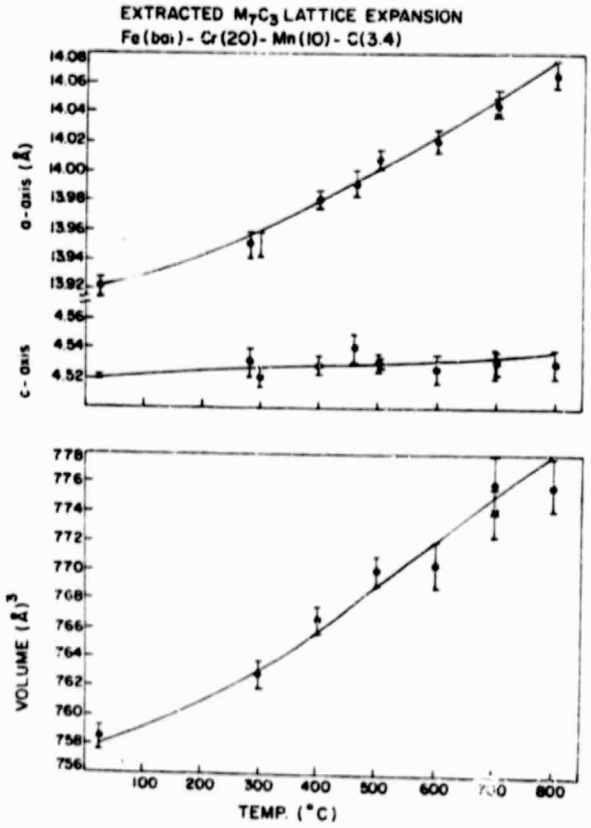

Fig. 25 Thermal Expansion of Extracted M_7C_3 Carbide, Lattice Parameters vs. Temperature

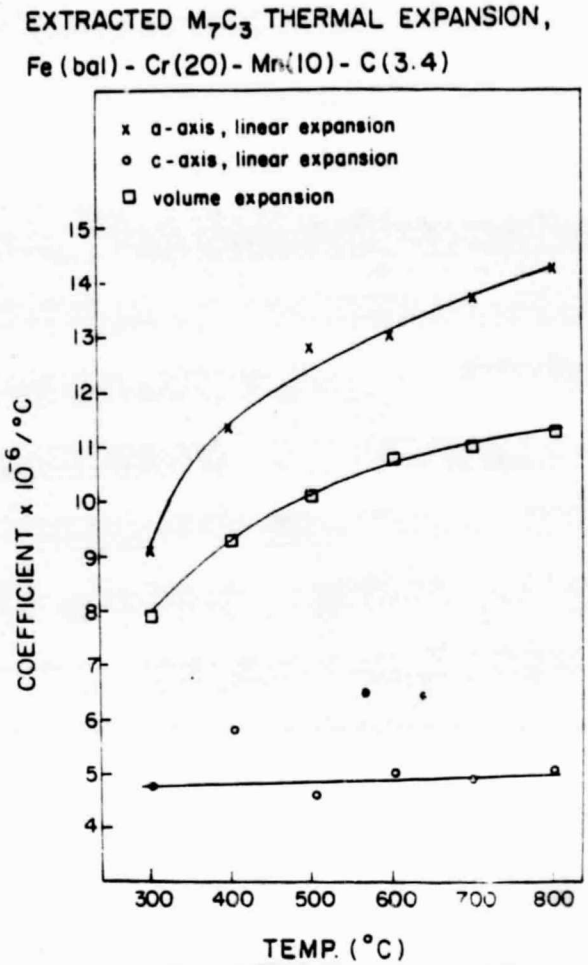

Fig. 26 Coefficients of Thermal Expansion for Extracted M_7C_3 Carbide

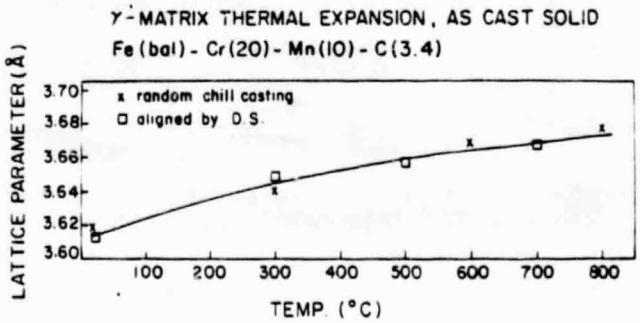

Fig. 27 Thermal Expansion of Cast Alloy Cr(20)Mn(10)C(3.4)Fe(bal)

γ-Matrix Lattice Parameter vs. Temperature

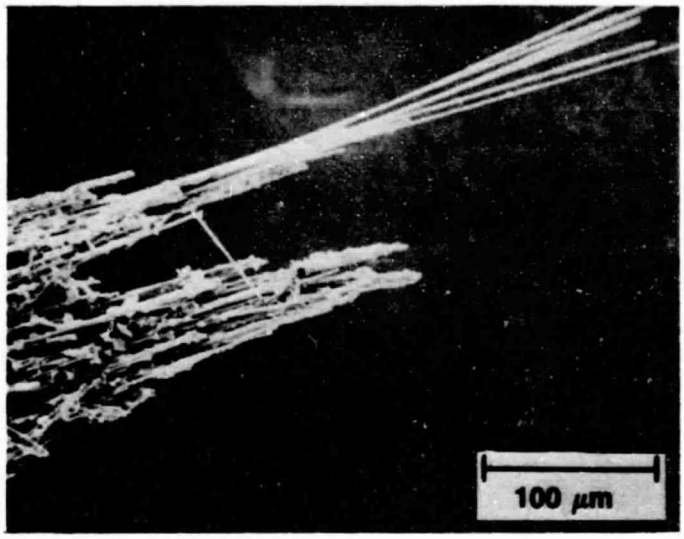

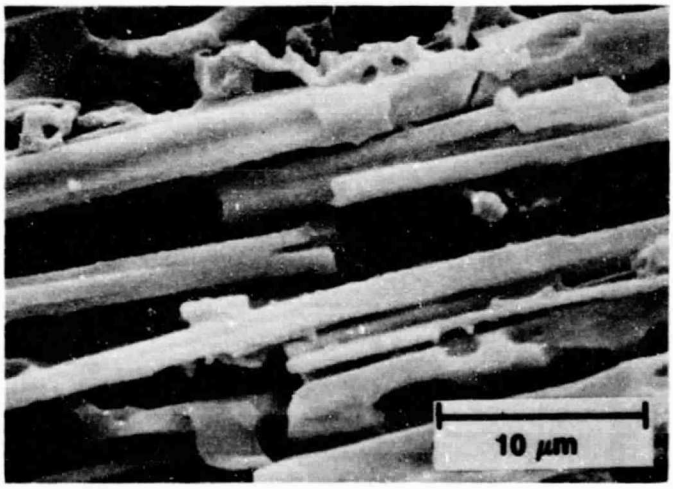

Fig. 28 Scanning Electron Micrographs of Extracted Carbide Fibers Produced by Directional Solidification

TABLE 27

Texture of Extracted M_7C_3 Fibers Fe(bal)-Cr(20)-Mn(10)-C(3.4),Cr-Kα

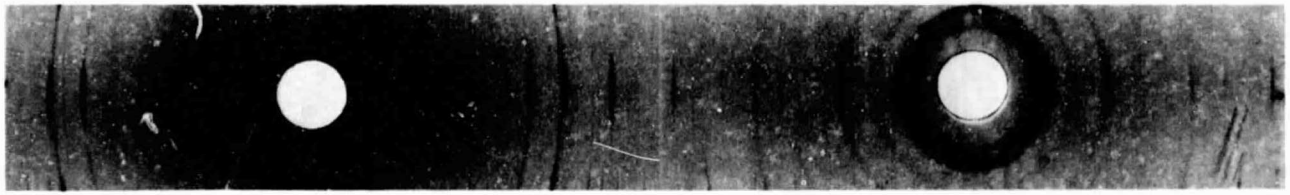

Fig. 29A X-Ray Powder Pattern of Isolated M_7C_3 Carbide Fiber, see Table 27

Equator Intensity	θ_{obs}	$\sin^2 \theta_{obs}$	Index	$\sin^2 \theta_{calc}$
w	10.9	.0358	$(20\bar{2}0)$	.0362
m	22.4	.1452	$(40\bar{4}0)$	.1449
vst	30.2	.2530	$(42\bar{6}0)$	.2536
st	34.9	.3273	$(60\bar{6}0)$	.3260
st	41.3	.4356	$(44\bar{8}0)$	.4349
w_+	43.4	.4721	$(62\bar{8}0)$	.4710
w^+	49.6	.5799	$(80\bar{8}0)$	.5799
w	56.0	.6873	$(64\bar{10}0)$	.6884
m	60.8	.7620	$(82\bar{10}0)$	.7609
vst,b	72.0	.9045	$(100\bar{10}0)$	.9058
vst,b	81.3	.9771	$(66\bar{12}0)$	.9782

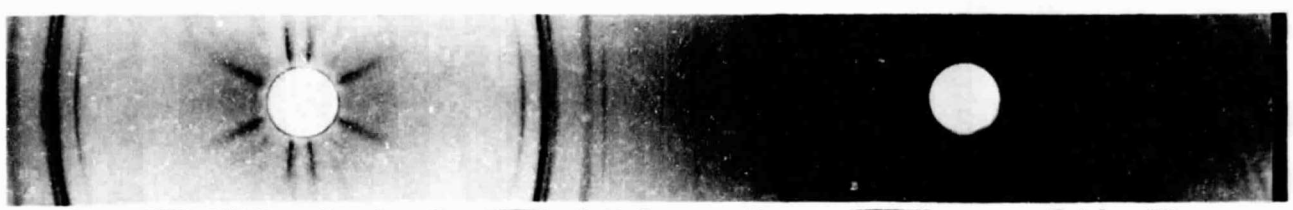

Fig. 29B X-Ray Powder Pattern of M_7C_3 in γ Matrix Needle, see Table 27

the directionally solidified (D.S.) material. In addition, a needle-shaped part of the alloy was diamond-machined from a D.S. bar and again oriented, by and large, parallel to the carbide c-axis. The X-ray pattern, Fig. 29B, confirms the orientation of the carbide fibers; however, it demonstrates a wider scattering of the orientation. The feature of the γ-matrix is much less pronounced; nevertheless, an epitaxial intergrowth is visible. A more detailed examination was made from transverse sections of Cr(20)-Mn(10)-C(3.4)-Fe(bal) processed at 5 cmh^{-1}. Figure 30 is a transmission electron micrograph showing the faceted carbide grains in the γ-Fe matrix. As expected, the interface between the matrix and carbide is a highly dislocated region reflecting the lattice mismatch. Also shown in Fig. 30 is the selected area diffraction pattern (SAD), which contains diffraction spots from both the carbide and the matrix. Dr. D. D. Pearson has determined that the c-axis of the carbide is aligned parallel to the [112] matrix direction.

With respect to directional solidification, various alloys with changing chemistry have been inspected for different growth rates, as seen in Table 28. The main result is that good alignment vanishes if the amount of molybdenum or aluminum is relatively high. Examples of microstructures for alloys having fairly large amounts of aluminum and/or molybdenum with poor alignment are seen in Figs. 31 and 32. These additions were made in an early state of the development of iron-based superalloys, when the improvement of high temperature mechanical and corrosion resistance was recognized as a major aim [68]. For comparison, Fig. 33 shows well-defined carbide fibers as hexagons in the transverse section of the alloy Cr(20)-Mn(10)-C(3.4)-Fe(bal) directionally solidified at 10 cmh^{-1}. Microhardness measurements for the M_7C_3

Fig. 30 TEM Photomicrograph of Directionally Solidified Cr(20)-Mn(10)-C(3.4)-Fe(bal) Processed at 5 cmh^{-1}; Transverse Section

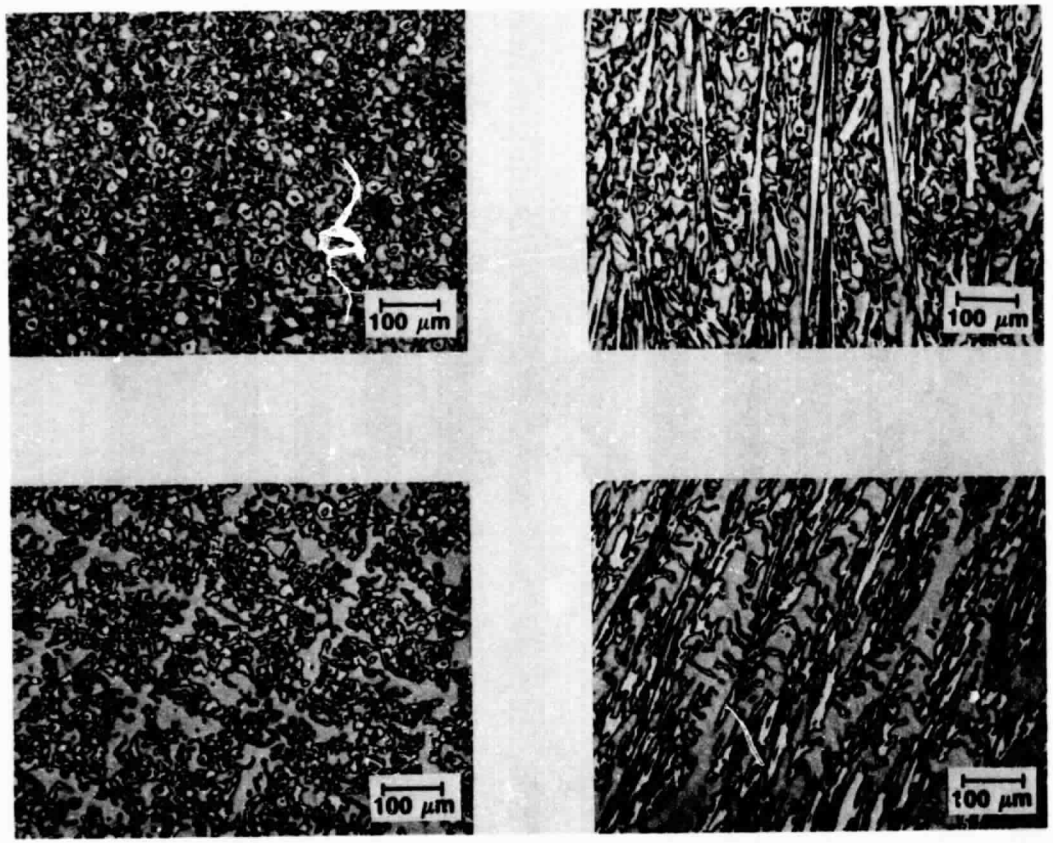

A83-299

3 cmh^{-1}

A83-202

3 cmh^{-1}

TRANSVERSE

LONGITUDINAL

Fig. 31 Light Micrographs of Alloy A83-200, and A83-202, 3 cmh^{-1}

Transverse and Longitudinal Sections, see Table 28

TABLE 28

Composition, Growth Rates and Microhardness of Directionally Solidified Alloys

Alloy designation	Composition wt. %							
	Fe	Cr	Mn	Al	Mo	Si	C	Nb
A83-031	64.3	15	15	2.5	--	--	3.2	--
A83-033	66.8	15	15	--	--	--	3.2	--
A83-034	64.2	15	15	2.0	2.0	1.0	2.8	--
A83-093	63	12	15	--	2.0	5.0	3.0	--
A83-096	64	12	15	--	2.0	5.0	2.0	--
A83-101	64	12	15	4.0	2.0	1.0	2.0	--
A83-116	63	12	15	4.0	2.0	1.0	3.0	--
A83-127	69	12	15	--	3.0	--	1.0	--
A83-128	69	12	15	--	3.0	--	1.0	--
A83-129	65	15	15	--	2.0	1.0	1.0	1.0
A83-130	65	15	15	--	2.0	1.0	1.0	1.0
A83-200	64.8	12	15	--	2.0	3.0	3.2	--
A83-202	62.8	12	15	4.0	2.0	1.0	3.2	--
A83-204	64.3	12	15	2.5	2.0	1.0	3.2	--
A83-206	64.3	12	15	--	2.0	3.5	3.2	--

TABLE 28 (continued)

Composition, Growth Rates and Microhardness of Directionally Solidified Alloys

Alloy designation	Growth rate (cmh^{-1})	Microhardness Vickers (VHN)	
		Matrix	Carbide
A83-031	10	400**	2,100*
A83-033	10	475**	2,100
A83-034	10	400**	2,100*
A83-093	10	--	--
A83-096	10	--	--
A83-101	10	--	--
A83-116	10	--	--
A83-127	25	300**	--
A83-128	25	290**	--
A83-129	25	325**	--
A83-130	25	325**	--
A83-200	3	350*	1,800*
A83-202	3	350*	1,800*
A83-204	3	400*	1,800*
A83-206	3	400*	1,800*

* 50 gm load
** 1000 gm load

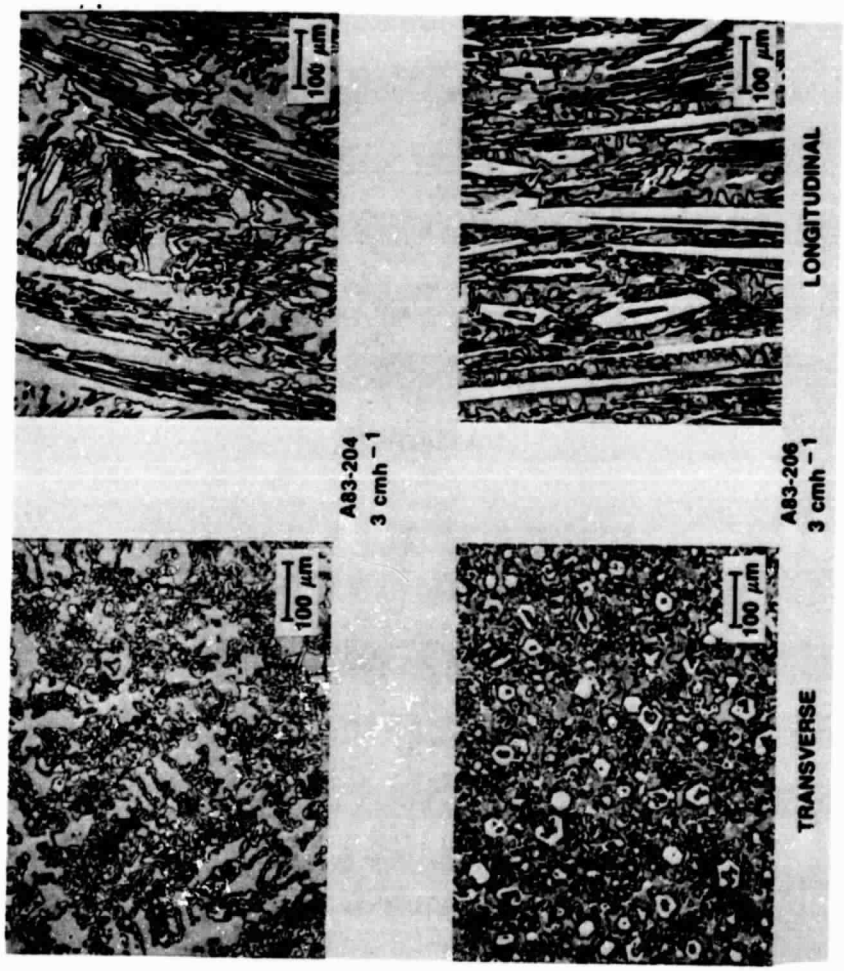

Fig. 32 As Figure 31, Alloy A83-204, and A83-206, 3 cmh^{-1}

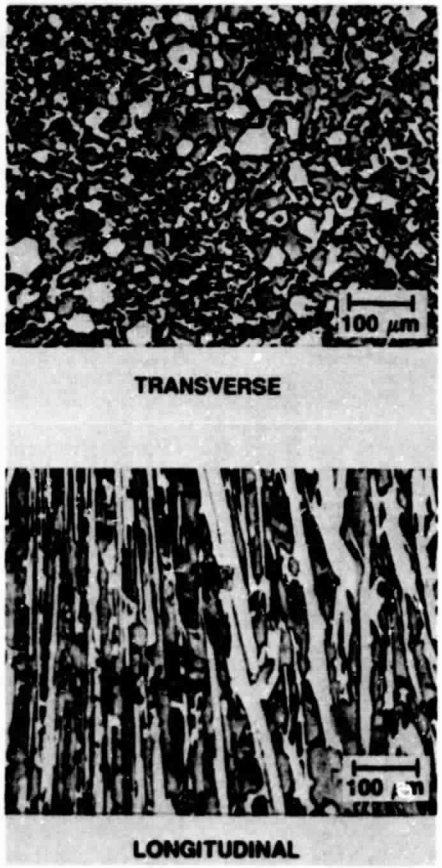

Fig. 33 As Figure 31, Alloy Cr(20)Mn(10)C(3.4)Fe(bal), 10 cmh^{-1}

carbide produced values between 1800 and 2100 VHN. The matrix has a hardness of ca 400 VHN.

H. Impact-Sliding Wear of Iron and Nickel-Based Superalloys

This part of the investigation examines the impact-sliding (8 ms^{-1}, 69 MPa) wear resistance of selected chill cast and aligned eutectic Fe-base superalloys against M42 and 17-4 PH steel counterface materials. The tests with the aligned material were run with the carbide fibers perpendicular to the counterface contact surface and the characterization focused on fracture processes as observed in the subsurface microstructure of the worn materials. Detailed metallographic analyses (taper and profile sections) were performed on specimens exposed to various numbers of repetitive impact load cycles (up to 100,000). For comparison, two other aligned in-situ composites (γ-γ'-δ and γ'-Mo) were tested with the same fiber orientation under identical test conditions against hardened M42 tool steel.

As mentioned earlier, one promising approach to achieve superalloy properties involves processing Fe-rich eutectic compositions by directional solidification in order to produce an in-situ aligned microstructure.

Earlier wear studies on aligned eutectic materials were conducted with cobalt-based alloys which were directionally reinforced by tantalum carbide fibers [73]. In that work, the TaC fibers were found to fracture when the material was exposed to repetitive impact sliding contact. At a relative transverse sliding velocity of 2.1 ms^{-1}, the more ductile α-cobalt matrix was found to plastically deform and undergo a phase transformation to β cobalt as determined by powder x-ray analysis of wear debris [73]. Related to this, Buckley found a strong increase in

the cobalt wear rate with temperature because of the allotropic transformation at 420°C [74].

With respect to iron alloys, a great deal of attention has been paid to the wear resistance of white [75,76,77,78] and grey cast irons [79-84], as these materials frequently are used as abrasion-resistant machine parts. Throughout these various investigations, the role of matrix/carbide stability, hardness, volume fraction, eutectic carbide spacing, capacity to work hardening, carbide orientation and morphology, have been examined under various contact pressures, velocities, impact conditions, and test environments. Each of these factors has been found to be significant in determining composite material wear resistance.

With cast irons, the addition of chromium has been shown to stabilize the M_7C_3 and γ-Fe phases and to improve the wear resistance [75]. The work of Thorpe et al. [85], has demonstrated that duplex eutectic carbides exist in Fe-Cr-C alloys (a core of M_7C_3 and a shell of M_3C). The structure and morphology of these carbides are two determinants of mechanical properties and wear resistance [85].

The most recent transmission electron microscope study by Pearce has shown that for 30% Cr iron, there is some strain-induced martensite which forms close to eutectic M_7C_3 carbides due to abrasive wear [86]. The increase in microhardness, as usually observed near friction surfaces, was attributed to plastic straining of the austenite and the phase transformation to martensite.

While a great many wear studies deal with steady-state conditions, some very detailed experiments by Blau [87] have pointed out the importance of the "precursor" events that establish the wear surface state during the initial stages of friction and wear tests. Accordingly, the

first part of this test program was designed to evaluate both precursor, and comparative repetitive impact-sliding wear resistance of the newly developed Fe-based eutectic superalloys in both chill cast and aligned microstructural configurations.

The second part of this study concentrates on the metallographic aspects of the worn iron-rich superalloy's microstructure. It has become apparent that scientific advancements in the area of wear of materials often depend upon interpretation of metallographic data. In fact, microstructural changes can serve to support theoretical predictions or to illuminate states of various wear processes [88-90]. It is, therefore, essential that accurate microstructural features be revealed when investigating the wear of materials. Indeed, metallographic processes such as sectioning, polishing, and etching, can introduce misleading artifacts and mask important microstructural information [91,92].

Various investigators have recognized the value of sound metallographic techniques. For example, the significance of "damage" introduced to the sample during metallographic preparation has been discussed in detail by Samuels [93], and is recognized to be an important factor in wear research [91,92,94].

The interpretation of subsurface features in worn microstructures depends upon the cross section as taken through the sample. The "normal section" (perpendicular to the wear surface) is most popular in wear studies and has been used to assess subsurface hardness profiles [95,96,97] and surface layer formation [98-101]. As a means of enhancement, taper sections have been used with some success [91,93,102], although quantitative determination obviously becomes more complex. Serial sections also have been used for crystal "reconstruction" [103]

and full characterization of near surface phenomena in the grinding of metals [104].

When microstructural inspection for wear damage is performed by transmission electron microscopy (TEM), particular care must be taken to not introduce artifacts into the samples, as any slight changes in structure are easily detected. The recent TEM work of Heilmann et al. [101], Salesky and Thomas [105], as well as that of Pearce [86] attest to the importance of wear sample preparation. Various metallographic techniques have been applied to the analysis of a newly developed iron base superalloy subjected to impact-sliding contact. In this present investigation, wear specimens were subjected to various load cycles, and metallographic examination of the subsurface was accomplished with profile, taper, and serial sections taken with respect to the relative sliding direction.

1. Materials and Methods

The materials used in this investigation were 17-4PH steel and the new superalloy Cr(20-Mn(10)-C(3.4)Fe(bal). The iron-rich superalloy used as the "pin" specimen was fashioned from directionally solidified (10 and 25 cmh^{-1}) bars. The resulting microstructure consisted of γ-Fe solid solution reinforced by the M_7C_3 (M=Fe, Cr, Mn) carbide phase. The tests were performed using two different counterface materials: a hard high-speed tool steel (M42) and a softer martensitic (17-4 PH) stainless steel (see Table 29).

The geometry of the pin and disc are shown schematically in Fig. 34. The flat-ended pin is a stepped shaft with a minor diameter of 3 mm. The disc has a diameter of 25 mm and a 2 mm thickness. The impact-sliding wear tests were performed with the apparatus developed by

TABLE 29

Material Characterization for Wear Studies

Alloy Designation	Composition (wt.%)	Conditions
Fe-base Superalloy (P)	20(Cr)-10(Mn)-3.4(C)-bal(Fe)	chill cast and directionally solidified (D.S) at 10 and 25 cmh^{-1}
γ-γ'-δ (P)	21.1(Nb)-2.5(Al)-bal(Ni)	D.S. at 8 cmh^{-1}
γ'-Mo (P)	27(Mo)-8(Al)-bal(Ni)	D.S. at 8 cmh^{-1}
M42 (D)	9.62(Mo)-7.88(Co)-3.7(Cr) 1.36(W)-1.12(V)-1.09(C)-0.4(Si) 0.24(Mn)-bal(Fe)	Hardened by quench and tempered (930 VHN)
17-4PH (D)	17(Cr)-4(Ni)-4(Cu)-1.0(Si) 0.35(Nb/Ta)-0.06(Mn)-0.05(C) bal(Fe)	Precipitation hardened (400 VHN)

(P) - pin
(D) - disc

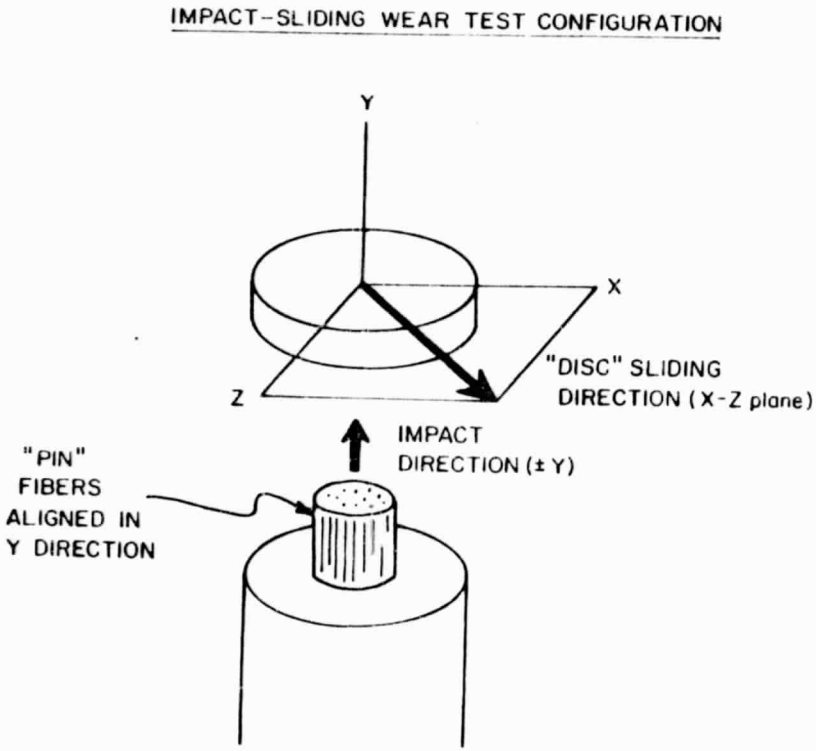

Fig. 34 Schematic of Impact-Sliding Wear Test Configuration and Pin/Disc Geometries

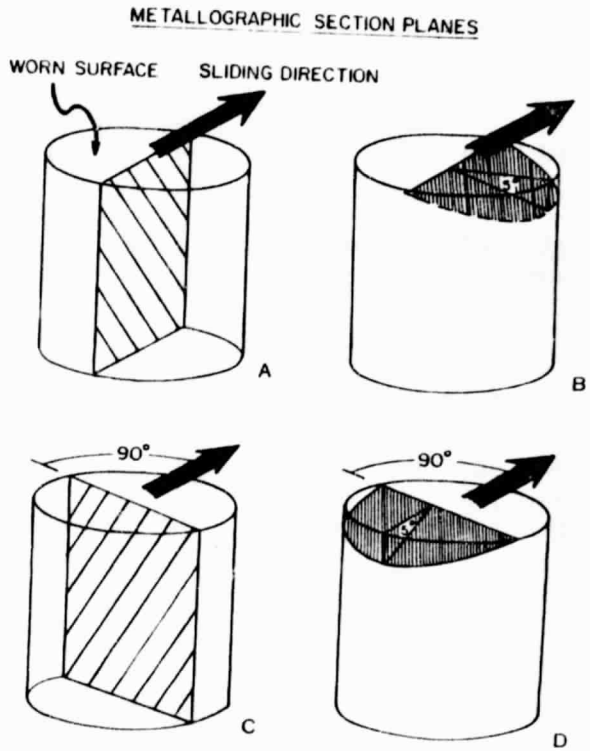

Fig. 35 Schematic of Metallographic Section Planes as Applied to the Worn Pins

Rice [106]. The relative transverse sliding velocity was 8 ms^{-1} with a nominal contact stress of 69 MPa in a laboratory air environment. The disc surfaces were ground to produce an average before-test surface roughness of 0.2 μm. The pins were abraded against 600 grit SiC paper for 1000 repetitive cycles to "run-in" the surface and establish the base line microstructural configuration. As standard procedure, the pins were examined following this run-in processing and confirmed to be free of damage. It should be noted that this procedure also ensures planar contact between pin and disc test surfaces during impact load cycling.

The wear tests were performed for 500, 1000, 10,000, and 20,000 repetitive impact-sliding cycles, thus allowing for study of the evolution of microstructural changes. Following testing, the wear pin was sectioned 3 mm below and parallel to the worn surface using a Buehler thin diamond wafering blade and an Isomet Low Speed saw lubricated with Isomet cutting fluid. The sections were then immersed in ethanol and agitated to remove the residual oil and cutting debris. The 3 mm long cylinders were then oriented to allow for either profile or taper sectioning through the worn surface. Figure 35 illustrates the four metallographic section planes as referred to the sliding direction and pin axis. The mounting procedure for the profile sections (Fig. 35 Types A and C) simply utilized a cement (cyanoacrylate) to attach the unworn cylinder onto a nut which served as a jig. The pin alignment was accomplished optically to achieve the normality conditions shown in Fig. 35, Types A and C. The taper sections shown in Fig. 35, Types B and D, were taken at 5° from the wear surface. This was accomplished by first preparing a rectangular (9 mm x 13 mm x 13 mm) steel fixture which

contained a "channel" carefully ground to a 5° orientation with a 3 mm depth. The worn samples were then oriented in this channel to achieve the conditions in Figure 35, Types B and D. The various arrangements were then independently mounted by hot pressing (2,500 psi, 150°C, 15 min.) with Epomet molding compound. The molded samples were then ground with water lubricated 120 grit SiC until one-half of the wear pin diameter was measured. In the case of the taper sections, grinding was continued until the jig (but not the wear pin) was visible. Subsequent polishing steps were 240, 400 and 600 grit SiC at low speed in water. Normal sections were rotated 90° between steps while taper sections were turned only slightly such that the wear surface was maintained as the "leading edge." This was done to maintain the worn surface region in compression so as to minimize unwanted cracking as reported by Torrance [91]. Rough polishing was accomplished on a concentric grooved lead lap wheel (100 rpm) charged with 15 μm diamond paste; the lubricant was a solution of kerosene and oil. Following ultrasonic cleaning in ethanol, an identical lead lap with 6 mm diamond was used to achieve a mirrorlike appearance. Final polishing was done with 0.05 μm chromium oxide on synthetic velvet which covered a plexiglass wheel; distilled water was the lubricant. Chemical etching was not used with light microscopy; however, Fry's reagent was employed for the scanning electron microscopy work.

2. Wear Against 17-4 PH Steel

Weight change measurements were made on superalloy pins and 17-4 PH steel discs at 5,000, 10,000, 15,000, and 20,000 repetitive load cycles. Severe wear of the 17-4 PH steel by each pin was observed and testing stopped after 20,000 cycles. Each pin experienced some degree of weight

gain, attributed to material transport of the 17-4 PH steel onto the pin.

3. Wear Against a Hard Counterface

The comparative wear resistance of the iron and nickel-based superalloys is shown in Fig. 36 as weight loss vs. repetitive impact-sliding cycles. The γ'-Mo and γ-γ'-δ alloy experienced "mild" weight loss following 100,000 cyles with little or no wear of the M42 disc. The iron-base alloy in the chill cast condition, however, did wear considerably following 20,000 cycles with no detectable wear of the M42 counterface. Surprisingly, the same iron-base alloy in the directionally solidified condition is observed to wear the M42 material dramatically without incurring any weight loss itself. This is strong evidence for the influence of microstructural configuration on the wear resistance of alloys.

4. Inspection of the Subsurface Microstructure

The interpretation of subsurface microstructural changes which result from wear processes can be described through the use of the subsurface zone model shown in Fig. 37. This representation consists of Zone 1 as undisturbed base material. Zone 2, the intermediate region, is plastically deformed, and Zone 3 is an interfacial layer which can be a mixture of pin and disc materials and the test environment.

Figures 38A, 38B, and 38C show profile sections (see Fig. 35) taken through γ'-Mo, γ- γ'-δ and the Fe-base superalloy respectively. After 100,000 cycles, the micrographs of the nickel-base alloys in Figs. 38A and 38B show the reorientation of the aligned phase (Zone 2) and some indication of a chemically distinct (Zone 3) surface layer. The Fe-alloy (D.S. 25) contains cracks which are oriented in the direction of

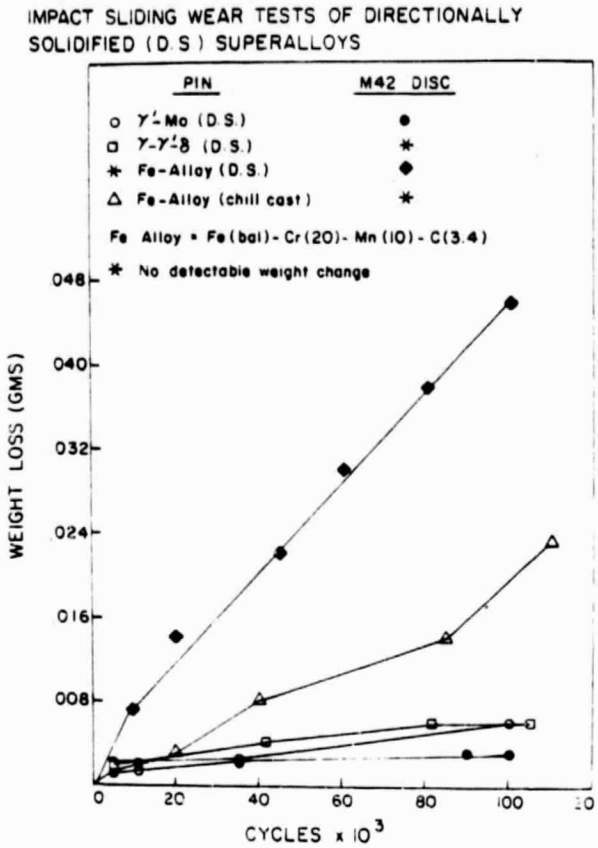

Fig. 36 Weight Loss vs. Cycles for Nickel- and Iron-Base Superalloys

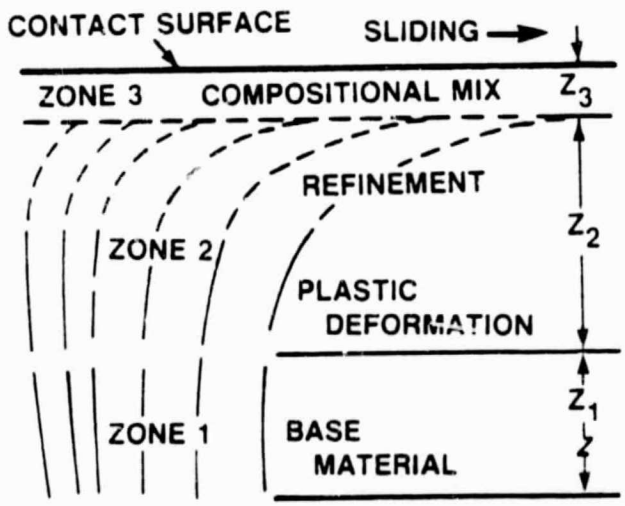

Fig. 37 Subsurface Zone Schematic Representation

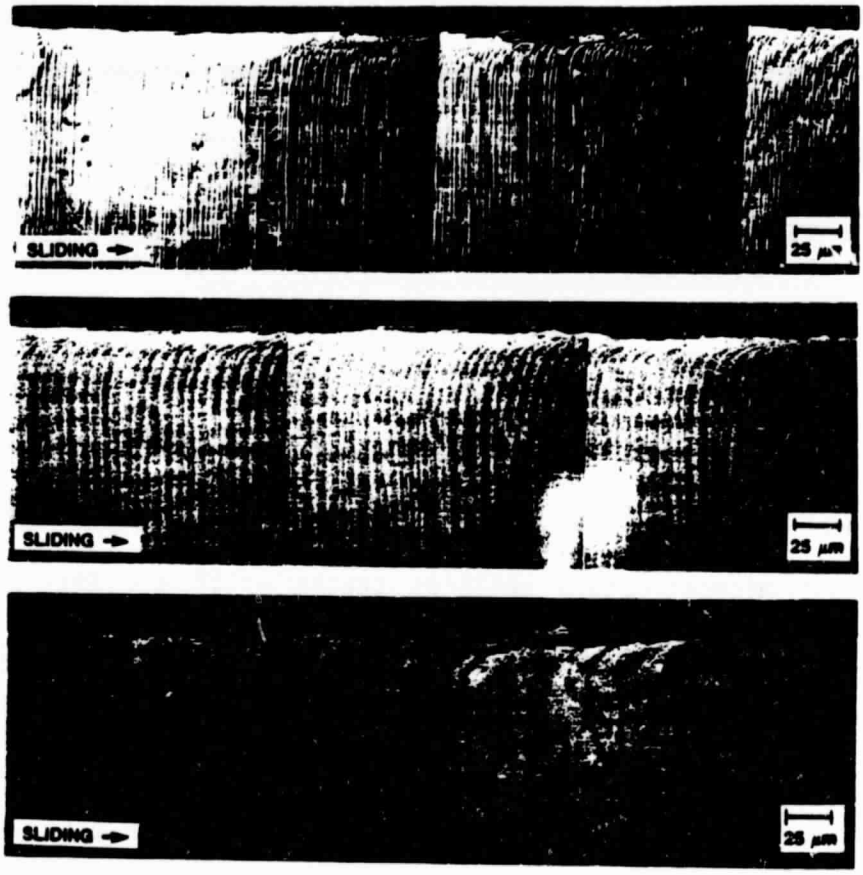

Fig. 38A Light Micrograph, Profile Section of γ'-Mo, 100,000 Cycles, M42 Counterface; Fig. 38B, as Fig. 38A, γ-γ'-δ; Fig. 38C, as Fig. 38A, Fe-Base Superalloy D.S. 25cmh^{-1}

the aligned phases (Fig. 38C). The Zone 3 surface layer is more pronounced on the Fe alloy. Inspection at higher magnification reveals more detail in the near surface region (see Figs. 39A-39D). In Fig. 39A the γ'-Mo aligned structure is reoriented by nearly 90° beneath the wear surface, and apparent mixing of the M42 and γ'-Mo materials occurs within Zone 3. The nickel base alloy γ-γ'-δ (Fig. 39B) reveals many cracks appearing in Zone 3. Interestingly, a propagated crack path develops into Zone 2, following the matrix/fiber interface and terminates by penetrating the aligned γ'- phase. In comparison, the Fe-base superalloy is seen in Figures 39C and 39D for the D.S. 25 cmh^{-1} and chill cast conditions following 100,000 cycles. In this, the highly wear resistant D.S. material (Fig. 39C) contains subsurface cracks which follow the aligned carbide phase along intergranular and transgranular paths. The Zone 3 layer appears securely bonded and tends to "fill" the near surface crack opening. In contrast to this behavior, the chill cast microstructure contains cracks which are nearly parallel to the wear surface and which do not penetrate into the substrate. The Zone 3 layer is not apparent for the chill cast material.

The profile sections of Figures 38 and 39 give a planar view of the worn subsurface, while taper sections can provide insight into three-dimensional crack paths. Figures 40A-40D are taper sections (see Fig. 35B and 35D) through the iron base superalloy following testing against 17-4 PH steel. Figures 40A and 40B show the 10 cmh^{-1} and 25 cmh^{-1} D.S. pins following after 500 cycles. A crack network exists in Zone 2, with propagation into the apparently homogeneous Zone 3 layer. The chill cast material (Fig. 40C) contains fewer cracks following 500 cycles, but after 20,000 cycles (Fig. 40D) a coarse crack network develops. In

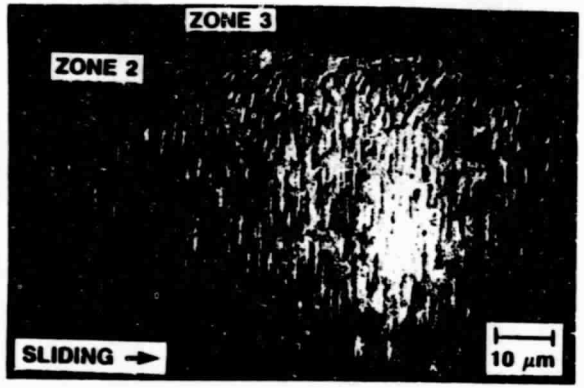

Fig. 39A High Magnification of Near Surface Microstructure, as Fig. 38A

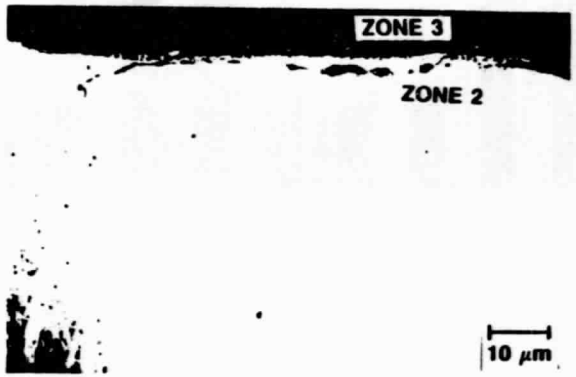

Fig. 39B High Magnification of Nickel-Based Superalloy, as Fig. 38B

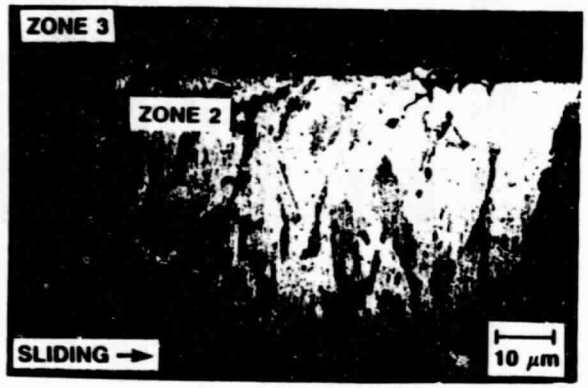

Fig. 39C High Magnification of Fe-Based Superalloy D.S. 25cmh^{-1}

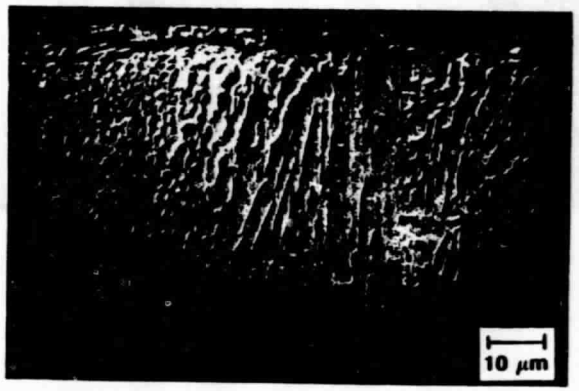

Fig. 39D As Fig. 39C, Chill Cast Microstructure

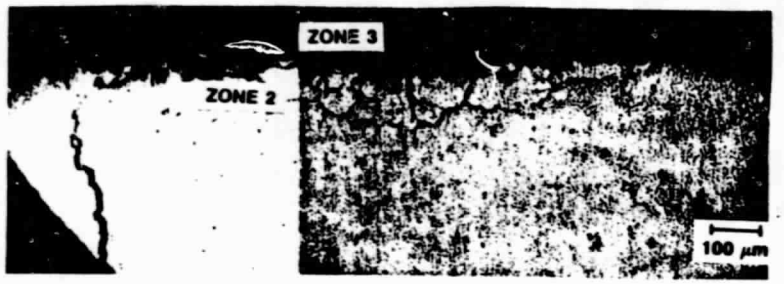

Fig. 40A Light Micrograph of Fe Base Superalloy D.S. at 10 cmh^{-1}

Fig. 40B As Fig. 40A, 25 cmh^{-1}

Fig. 40C As Fig. 40A, Chill Cast, 500 Cycles

Fig. 40D As Fig. 40C, 20,000 Cycles

this, penetration is deep into the subsurface material, as found in the directionally solidified specimens.

5. Subsurface Damage

In the light of the various microstructural changes encountered in this investigation, the importance of material transport becomes a key issue. For the case when no disc wear was produced, the Fe-base alloy (chill cast) did not form a thick, adhered Zone 3, but did suffer from subsurface cracking (see Figs. 39D, 40C and 40D) leading to severe weight (volume) loss. In contrast, the same Fe-base alloy in the directionally solidified configuration formed a strong interface Zone 3 region (see Figs. 38C and 39C). The D.S wear pin of Fig. 38C did contain periodically spaced cracks that are no doubt related to the aligned structure. However, these cracks propagate along the carbide or carbide/matrix interface and terminate in the substrate (the Zone 2/Zone 1 interface). Based on such a comparison, it appears that the Zone 3 layer serves to transmit interfacial shear stresses and/or to "flow."

Detailed Metallography of Iron Rich Superalloy Wear Prior to Steady State

Based upon the microstructures obtained thus far, a more detailed examination seemed necessary to understand the early stages of the wear process.

The conventional profile section (see Fig. 35A) of a worn pin after 1000 cycles is shown in Fig. 41A and reveals the aligned duplex microstructure of the superalloy. From this point of view, subsurface cracks are observable and favor the matrix/carbide interface, within the Zone 2 region. Increasing the cycle to 10,000 produces a similar Zone 2 region; however, the development of a Zone 3 layer is apparent in Fig.

41B. This Zone 3 is bonded to Zone 2 and is seen to contain a continuous crack which could obviously lead to debris formation. For comparison, Figuress 41C and 41D represent the section plane of Fig. 35C taken at 1,000 and 10,000 cycles, respectively. Figure 41C clearly reveals the refinement of the carbide phase; however, the cracks of Figure 41A are not present but a thin Zone 3 is detectable. Figure 41D reveals the unexpected crack path as viewed parallel to the sliding direction. The surface roughness profile is obtained in Fig. 41D and subsurface cracks are continuous between Zones 2 and 3. Crack branching is found in Zone 2 and evidence for mixing is seen in Zone 3.

From observations of the profile sections, the appearance of the subsurface zones is markedly different and each view (Fig. 41A to 41D) offers a unique perspective to the worn microstructure.

Turning to the taper section (see Fig. 35, Type D), still another view is obtained which exposes the subsurface crack network. Figures 42A and 42B are taper sections following 20,000 load cycles on the 10 cmh^{-1} and 25 cmh^{-1} solidified materials. Fig. 42A contains a finer network of cracks, primarily confined to Zone 2. At the higher solidification rate, the crack network does not penetrate as deeply into Zone 2 and continuous crack paths tend to favor the Zone 2/Zone 3 interface with less branching. Although the volume fraction of carbides is the same for Figs. 42A and 42B, the carbide spacing differs, and obviously influences the subsurface fracture processes.

The final taper section (see Fig. 35, Type B) was performed on a 25 cmh^{-1} directionally solidified specimen following 10,000 cycles. This section focused on the crack orientation and spacing and Fig. 43A provides insight into the behavior of cracks at the Zone 2/Zone 3

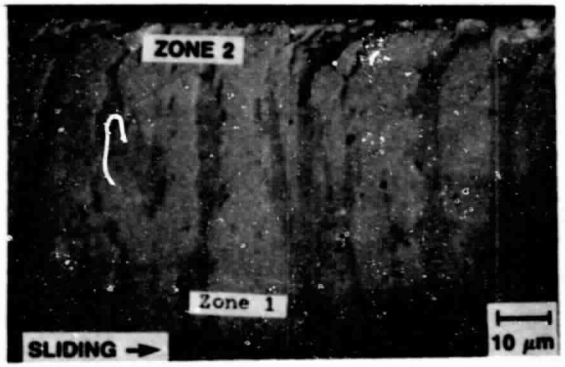

Fig. 41A Light Micrograph, Profile Section as Shown in Fig. 35A, N = 1,000 Cycles, D.S. at 10 cmh^{-1}

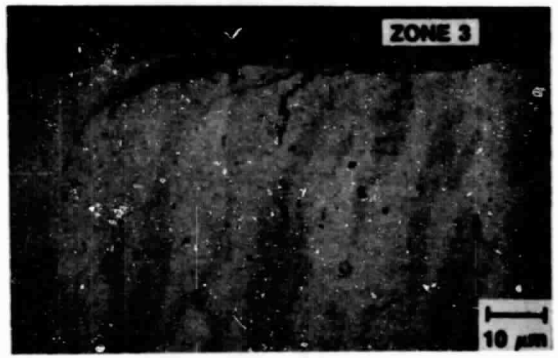

Type 'A'

Fig. 41B As Fig. 41A, N = 10,000 Cycles

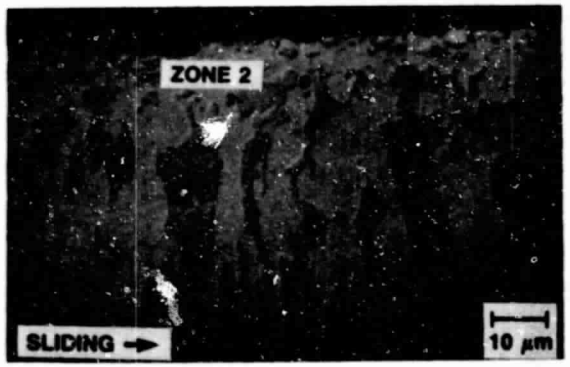

Fig. 41C Light Micrograph, Profile Section as Shown in Fig. 35C, N = 1,000 Cycles, D.S. at 10 cmh^{-1}

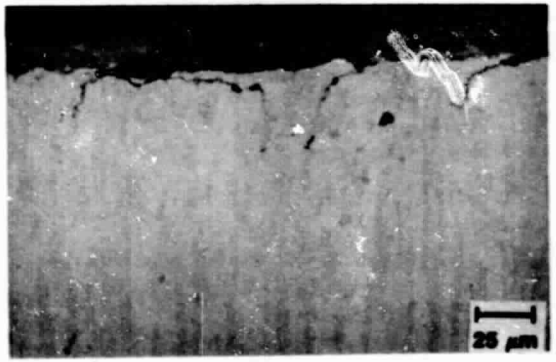

Type 'C'

Fig. 41D As Fig. 41C, N = 10,000 Cycles

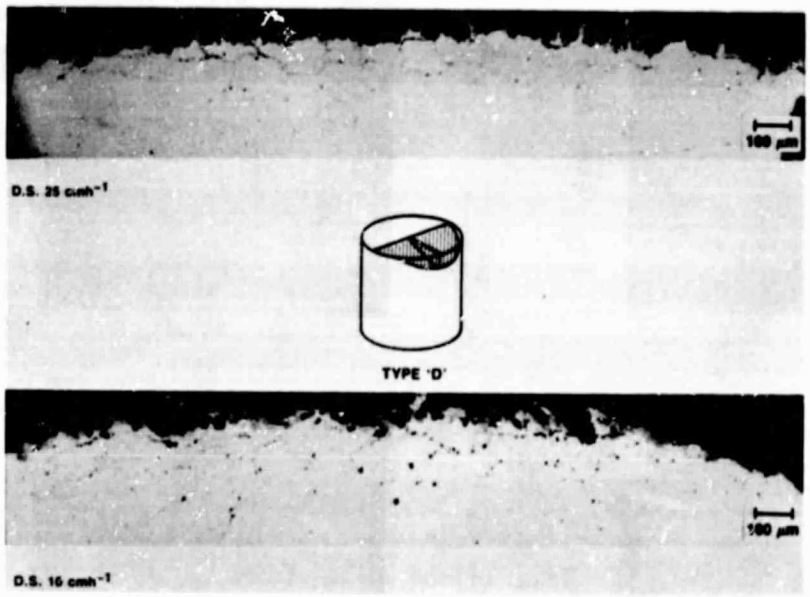

Fig. 42A Light Micrograph, Taper Section as Shown in Fig. 35D, N = 20,000 Cycles, D.S. at 10 cmh^{-1}

Fig. 42B As Fig. 42A, D.S. at 25 cmh^{-1}

Fig. 43A Light Micrograph, Taper Section as Shown in Fig. 35B, N = 10,000 Cycles, D.S. at 25 cmh^{-1}

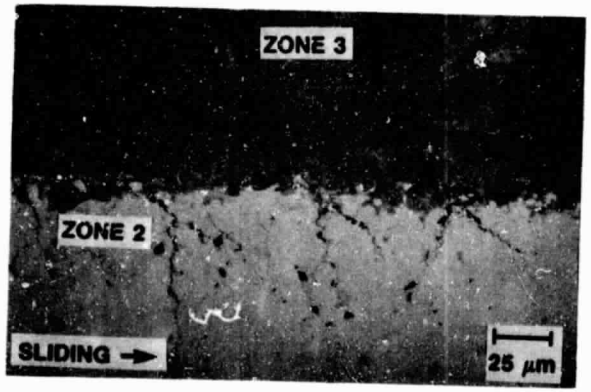

Fig. 43B As Fig. 43A, Close-Up of Securely Bonded Zone 2/Zone 3 Interface

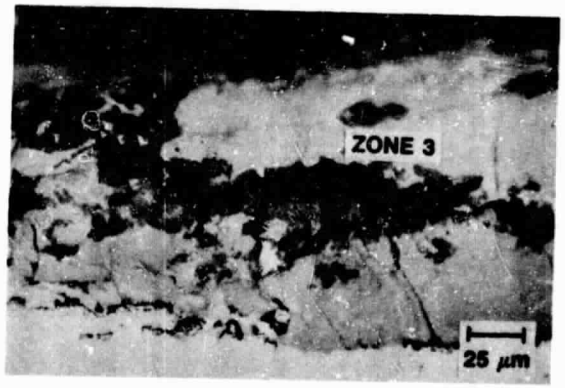

Fig. 43C As Fig. 43B, Weakly Bonded Interface

interface. The cracks in Zone 3 are regularly spaced and oriented normal to the sliding direction. A close inspection of the right side of the section (Fig. 43B) shows a region where Zone 2 and Zone 3 are securely bonded and cracks are found to branch into Zone 2 and continue through Zone 3. In contrast, Fig. 43C is a region where Zone 2 and Zone 3 appear less strongly bonded. The result is suggestive of a mechanical mixing within Zone 3, and the cracks do not penetrate as deeply into Zone 2. The difference between Fig. 43B and 43C probably stems from different load cycling experienced by the leading and trailing ends of the specimen.

Table 30 illustrates an increase in the Zone 2 hardness with increasing number of load cycles. Table 30 further shows the Zone 3 development leading to a "steady state" thickness for this layer. Interestingly, Zone 3 has an intermediate hardness of 1,060 V.H.N. which lies between Zone 1 (400 V.H.N.) and the bulk carbide hardness (1,900 V.H.N.). The average spacing between cracks decreased slightly with increasing cycles, while the thickness of Zone 2 was observed to remain nearly constant throughout the tests. This suggests that cracks initiate early and penetrate to a terminal depth from the surface. Further growth is in the form of lateral branching with increasing numbers of impact cycles. This branching has been added to the primary crack length to give the average crack length data in Table 30.

The scanning electron micrograph in Fig. 44A presents a worn pin which contains the actual wear surface with associated light micrographs of the profile (Fig. 44B) and taper sections (Fig. 44C). From such data, the advantage of combined metallographic sections is apparent.

TABLE 30

Quantitative Analysis Determined by Serial Sections*

Cycles	Microhardness (V.H.N.)**		Layer Thickness (μm)	Subsurface Crack Parameters***	
	Zone 2	Zone 3	Zone 3	Avg. Spacing (μm)	Avg. Crack Length (μm)
1,000	670	-	12	60 ± 25	12 ± 3
10,000	820	1060	25	50 ± 25	18 ± 3
20,000	870	1060	25	40 ± 25	28 ± 3

* 4 sections per test sample, Fig. 35, Type A profile sections

** matrix hardness for Zone 2

*** Quantimet image analysis data

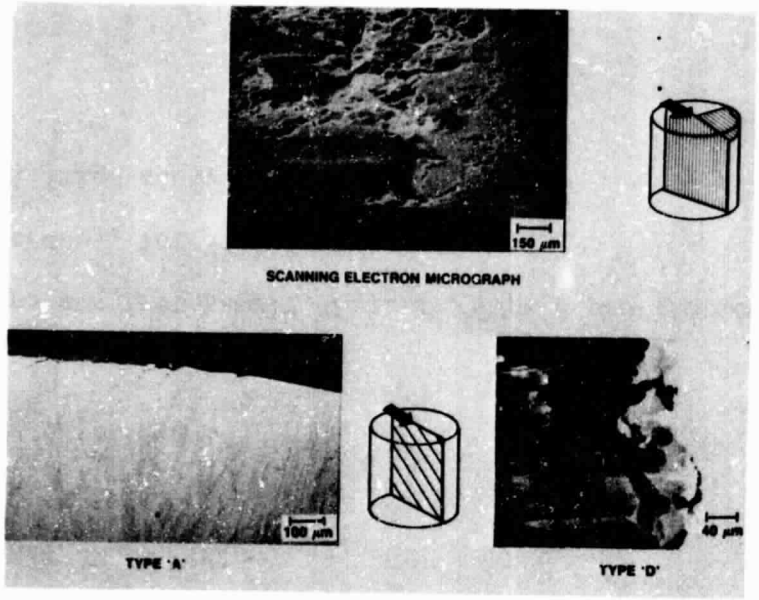

Fig. 44A Scanning Electron Micrograph (S.E.M.), Wear Pin Segment Showing Wear Surface, Profile and Taper Section Planes

Fig. 44B Light Micrograph, Profile Section of Fig. 44A

Fig. 44C As Fig. 44B, Taper Section

IV. Discussion

The development of iron-rich low-cost superalloys has been pursued from two different approaches, which differ in their chemistry and processing. The first approach was to process all alloy compositions by chill casting, as this is the conventional means by which automotive engine components would be produced. The initial alloys (NASAUT 1 to NASAUT 12) screened the influence of major chemical changes to the basic Fe-Cr-Mn-C system. Keeping in mind that the microstructure of γ-Fe matrix with M_7C_3 carbide was desired, the alloying elements Mo and Al were added in varying proportions. The resulting phase equilibria (see Tables 1 and 2) revealed that the M_7C_3 carbide was not coexisting solely with the γ matrix, but was rather a mixture with the $M_{23}C_6$ or M_2C carbides. The presence of the M_2C is explained by the previous work of Gupta [43] who found that Mo favored the M_2C over the M_7C_3. The higher amounts of chromium, thought initially to stabilize the M_7C_3 carbide are seen to also form $M_{23}C_6$ at higher concentrations. This observation was also made by Lemkey et al. [3] (see Fig. 7) in the Fe-Mn-Cr-C system. The initial screening of the alloy candidates was done by mechanical property measurements and cyclic oxidation tests. Based on these tests, the influence of alloy chemistry produced a range of ductile, strong, and oxidation resistant materials. Two specific compositions, NASAUT 1 and NASAUT 4, were identified as having the most promising combination of properties and suitability for further modification. The chemical modifications were made later on with Mo, Al, Si, Nb, and carbon additions. It became clear that NASAUT 4G Mn(15)-Cr(12)-Mo(3)-C(1.5)-Si(1.0)-Nb(1.0)-bal Fe was the best alloy for oxidation resistance and appeared to be stronger at higher stress levels [107]. Good creep

ductility was also obtained with temperatures up to 870°C. At this point, ground tensile samples were exposed to flowing hydrogen for 100 hours at 788°C and tested at 24° and 788°C showing a small loss in strength and ductility. Modifications were then made on NASAUT 4GA by adjusting the Cr, Mo, and Nb concentrations, producing alloy 4GA1, Mn(15)-Cr(15)-Mo(2)-C(1.5)-Si(1.0)-Nb(1.0)-bal Fe, which optimized the desired properties. Reactive metal additions were made to the 4GA alloys with La, Ce, Hf, and Y to improve the oxide stability and adherence [108]. After cyclic oxidation testing, the oxide which developed on the test bars was identified as a mixture of cubic β-Mn_2O_3 (a = 9.424 Å), spinel and α-Fe_2O_3. With the exception of the Y additions by themselves, excellent cyclic oxidation resistance was obtained. At this stage of development NASAUT 4GA1 emerged as the alloy for more advanced performance evaluation, thus high cycle fatigue tests were done (R ratio $\sigma_{min}/\sigma_{max}$ of 0.1 at 20 Hz) with the endurance limit set at 10^7 cycles. This endurance limit was found to be 241 MPa for NASAUT 4G-A1 which is superior to the comparable alloys X-40 and equivalent to XF-818 [109]. The identification of alloy NASAUT 4GA1 was, in essence, the major finding of the cast iron alloy development task.

Another aspect of this work was the clear understanding of the carbide phase molybdenum cementite "$MoFe_2C$." This carbide phase could easily exist within the various alloy modifications and contribute to the properties. As mentioned earlier, very little attention has been paid to this important phase and there is a lack of references and research data in the field of Cr-Mo steels. The recent work of Craig [62] has pointed to this fact and his investigations have shown that "$MoFe_2C$" is responsible for the strengthening of 4140 steels. Interestingly,

Craig has stated that the Mo-cementite does not form out of a reaction sequence with Fe_3C as previously proposed by Dyson and Andrews [63]. In fact, Craig showed evidence for the formation of "$MoFe_2C$" in the presence of NbC, which may act as a nucleus. This observation is pertinent to this investigation, as NASAUT 4GAl contains the necessary elements to develop the Mo-cementite precipitates. It is not known whether this carbide phase is beneficial or deleterious to the alloy behavior in general and its kinetics of formation is not known. It then became apparent that the "$MoFe_2C$" phase deserved further investigation. The earliest work by Kuo and Dyson and Andrews identified the carbide phase from a polycrystal isolated by chemical extraction. Based on powder patterns, Dyson and Andrews proposed an orthorhombic crystal structure for Mo-cementite with a relatively large cell size. Indexing of electron diffraction patterns [63] did not really confirm this crystal structure, posing the technical challenge of accurate crystal structure determination.

The approach taken in this investigation was to grow single crystals of the Mo-cementite and solve the structure by conventional X-ray crystallography techniques. This resulted in the new monoclinic cell description which is roughly one fourth the volume of the previously proposed orthorhombic cell. The new crystal structure is seen to be made up of trigonal prisms and octahedral structural elements configured with the metal atoms. The carbon atoms occupy the voids in metal octahedra and metal trigonal prisms. The accurate chemical formula for the molybdenum cementite derived from the crystal structure determination is $Mo_{12}Fe_{22}C_{10}$. There remained some question of Mo and Fe atom occupancy which could lead to partial mixing between atomic sites. This was

checked by varying the isotropic and anisotropic temperature factors for each atom which proved that within the standard deviation, no metal atom mixing was probable. It should be mentioned that the obtained R-value of 6% is most satisfactory.

The second approach in this program was to study the effects of processing on the properties of the Fe-Cr-Mn-C base alloy. This work, as contrasted to the cast alloy modifications for the Stirling engine, was aimed at gas turbine applications. To achieve the necessary high temperature superalloy properties, processing of the eutectic composition Fe-(20)-Cr-(10)Mn-(3.4)C was done by directional solidification. This resulted in a structure with M_7C_3 carbide fibers aligned in a γ-Fe solid solution matrix. At the onset, it was obvious that this unique processing would provide the strength [3] currently obtained with nickel base superalloys although little was known about the structural interplay between the M_7C_3 and γ-$Fe_{s.s.}$ phases. In this work, the D.S. alloys were further evaluated for thermal expansion, fiber orientation, by means of X-ray and electron diffraction, and wear resistance. By extracting the M_7C_3 carbide phase, the thermal expansion behavior was shown to be strongly anisotropic with the a-axis changing significantly from room temperature to 800°C. In contrast, the c-axis change was barely detectable. This has significance with regard to the alloy stability at elevated temperature because the D.S. processing produces an epitaxial relationship between the aligned M_7C_3 and γ-Fe matrix. Since there is an inherent difference between the thermal expansion coefficients of the cubic matrix and the hexagonal carbide, interfacial stress will exist. The measurements made in this work show that significant lattice mismatch will be preferentially produced along the

fiber/matrix interface at elevated temperatures. Transmission electron microscopy of transverse sections of Fe-(20)Cr-(10)Mn-(3.4)C processed at 5 cmh^{-1} revealed the c-axis of the carbide aligned parallel with [112] the matrix. X-ray diffraction of extracted carbide whiskers also showed strong texturing of the M_7C_3 with c-axis alignment in the growth direction. It is believed that due to Lattice mismatch and thermal expansion behavior, the D.S. composites will produce hoop stresses which may influence the mechanical properties, especially thermal fatigue resistance at elevated temperatures.

Since the solidification behavior of the Fe-Cr-Mn-C alloy displayed strong coupled growth, compositional changes were examined as well as various growth rates to regulate carbide distribution, spacing and stability. Chemical additions of Al, Mo, and Si proved to complicate the directional solidification growth mechanism of the alloy leading to undesirable dendritic microstructures. The M_7C_3 carbide stability was a point of concern, as the earlier eutectic alloy research of Boomgaard [18], showed a deleterious phase transformation of Cr_7C_3 to $M_{23}C_6$ at elevated temperatures. However, this current investigation has proven the $(Fe,Cr,Mn)_7C_3$ to be a very stable phase after two weeks at 1150°C and four weeks at 950°C. Changes in the directionally solidified carbide morphology were more apparent at the higher temperature, which is attributed to coarsening.

Another property of considerable interest is the wear resistance of the directionally solidified alloy. Earlier research with cobalt/tantalum carbide (COTAC) eutectics showed a very high resistance to impact-sliding wear when the fibers were aligned perpendicular to the sliding direction [72].

The supposition in this current work was that the wear resistance of the directionally solidified microstructure would be superior to that produced by conventional chill casting. Furthermore, since the rupture strength of the D.S. Fe-(20)Cr-(10)Mn-(3.4)C was equivalent to nickel base alloys, its impact wear behavior would also compare favorably.

The structure and morphology of the carbide phases in the cast iron alloys are controlled by processing and ultimately determine the mechanical properties and wear resistance. When the Cr(20)-Mn(10)-C(3.4)-bal Fe alloy was tested by impact wear against 17-4 PH steel, almost no wear of the superalloy was observed. The softer 17-4 PH steel was severely worn and adhesively transferred onto the superalloy pin which actually gained weight during the wear test. This behavior was true for both chill cast and directionally solidified microstructures.

When a hard M42 tool steel was used in place of 17-4 PH steel, then the effect or processing became apparent. The iron base superalloy suffered considerable wear in the chill cast condition without wearing the M42 counterface. Directionally solidified material surprisingly wore the M42 a great deal without incurring any weight (volume) loss itself. The influence of the microstructure is apparent and the role of the aligned carbide phase is to greatly improve the alloy's wear resistance. Since the volume fraction of carbide phase is a constant between the chill cast and D.S. materials, the columnar fibrous carbide serves to "machine" the counterface and resist deformation. Figure 36 shows that the impact wear resistance of nickel based D.S. alloys compares favorably with the iron base alloy. Subsurface microstructural inspection of these D.S. alloys after wear revealed a reorientation (bending) of the aligned phases into the sliding direction, with some cracks.

These cracks were usually found in Zone 3, a deposited surface layer which was chemically distinct from the substrate. This interface layer results from mechanical mixing of the pin and disc materials over a 100 μm distance. Depending on the reactivity of the worn surfaces with the air atmosphere, oxides of the metal components may also be present. The crack paths in the iron base alloy appeared to follow the carbide/matrix interface with some transgranular fracture. The adhered layer (Zone 3) on the superalloy was frequently seen to fill the crack openings, thus the plastic flow of this material obviously is very high. Taper sections through the worn surfaces showed that beneath the adhered layer was a three-dimensional crack network which was linked to the homogeneous Zone 3. The chill cast materials had a coarser network than did the directionally solidified microstructures. There is no doubt that the different carbide configurations allow various crack networks to develop, in the case of D.S. material. Based on the microstructural evidence in Figures 38A-38C and 40A-40D, it appears that the Zone 3 layer serves to transmit interfacial shear stresses to the substrate. Depending on the degree of bonding between Zones 2 and 3, more near surface damage can exist in Zone 3 (weak bond situation) and thus debris stems from the region. When a strong bond is produced, Zone 3 transmits higher stresses to Zone 2 as demonstrated by the consequent subsurface deformation (Figs. 38A, 38B, 38C) and attendant fracture processes (Figs. 40A-40D).

The influence of the solidification rate on wear resistance for the iron base superalloy was examined for 10 cmh^{-1} and 25 cmh^{-1} materials. At the higher processing rate. worn materials contained subsurface crack networks which did not penetrate deeply into the substrate because

continuous cracks tended to favor the Zone 3/Zone 2 interface. The spacing of the carbide fibers is thought to be the reason for differences in the crack networks.

The effect of load cycles is seen in Table 30 which details subsurface zone thickness and hardness. After 1,000, 10,000, and 20,000 load cycles, Zone 3 on the iron base superalloy develops to a steady state configuration. By 10,000 cycles, Zone 3 is 25 μm thick and has a hardness of 1060 V.H.N. which is maintained up to 20,000 cycles. Interestingly, the cracks which form in the subsurface of these worn samples grow in length with increasing cycles. Intuitively, the crack spacing is expected to decrease as cycles increase and the population of cracks seems to go up; however, the scatter in this measurement does not allow for this confirmation in Table 30.

This work has shown that multiple metallographic techniques are needed to accurately describe the subsurface microstructural changes induced by impact-sliding wear. With increasing load cycles, cracks grew to a terminal depth and continued growth by lateral branching, with a decrease in average crack spacing. A combination of profile and taper sections has proven to be useful in determining subsurface crack behavior in an iron base superalloy. Furthermore, this portion of work has shown that material transport between mating material pairs is an influential factor which regulates the subsurface crack behavior.

V. Conclusions

1. A low-cost iron base superalloy has been identified as NASAUT 4GA1 Cr(15)-Mn(15)-Mo(2)-C(1.5)-Si(1.0)-Nb(1.0)-Fe(bal). This alloy when processed by conventional chill casting has physical and mechanical properties at elevated temperatures which compare favorably with existing nickel base superalloys while containing significantly lower amounts of strategic elements.

2. Studies on the molybdenum cementite phase have proven that the crystal structure of the ξ phase is not orthorhombic. The molybdenum cementite has a monoclinic cell (space group C2/m) a=10.870, b=7.761, c=6.563 Å and β=120.1° with a volume approximately one fourth the size of the previously proposed cell. The crystal structure of the Mo-cementite (ξ phase) is made up of octahedra building elements consisting of 4 Mo and 2 Fe-atoms and trigonal prisms consisting of 4 Fe and 2 Mo-atoms. The voids are occupied by carbon atoms.

3. The previous chemical formula for the molybdenum cementite "$MoFe_2C$" is now clearly seen to be $Mo_{12}Fe_{22}C_{10}$.

4. The thermal expansion of the M_7C_3 (M=Fe,Cr,Mn) carbide is highly anisotropic with the a-axis being the predominant mode of expansion.

5. Directional solidification of the Cr(20)-Mn(10)-C(3.4)-bal (Fe) eutectic produces an aligned microstructure consisting of M_7C_3 fibers in a γ-Fe matrix. This good alignment vanishes when molybdenum or aluminum is added in higher concentrations.

6. The directional solidification provides impact wear resistance exceeding that of conventional nickel base superalloys when tested against M42 steel.

7. An interesting finding from this work is the strong improvement in wear resistance of an aligned eutectic structure as compared to the corresponding randomized chill cast structure. Impact wear experiments with the softer 17-4 PH steel counterface were characterized by transfer onto the Fe-base superalloy. The cracks which form in this transported layer and in the superalloy materials were oriented transverse to the relative sliding direction. Moreover, the cracks occur in a periodic fashion, reflecting their relationship to the underlying microstructure.

Appendix 1

Bond Length and Bond Angles for the ξ Carbide

Carbon (1)

C(1)-Fe(2)		1.980(12)
C(1)-Fe(4)		1.982(10)
C(1)-Fe(3)		2.017(11)
C(1)-Fe(3)		2.144(11)
C(1)-Mo(1)		2.144(12)
C(1)-Mo(2)		2.165(11)
C(1)-Mo(2)		2.337(11)
C(1)-Fe(5)		2.715(11)
C(1)-Fe(5)		2.878(11)

Fe(2)-C(1)-Fe(4)		82.3(4)	2.606( )
Fe(2)-C(1)-Fe(3)		123.1(6)	3.514( )
Fe(2)-C(1)-Fe(3)		73.3(4)	2.465( )
Fe(2)-C(1)-Mo(1)		151.2(6)	3.994( )
Fe(2)-C(1)-Mo(2)		85.8(4)	2.824( )
Fe(4)-C(1)-Fe(3)		75.9(4)	2.458( )
Fe(4)-C(1)-Fe(3)		119.6(5)	3.566( )
Fe(4)-C(1)-Mo(1)		90.0(4)	2.920( )
Fe(4)-C(1)-Mo(2)		152.3(6)	4.026( )
Fe(3)-C(1)-Fe(3)		73.5(4)	2.491( )
Fe(3)-C(1)-Mo(1)		81.1(4)	2.708( )
Fe(3)-C(1)-Mo(2)		131.1(6)	3.807( )
Fe(3)-C(1)-Mo(1)		133.3(6)	3.937( )
Fe(3)-C(1)-Mo(2)		80.2(4)	2.774( )
Mo(1)-C(1)-Mo(2)		88.4(4)	3.005( )

Carbon (2)

C(2)-Fe(5)	2x	1.923(3)
C(2)-Mo(2)	4x	2.067(1)

Fe(5)-C(2)-Mo(2)	4x	87.88(6)	2.770( )
Fe(5)-C(2)-Mo(2)	4x	92.12(6)	2.875( )
Mo(2)-C(2)-Mo(2)	2x	94.83(6)	3.044( )
Mo(2)-C(2)-Mo(2)	2x	85.17(6)	2.797( )
Fe(5)-C(2)-Fe(5)		180.0	3.845( )
Mo(2)-C(2)-Mo(2)	2x	180.0	4.134( )

Appendix 1 (continued)

Bond Length and Bond Angles for the ξ Carbide

Iron (1)					
Fe(1)-Fe(3)	4x	2.481(2)			
Fe(1)-Fe(2)	2x	2.498(3)			
Fe(3)-Fe(1)-Fe(3)			2x	61.25(8)	2.528( )
Fe(3)-Fe(1)-Fe(3)			2x	118.75(8)	4.270( )
Fe(3)-Fe(1)-Fe(2)			4x	120.66(6)	4.326( )
Fe(3)-Fe(1)-Fe(2)			4x	59.34(6)	2.[illegible]( )
Fe(3)-Fe(1)-Fe(3)			2x	180.0	4.962( )
Fe(2)-Fe(1)-Fe(2)				180.0	4.996( )
Iron (2)					
Fe(2)-C(1)	2x	1.980(12)			
C(1)-Fe(2)-C(1)				149.0(6)	3.815( )
Iron (3)					
Fe(3)-C(1)		2.017(11)			
Fe(3)-C(1)		2.144(11)			
C(1)-Fe(3)-C(1)				106.5(4)	3.335( )
Iron (4)					
Fe(4)-C(1)		1.982(11)			
Fe(4)-C(1)		1.982(11)			
C(1)-Fe(4)-C(1)				141.0(7)	3.736( )
Iron (5)					
Fe(5)-C(2)		1.923(3)			
Molybdenum (1)					
Mo(1)-C(1)	2x	2.144(11)			
C(1)-Mo(1)-C(1)				128.1(6)	3.855( )
Molybdenum (2)					
Mo(2)-C(2)		2.067(1)			
Mo(2)-C(1)		2.165(11)			
Mo(2)-C(1)		2.337(11)			
C(2)-Mo(2)-C(1)				109.3(3)	3.452( )
C(2)-Mo(2)-C(1)				133.5(3)	4.048( )
C(2)-Mo(2)-C(1)				102.7(4)	3.518( )

Appendix 2

Fractional Coordinates for the Atoms

Atom Type	x/a*	y/b	z/c	Isotropic B***
Mo(1)	0.8831(2)	0.5	0.2829(3)	0.13(3)
Mo(2)	0.8840(1)	0.1984(1)	0.0372(2)	0.16(3)
Fe(1)	0.0**	0.5	0.0	0.00(5)
Fe(2)	0.2657(3)	0.5	0.2097(4)	-0.03(4)
Fe(3)	0.3600(2)	0.1648(2)	0.6273(3)	-0.03(3)
Fe(4)	0.5	0.3375(3)	0.5	-0.04(4)
Fe(5)	0.3632(3)	0.5	0.6683(4)	-0.04(4)
C(1)	0.3027(11)	0.2513(15)	0.3011(18)	-0.13(14
C(2)	0.0	0.0	0.0	0.36(35)

* ( ) estimated standard deviations

** special positions

*** temperature factors

Appendix 3

Structure Factors

H	K	L	FOBS	FCAL
-15	1	5	1027	954
-14	4	5	605	586
-14	4	4	637	562
-14	4	3	202	139
-14	2	7	1102	969
-14	2	6	888	690
-14	2	5	185	142
-14	2	4	251	158
-14	2	3	337	358
-14	2	2	462	413
-14	0	7	462	380
-14	0	6	894	718
-14	0	5	1545	1323
-14	0	4	251	179
-14	0	3	235	99
-14	0	2	402	338
-14	0	1	1580	1432
-13	1	7	582	519
-13	1	6	203	161
-13	1	5	1008	912
-13	1	4	344	312
-13	1	3	307	221
-13	1	2	1454	1333
-13	1	1	1008	958
-13	1	0	533	507
-13	3	7	241	170
-13	3	6	1367	1247
-13	3	5	1467	1350
-13	3	3	1176	1116
-13	3	2	429	407
-13	5	5	1003	1007
-13	5	3	780	761
-13	5	2	1870	1916
-12	6	5	479	510
-12	6	4	451	435
-12	6	3	1654	1846
-12	6	2	1499	1681
-12	4	7	985	925
-12	4	6	841	820
-12	4	5	980	980
-12	4	4	1684	1684
-12	4	2	403	460
-12	4	1	180	210

H	K	L	FOBS	FCAL
-12	4	0	756	773
-12	2	8	250	178
-12	2	6	2058	1823
-12	2	5	2298	2118
-12	2	3	1385	1280
-12	2	2	1864	1760
-12	2	1	1627	1546
-12	2	0	469	441
-12	0	8	531	401
-12	0	7	1251	1064
-12	0	6	511	402
-12	0	4	1823	1623
-12	0	3	3579	3129
-12	0	2	1489	1380
-12	0	1	1880	1759
-12	0	0	1529	1437
-11	1	8	946	858
-11	1	7	608	553
-11	1	6	1277	1182
-11	1	5	584	519
-11	1	4	390	376
-11	1	3	1298	1240
-11	1	1	196	145
-11	1	0	237	248
-11	3	8	590	480
-11	3	7	2898	2581
-11	3	6	678	631
-11	3	5	1239	1158
-11	3	4	1740	1721
-11	3	3	465	433
-11	3	2	583	553
-11	3	1	1987	2029
-11	3	0	1774	1774
-11	5	7	1189	1205
-11	5	6	1928	1991
-11	5	5	1241	1291
-11	5	4	1058	1141
-11	5	3	1603	1770
-11	5	2	650	678
-11	5	0	417	453
-11	7	5	777	813
-11	7	4	826	891
-11	7	2	646	705

Appendix 3 (continued)

Structure Factors

H	K	L	FOBS	FCAL
-10	8	4	484	568
-10	8	3	1199	1302
-10	6	7	379	376
-10	6	6	411	462
-10	6	5	1916	2054
-10	6	4	1313	1420
-10	6	3	331	294
-10	6	2	327	186
-10	6	1	185	166
-10	4	8	339	351
-10	4	7	1000	1056
-10	4	6	664	666
-10	4	5	430	462
-10	4	3	1418	1538
-10	4	1	514	528
-10	4	0	486	502
-10	2	8	1299	1133
-10	2	7	2384	2113
-10	2	6	534	473
-10	2	5	651	592
-10	2	4	536	477
-10	2	3	1622	1601
-10	2	2	178	143
-10	2	1	1053	1052
-10	2	0	523	547
-10	0	9	1333	1059
-10	0	8	2102	1699
-10	0	6	171	86
-10	0	5	3789	3357
-10	0	4	1696	1569
-10	0	3	433	416
-10	0	1	470	491
-10	0	0	682	706
- 9	1	7	1168	1023
- 9	1	6	844	767
- 9	1	5	638	607
- 9	1	4	828	778
- 9	1	3	1284	1267
- 9	1	2	603	606
- 9	1	0	294	251
- 9	3	8	204	123
- 9	3	7	580	560
- 9	3	4	413	505
- 9	3	3	435	474
- 9	3	2	2772	3093
- 9	3	1	481	484
- 9	3	0	2118	2216
- 9	5	8	551	598
- 9	5	7	1140	1177
- 9	5	6	732	776
- 9	5	5	666	677
- 9	5	4	855	942
- 9	5	3	394	403
- 9	5	2	1015	1148
- 9	5	1	1038	1142
- 9	5	0	948	1050
- 9	7	6	446	446
- 9	7	5	276	304
- 9	7	3	1703	1814
- 9	7	2	426	457
- 9	7	1	1061	1142
- 9	7	0	988	1062
- 8	8	5	664	719
- 8	8	3	1022	1103
- 8	8	2	1686	1818
- 8	8	1	205	141
- 8	6	7	289	306
- 8	6	6	1642	1717
- 8	6	5	372	370
- 8	6	4	1069	1118
- 8	6	3	1374	1425
- 8	6	2	653	721
- 8	6	1	744	766
- 8	6	0	2881	3133
- 8	4	8	585	603
- 8	4	7	1347	1406
- 8	4	6	179	85
- 8	4	5	494	532
- 8	4	4	1358	1442
- 8	4	3	389	399
- 8	4	2	509	552
- 8	4	1	1595	1753
- 8	4	0	1205	1305
- 8	2	8	1074	1015
- 8	2	7	974	919
- 8	2	6	772	715

Appendix 3 (continued)

Structure Factors

H	K	L	FOBS	FCAL
- 8	2	5	1057	1071
- 8	2	3	1049	1109
- 8	2	2	2359	2635
- 8	2	1	195	203
- 8	0	9	650	512
- 8	0	8	1075	936
- 8	0	7	231	154
- 8	0	6	2870	2493
- 8	0	5	621	610
- 8	0	4	2601	2486
- 8	0	3	2706	2661
- 8	0	2	381	385
- 8	0	1	2367	2336
- 8	0	0	4977	4671
- 7	1	9	634	546
- 7	1	8	1044	925
- 7	1	6	2448	2248
- 7	1	5	921	867
- 7	1	4	658	658
- 7	1	3	542	561
- 7	1	2	1569	1656
- 7	1	1	571	600
- 7	1	0	476	516
- 7	3	8	1404	1446
- 7	3	7	1536	1539
- 7	3	6	318	336
- 7	3	5	725	734
- 7	3	4	4611	5079
- 7	3	3	702	710
- 7	3	2	780	809
- 7	3	1	1987	2248
- 7	3	0	383	416
- 7	5	8	180	219
- 7	5	7	939	931
- 7	5	6	2762	2818
- 7	5	5	434	420
- 7	5	4	398	355
- 7	5	3	1545	1559
- 7	5	2	2023	2114
- 7	5	1	195	165
- 7	7	7	1025	1045
- 7	7	6	463	475
- 7	7	5	1995	2136

H	K	L	FOBS	FCAL
- 7	7	4	1729	1807
- 7	7	3	945	1020
- 7	7	1	1204	1329
- 7	7	0	864	918
- 7	9	4	1961	2175
- 7	9	3	1401	1546
- 7	9	2	406	473
- 7	9	1	684	759
- 7	9	0	196	168
- 6	8	6	929	931
- 6	8	5	493	510
- 6	8	4	441	487
- 6	8	3	286	68
- 6	8	1	606	648
- 6	6	7	202	23
- 6	6	6	277	270
- 6	6	5	1397	1460
- 6	6	4	504	522
- 6	6	3	313	349
- 6	6	2	1919	2042
- 6	6	1	1128	1161
- 6	6	0	569	580
- 6	4	8	1061	1087
- 6	4	7	376	333
- 6	4	6	161	249
- 6	4	5	689	690
- 6	4	4	359	372
- 6	4	3	1043	1050
- 6	4	1	919	966
- 6	4	0	879	921
- 6	2	9	361	217
- 6	2	7	1108	1108
- 6	2	6	1424	1472
- 6	2	5	522	512
- 6	2	4	421	425
- 6	2	3	318	53
- 6	2	2	183	146
- 6	2	1	1370	1532
- 6	2	0	327	354
- 6	0	9	580	483
- 6	0	8	4359	3561
- 6	0	7	974	842
- 6	0	6	958	879

Appendix 3 (continued)

Structure Factors

H	K	L	FOBS	FCAL
- 6	0	5	2792	2578
- 6	0	4	1090	1098
- 6	0	3	346	363
- 6	0	2	3264	3239
- 6	0	1	2265	2272
- 6	0	0	581	575
- 5	1	8	710	662
- 5	1	7	498	464
- 5	1	6	220	246
- 5	1	5	1038	1032
- 5	1	4	327	268
- 5	1	3	603	666
- 5	1	2	1461	1648
- 5	1	1	2380	2689
- 5	1	0	607	683
- 5	3	8	1213	1219
- 5	3	7	410	437
- 5	3	6	2496	2490
- 5	3	5	537	506
- 5	3	3	669	700
- 5	3	2	794	800
- 5	3	1	603	577
- 5	3	0	891	1021
- 5	5	8	1044	1118
- 5	5	7	310	195
- 5	5	6	427	421
- 5	5	5	641	668
- 5	5	2	1863	1961
- 5	5	1	2724	2896
- 5	5	0	586	595
- 5	7	7	1059	1138
- 5	7	6	207	161
- 5	7	5	953	986
- 5	7	4	410	430
- 5	7	3	975	1009
- 5	7	2	191	124
- 5	7	1	527	537
- 5	7	0	1807	1920
- 5	9	5	367	413
- 5	9	2	303	295
- 5	9	1	1276	1323
- 5	9	0	392	436
- 4	10	3	1051	1060
- 4	10	2	636	660
- 4	10	1	678	711
- 4	10	0	1492	1459
- 4	8	6	603	602
- 4	8	5	2015	2190
- 4	8	4	396	387
- 4	8	3	571	632
- 4	8	2	1694	1800
- 4	8	1	1817	1936
- 4	8	0	904	937
- 4	6	7	441	462
- 4	6	6	278	288
- 4	6	5	552	559
- 4	6	4	563	585
- 4	6	3	2818	2935
- 4	6	2	1602	1656
- 4	6	0	1568	1625
- 4	4	8	395	343
- 4	4	7	818	819
- 4	4	5	1965	1972
- 4	4	4	1298	1301
- 4	4	3	726	721
- 4	4	1	658	649
- 4	4	0	810	837
- 4	2	7	838	850
- 4	2	6	947	975
- 4	2	5	3170	3279
- 4	2	4	234	54
- 4	2	3	1171	1228
- 4	2	2	2807	3054
- 4	2	1	2569	2843
- 4	2	0	1208	1329
- 4	0	7	558	462
- 4	0	6	366	293
- 4	0	4	365	310
- 4	0	3	5794	5770
- 4	0	2	658	619
- 4	0	1	1126	1314
- 4	0	0	3512	3751
- 3	1	8	374	377
- 3	1	6	1368	1338
- 3	1	5	675	635
- 3	1	4	244	251

Appendix 3 (continued)

Structure Factors

H	K	L	FOBS	FCAL
- 3	1	3	2539	2589
- 3	1	2	699	765
- 3	1	0	159	183
- 3	3	8	397	402
- 3	3	7	2289	2316
- 3	3	6	192	153
- 3	3	5	595	591
- 3	3	4	2714	2670
- 3	3	3	353	379
- 3	3	2	603	541
- 3	3	1	5053	5440
- 3	3	0	1500	1448
- 3	5	7	602	604
- 3	5	6	2015	2069
- 3	5	5	1543	1536
- 3	5	4	1329	1326
- 3	5	3	3014	3083
- 3	5	2	1808	1830
- 3	5	1	731	749
- 3	5	0	753	780
- 3	7	6	240	210
- 3	7	5	917	941
- 3	7	4	1382	1421
- 3	7	2	1042	1078
- 3	7	1	1191	1219
- 3	7	0	1164	1211
- 3	9	5	695	769
- 3	9	4	444	464
- 3	9	3	1047	1056
- 3	9	2	1469	1489
- 3	9	1	1937	1942
- 3	9	0	1528	1513
- 2	10	3	374	369
- 2	10	1	482	443
- 2	8	5	533	592
- 2	8	4	483	543
- 2	8	3	1704	1696
- 2	8	2	1232	1257
- 2	8	1	334	327
- 2	8	0	497	499
- 2	6	6	1289	1338
- 2	6	5	2573	2688
- 2	6	4	474	446
- 2	6	3	1069	1078
- 2	6	2	346	331
- 2	6	0	310	317
- 2	4	7	1057	1067
- 2	4	6	286	302
- 2	4	5	603	566
- 2	4	4	896	894
- 2	4	3	1302	1272
- 2	4	2	1066	1024
- 2	4	1	686	689
- 2	4	0	711	661
- 2	2	8	411	398
- 2	2	7	2768	2777
- 2	2	6	1317	1275
- 2	2	5	639	610
- 2	2	4	1000	942
- 2	2	3	3008	2874
- 2	2	2	1695	1646
- 2	2	1	268	310
- 2	2	0	571	544
- 2	0	8	1685	1502
- 2	0	7	1258	1164
- 2	0	6	844	795
- 2	0	5	4547	4200
- 2	0	4	501	575
- 2	0	3	632	627
- 2	0	2	456	505
- 2	0	0	387	258
- 1	1	8	188	107
- 1	1	7	826	810
- 1	1	6	1095	1091
- 1	1	5	481	417
- 1	1	4	1289	1187
- 1	1	3	1631	1517
- 1	1	2	317	303
- 1	1	1	150	163
- 1	1	0	155	172
- 1	3	7	170	280
- 1	3	6	322	271
- 1	3	5	780	745
- 1	3	4	717	661
- 1	3	3	1458	1324
- 1	3	2	3832	3628

Appendix 3 (continued)

Structure Factors

H	K	L	FOBS	FCAL
-1	3	0	1922	1955
-1	5	7	1281	1318
-1	5	6	1435	1456
-1	5	5	591	595
-1	5	4	714	722
-1	5	3	861	848
-1	5	2	511	532
-1	5	1	931	955
-1	5	0	838	831
-1	7	4	1045	1035
-1	7	3	1349	1339
-1	7	2	358	330
-1	7	1	1008	964
-1	7	0	1465	1413
-1	9	4	531	530
-1	9	3	865	897
-1	9	2	1491	1447
-1	9	1	863	786
0	10	3	1413	1394
0	10	1	1843	1326
0	10	0	2138	2010
0	8	5	750	783
0	8	4	238	275
0	8	2	2416	2355
0	8	1	933	874
0	8	0	276	272
0	6	6	790	842
0	6	5	273	267
0	6	4	643	617
0	6	3	1534	1474
0	6	2	233	50
0	6	1	730	672
0	6	0	4642	4619
0	4	7	815	908
0	4	6	189	222
0	4	5	250	233
0	4	4	1435	1476
0	4	3	1497	1466
0	4	2	1558	1525
0	4	1	1507	1482
0	4	0	2710	2624
0	2	7	720	751
0	2	5	662	653
0	2	4	353	380
0	2	3	403	406
0	2	2	3703	3582
0	2	1	955	958
0	2	0	129	118
0	0	7	702	692
0	0	6	1300	1273
0	0	5	482	458
0	0	4	1710	1616
0	0	3	3903	3529
0	0	2	1052	995
0	0	1	396	496
1	1	7	849	864
1	1	6	2035	2063
1	1	4	987	912
1	1	2	2144	1926
1	1	1	185	171
1	1	0	173	172
1	3	7	1057	1140
1	3	6	739	759
1	3	5	645	619
1	3	4	4667	4695
1	3	3	1261	1254
1	3	2	123	140
1	3	1	3465	3406
1	3	0	1953	1955
1	5	6	2178	2424
1	5	5	987	1027
1	5	3	1280	1300
1	5	2	2634	2603
1	5	1	1260	1269
1	5	0	848	831
1	7	5	1195	1269
1	7	4	1982	2017
1	7	3	1543	1530
1	7	2	418	360
1	7	1	1519	1457
1	7	0	1458	1413
1	9	4	1908	1965
1	9	3	462	475
1	9	2	1256	1215
1	9	1	711	660
2	10	2	540	512

Appendix 3 (continued)

Structure Factors

H	K	L	FOBS	FCAL
2	10	1	1388	1318
2	8	4	805	874
2	8	3	658	671
2	8	2	401	405
2	8	1	634	605
2	8	0	483	499
2	6	5	913	955
2	6	4	1067	1098
2	6	3	784	788
2	6	2	2578	2633
2	6	1	440	411
2	6	0	279	316
2	4	5	998	990
2	4	4	236	236
2	4	3	907	870
2	4	2	350	339
2	4	1	1945	1964
2	4	0	720	661
2	2	7	734	759
2	2	6	1137	1121
2	2	5	721	719
2	2	4	1388	1346
2	2	3	277	294
2	2	2	829	801
2	2	1	937	866
2	2	0	591	544
2	0	7	1619	1618
2	0	6	484	471
2	0	5	2358	2298
2	0	4	2465	2440
2	0	3	549	538
2	0	2	5535	4844
2	0	1	236	356
2	0	0	376	258
3	1	6	185	241
3	1	5	617	607
3	1	3	1031	1036
3	1	2	160	146
3	1	1	3522	3129
3	1	0	152	183
3	3	6	1953	2009
3	3	5	1060	1045
3	3	2	150	187

H	K	L	FOBS	FCAL
3	3	1	294	279
3	3	0	1616	1448
3	5	6	702	708
3	5	4	246	206
3	5	3	955	969
3	5	2	340	329
3	5	1	2651	2709
3	5	0	795	780
3	7	4	470	487
3	7	3	591	639
3	7	2	195	145
3	7	1	1430	1417
3	7	0	1207	1211
3	9	2	189	61
3	9	1	728	698
3	9	0	1542	1513
4	10	1	467	413
4	10	0	1499	1459
4	8	2	1317	1366
4	8	1	1480	1483
4	8	0	926	937
4	6	5	178	103
4	6	4	1460	1531
4	6	3	2032	2048
4	6	2	216	201
4	6	1	953	925
4	6	0	1665	1625
4	4	5	1729	1758
4	4	4	431	436
4	4	3	591	573
4	4	2	315	183
4	4	1	243	204
4	4	0	850	837
4	2	6	652	687
4	2	5	2081	2068
4	2	4	544	538
4	2	3	184	128
4	2	2	1758	1678
4	2	1	2769	2629
4	2	0	1291	1329
4	0	6	573	557
4	0	4	1314	1265
4	0	3	3220	3027

Appendix 3 (continued)

Structure Factors

H	K	L	FOBS	FCAL
4	0	2	548	550
4	0	1	250	333
4	0	0	3849	3751
5	1	6	836	845
5	1	5	607	586
5	1	4	384	382
5	1	3	1949	1843
5	1	2	1206	1190
5	1	1	223	233
5	1	0	689	682
5	3	4	1648	1633
5	3	3	1355	1311
5	3	2	1621	1527
5	3	1	4625	4358
5	3	0	968	1021
5	5	5	1143	1156
5	5	4	498	494
5	5	3	2416	2427
5	5	2	2237	2179
5	5	1	1135	1133
5	5	0	613	595
5	7	2	643	664
5	7	1	1195	1220
5	7	0	1856	1920
5	9	2	2147	2240
5	9	1	1477	1543
5	9	0	413	436
6	8	2	1347	1402
6	8	1	691	736
6	6	4	936	978
6	6	3	811	810
6	6	2	171	138
6	6	1	635	610
6	6	0	567	580
6	4	4	733	721
6	4	3	385	362
6	4	2	532	510
6	4	1	150	89
6	4	0	923	921
6	2	5	735	761
6	2	4	439	391
6	2	3	1837	1807
6	2	2	2130	2093
6	2	1	829	852
6	2	0	358	354
6	0	5	2430	2435
6	0	4	1707	1696
6	0	3	225	97
6	0	2	843	874
6	0	1	1112	1139
6	0	0	594	575
7	1	4	471	510
7	1	3	771	772
7	1	2	167	169
7	1	0	574	516
7	3	4	440	470
7	3	3	1327	1404
7	3	2	877	941
7	3	1	316	321
7	3	0	401	416
7	5	3	851	869
7	5	2	289	285
7	5	1	425	311
7	5	0	226	38
7	7	0	873	917
8	6	2	440	462
8	6	1	1403	1519
8	6	0	2942	3133
8	4	3	1289	1361
8	4	2	759	801
8	4	1	211	228
8	4	0	268	1304
8	2	4	444	458
8	2	3	902	930
8	2	2	1983	1951
8	2	1	1057	1103
8	0	4	353	384
8	0	3	1316	1300
8	0	2	1460	1406
8	0	1	1220	1172
8	0	0	5282	4671
9	1	3	256	220
9	1	2	886	902
9	1	1	242	200
9	1	0	287	251
9	3	3	1651	1716

Appendix 3 (continued)

Structure Factors

H	K	L	FOBS	FCAL
9	3	1	1588	1634
9	3	0	2222	2215
9	5	2	1558	1630
9	5	1	1018	1090
9	5	0	975	1050
9	7	1	1044	1131
9	7	0	993	1062
10	6	1	829	892
10	6	0	172	60
10	4	1	1183	1206
10	4	0	472	502
10	2	2	741	753
10	2	1	313	310
10	2	0	515	548
10	0	2	2456	2303
10	0	1	1696	1536
10	0	0	696	706
11	1	2	691	721
11	1	1	1432	1390
11	1	0	269	247
11	3	0	1766	1774
11	5	0	398	453
12	4	0	713	773
12	2	1	1071	1008
12	2	0	488	441
12	0	1	389	418
12	0	0	1531	1437
13	1	0	522	507

Bibliography

1. J. Stephens, "A Status Review of NASA's COSAM (Conservation of Strategic Aerospace Materials) Program," NASA Tech. Memorandum 82852, May (1982).
2. J. Stephens, "COSAM Program Overview," NASA Tech. Memorandum 83006, October (1982).
3. F. Lemkey, E. Thompson, J. Schuster, and H. Nowotny, "The Quaternary System Fe-Cr-Mn-C and Aligned Superalloys," In Situ Composites IV, p. 31 (1982).
4. J. B. See, "Development in Chromium - 1979", J. of Metals, April (1980).
5. F. Lemkey and H. Nowotny, "Identification of a Cast Iron Alloy Containing Nonstrategic Elements," Contract DEN3-282, (1982).
6. J. van den Boomgaard and L. R. Wolff, Philips Res. Reports 27 509 (1972).
7. M. Hillert and M. Waldenstrom, Calphad, 1, 97 (1977).
8. R. Lundberg, M. Waldenstrom, and B. Uhrenius, Calphad, 159 (1977).
9. S. Shimma, Proc. Imp. Acad. 6, 269 (1929).
10. R. Benz, J. F. Elliot, and J. Chipman, Met. Trans. 4 1975 (1973); 5 2235 (1974).
11. R. Benz, Met. Trans. 5, 2217, 1974.
12. L. R. Woodyatt and G. Krauss, Met. Trans., A. 7A, 983 (1976).
13. L. Brewer, J. Chipman, and S. G. Chang, in Metals Handbook, 8th edition, ASM.
14. J. Beech and D. H. Warrington, J. Iron Steel Inst. 204, 460 (1966).
15. A. Inoue, S. Arakawa, and T. Matsumoto, Trans. JIM 19, 11 (1978).
16. H. C. Eckstrom and W. A. Adcock, J. Amer. Chem. Soc. 72, 1042 (1950).
17. E. R. Thompson and F. D. Lemkey, U. S. Patent 3,671,223, June 20, 1972.
18. J. Van den Boomgaard and A.M.J.G. van Run, "Proc. of Conf. on In Situ Composites," Nat. Acad. Sci., Washington, D. C. NMAB report 208-II, p. 161 (1973).
19. P. N. Quested, D. E. Miles, and M. McLean, Metals Technology, p. 433, November (1980).
20. G. Kirchner and B. Uhrenius, Acta Met., 22, 523 (1974).
21. B. Potůček and Hutnicke Listy, 13, 1070 (1958).
22. E. Rudy, St. Windisch, A. J. Stosick, and R. J. Hoffmann, Trans. Met. Soc. AIME 239, p. 1242 (1967).
23. A. K. Sinha, R. A. Buckley, and W. Hume-Rothery, J. Iron Steel Inst.-London, 205, 191 (1967).
24. R. C. Ruhl and M. Cohen, Trans. AIME 245, 241 (1969).
25. T. Takei and Kinzoku no Kenkyu, 9, 97 (1932).
26. K. Kuo, JISI, t. 173, 363 (1953), and t. 184, 258 (1956).
27. T. Satô, T. Nishizava and T. Tamaki, Trans. Japan Inst. Metals, 3, 196 (1962) and 24, p. 395 (1960).
28. F. E. Bowman and R. M. Parke, Trans. Amer. Soc. Metals, 33, 481 (1944) and 36, 61 (1946).

Bibliography (continued)

29. M. Aldén, S. Asplund, and B. Aronson, J. Iron Steel Inst. (London) 207, 235 (1969).
30. H. Harvig and B. Uhrenius, Rept. TRITA-MAC-0008 Materials Center Royal Inst. Technology, Stockholm, 1971, Metal Science 9, 67 (1975).
31. A. C. Fraker and H. H. Stadelmaier, Trans. Met. Soc. AIME 245, 847 (1969).
32. P. Ettmayer, R. Suchentrunk Mh. Chem. 101, 1098 (1970).
33. W. Jellinghaus, Arch. Eisenhüttenw. 39 705 (1968).
34. R. F. Campbell, S. H. Reynolds, L. W. Ballard, and K. G. Carrol, Trans. Met. Soc. AIME 218, 723 (1960).
35. K. Bungardt, E. Schuermann, H. Preisendanz, P. Schueler, and H. J. Osing, DEW (Deutsch Edelstahlwerke) Tech. Bert. 9, 439 (1969).
36. T. Nishizava, Swedish Council Appl. Res. Rep., 4602, (1967) and T. Nishizava, Scand. J. Met. 1, 41, (1972).
37. T. Wada, H. Wada, J. Elliot, and J. Chipman, Met. Trans., 3, 2865 (1972).
38. S. Wayne and H. Nowotny, Rev. Chimie Minerale, t. 20, 528 (1983).
39. B. D. Craig, Scripta Met., t. 15, 91 (1981).
40. E. Staska, R. Bloch and A. Kulmberg, Mikrochemica Acta, Suppl. 5, 111 (1974).
41. E. Krainer and Berg-u. Huttenm. Mh. 127, 117 (1982).
42. F. D. Lemkey and H. Nowotny, Identification of a Cast Iron Alloy Containing Nonstrategic Elements, UTRC Report R81-915782-1, Contract NASA-DEN3-282 (1981).
43. H. K. Gupta, The Solubility of Transition Metals in M_7C_3 Carbide, Master Thesis, Univ. of Connecticut (1982).
44. F. D. Lemkey and H. Nowotny, Identification of a Cast Iron Alloy Containing Nonstrategic Elements, Contract NASA-DEN3-282 (1981); R82-915782-6, R82-915782-8, R82-915782-9, (1982) also R83-915782-18 (1983).
45. F. D. Lemkey and R. S. Bailey, Second Quarterly Report DEN3-282, United Tech. Research Center, February (1982).
46. W. Jeitschko, H. Nowotny, and F. Benesovsky, Mh. Chem. 94, 247 (1963).
47. H. J. Goldschmidt, Metallurgia, 56, 17 (1957).
48. D. A. Evans and K. H. Jack, Acta Cryst. 10, 769 (1957).
49. D. J. Schmatz, Trans. TMS AIME 215, 112 (1959).
50. Yukawa Tadeda, J. Japan Inst. Met. 21, 275 (1957).
51. K. W. Andrews and P. E. Brookes, Met. Treat. 18, 201 (1951).
52. N. Yu Surovoi, V. I. Alexeev, and L. A. Schwarzman, Dokl. Adad. Nauk SSSR, 157, 951 (1964); Izv. Akad. Nauk. SSSR, Neorg. Mater. 1, 1816 (1965).
53. B. Uhrenius and H. Harvig, Met. Sci. 9, 67 (1975).
54. H. Holleck, Report KfK 3087 B, January (1981), Karlsruhe, GFR.
55. J. C. Schuster and H. Nowotny, unpublished data.
56. V. S. Telegus, Yu. B. Kuz'ma, and M. A. Marko, Porosh. Met. 11, 56 (1971).

Bibliography (continued)

57. J. E Bridge, Jr., G. N. Marinar, and T. V. Philip, Met. Trans. 2, 2209 (1971).
58. W. B. Pearson, A Handbook for Lattice Spacings and Structures of Metals and Alloys, Pergamon, Oxford, (1967).
59. E. Parthé and V. Sadagopan, Acta. Cryst. 16, 202 (1963).
60. E. Rudy, Compendium of Phase Diagram Data, Tech. Rep. AFML-TR-65-2, Part V (1969).
61. F. D. Lemkey, H. Gupta, H. Nowotny, and S. F. Wayne, J. of Mat. Sci. 19 (1984).
62. B. D. Craig, Res. Mech. Letters. t. 1 (1981); Res. Mech. Letters t. 8 (1983), and L. Habraken, Rev. Met. 5. 51 (1954).
63. D. J. Dyson and K. W. Andrews, J.I.S.I., t. 191 (1964) and Acta Cryst. 17 (1964).
64. R. S. Bailey, F. D. Lemkey, and J. Smeggil, Fourth Quarterly Report, NASA Contract DEN3-282 8/15/82; D. L. Anton, Ninth Quarterly Report, NASA Contract DEN3-282, 1/15/84.
65. A. Inoue and T. Matsumoto, Met. Trans. A. 11A, 739 (1980).
66. Ruth Petri, E. Schnabel, and P. Schwaab, Arch. Eisenhüttenw. 52, 2 (1981).
67. D. E. Appleman and H. T. Evans, "Job 9214: Indexing and Least Squares Refinement of Powder Diffraction Data," U. S. Geological Survey, Washington, D. C. (1973).
68. R. S. Bailey, F. D. Lemkey, and H. Nowotny, Third Quarterly Report, NASA Contract DEN3-282, 5/15/82 and Second Quarterly Report 2/15/82.
69. T. Shigematsu, S. Ohmori, N. Nakanishi, and S. Kachi, J. Phys. Soc. Japan, 38 (1975).
70. H. Stuart and N. Ridley, J.I.S.I., July (1966).
71. M. J. Buerger, The Precession Method in X-Ray Crystallography, John Wiley, New York (1964).
72. A. Fernandez Guillermet, Bull. of Alloy Phase Diagrams, 3, 359 (1982); E. K. Storms, E. Rudy et al., J. Chipman, T. Wada, Metals Handbook 8th Edition; C. M. Adam et al. Report FR-13606, United Technologies Corp. Contract Nr. F33615-76-C-5136.
73. S. L. Rice, S. F. Wayne, and H. Nowotny, Mat. Sci. and Eng. 45, 229, (1980) and H. Nowotny, S. L. Rice, and S. F. Wayne, Wear 68, (1981).
74. D. H. Buckley, NASA SP-277, (1971).
75. M. E Garber, I. D. Zeilikman, and I. I. Taypin, Russian Castings Production, 327, (1965).
76. V. Popov and N. Brykov, Russian Castings Production, 330, (1965).
77. R. Richardson, Wear 10, 291, (1967); and Wear 10, 353, 1967.
78. J. Muscara, "A Metallurgical Study of High Stress Abrasion" Doc. Diss. U. Michigan (1971) and T. R. Bates, Jr., "The Influence of Eutectic Carbide Spacing on the Wear of White Iron," Doc. Diss. U. Michigan (1975).
79. T. S. Eyre, R. F. Iles, and D. W. Gasson, Wear 13, 229, (1969); T. S. Eyre and D. Maynard, Wear 18, 301, (1971).
80. E. Takeuchi, Wear 19, 267, (1972).

Bibliography (continued)

81. R. S. Montgomery, Wear 14, 99, (1969).
82. J. Sugishita and S. Fujiyoshi, Wear 66, 209, (1981).
83. P. W. Leach and D. W. Borland, Wear 85, 257, (1983).
84. V. Bankarusamy and Kishore, Wear 86, 173, (1983).
85. W. R. Thorpe and B. Chicco, Mat. Sci. and Eng. 51, 11, (1981).
86. J. T. H. Pearce, Wear 89, 333, (1983).
87. P. J. Blau, Wear 72, 55, (1981), see also Wear 72, 67, (1981).
88. N. P. Suh, Wear 44, 115, (1977).
89. N. Saka, J. J. Paimes-Teixeira, and N. P. Suh, Wear 44, (1977).
90. S. L. Rice, H. Nowotny, and S. F. Wayne, A.S.L.E. Trans. 24, 2, (1981).
91. A. A. Torrance, Wear 50, 169, (1978).
92. T. M. Ahn, P. F. Blau, K. L. Hsu, D. A. Rigney, and F. D. Schell, Wear 409, (1979).
93. L. E. Samuels, J. Inst. of Metals, 85, 51, (1956).
94. N. P. Suh, Wear 56, 423, (1979).
95. J. F. Velez and G. W. Powell, Wear 66, 367, (1981).
96. J. A. Bailey and S. Jeelani, Wear 72, 237, (1981).
97. S. F. Wayne, S. L. Rice, K. Minakawa, and H. Nowotny, Wear 85, 93, (1983).
98. H. Furuichi and H. Yoshida, Wear 50, 357, (1978).
99. Y. Mizutani, Fundamentals of Tribology, edited by N. P. Suh and N. Saka, MIT Press, (1978).
100. S. L. Rice, H. Nowotny, and S. F. Wayne, Wear 74, 131, (1981).
101. P. Heilmann, J. Don, T. C. Sun, D. A. Rigney, and W. A. Glaeser, Wear 91, 171, (1983).
102. D. A. Rigney and W. A. Glaeser, Wear 46, 241, (1978).
103. G. Shaw Scott, J. Inst. of Metals, 12, 2, (1914).
104. E. D. Doyle and D. M. Turley, Wear 51, 269, (1978).
105. W. J. Salesky and G. Thomas, Wear 75, 21, (1982).
106. S. L. Rice, Wear 45, 1, 85 (1977).
107. R. S. Bailey, F. D. Lemkey, and J. Smeggil, "Identification of a Cast Iron Alloy Containing Nonstrategic Elements," Fourth Quarterly Report DEN3-282, UTRC Report R82-915782-12, 1982.
108. R. S. Bailey, F. D. Lemkey, and J. Smeggil, "Identification of a Cast Iron Alloy Containing Nonstrategic Elements," UTRC Report R83-915782-21, 1983.
109. D. L. Anton, "Identification of a Cast Iron Alloy Containing Nonstrategic Elements," Ninth Quarterly Report, UTRC Report R84-916609-3, 1984.

1. Report No.	2. Government Accession No.	3. Recipient's Catalog No.
NASA CR-174900		

4. Title and Subtitle	5. Report Date
Iron-Rich Low-Cost Superalloys	May 1985
	6. Performing Organization Code
7. Author(s)	8. Performing Organization Report No.
Steven F. Wayne	None
	10. Work Unit No.
9. Performing Organization Name and Address	11. Contract or Grant No.
The University of Connecticut Storrs, Connecticut 06108	NAG 3-271
	13. Type of Report and Period Covered
12. Sponsoring Agency Name and Address	Contractor Report
National Aeronautics and Space Administration Washington, D.C. 20546	14. Sponsoring Agency Code
	505-33-1B

15. Supplementary Notes

Final report. Project Manager, Joseph R. Stephens, Materials Division, NASA Lewis Research Center, Cleveland, Ohio 44135. This report was a dissertation submitted in partial fulfillment of the requirements for the degree Doctor of Philosophy to The University of Connecticut.

16. Abstract

An iron-rich low-cost superalloy has been developed in conjunction with United Technologies Research Center under the NASA COSAM Program, Conservation of Strategic Aerospace Materials. The alloy, when processed by conventional chill casting, has physical and mechanical properties that compare favorably with existing nickel and cobalt-based superalloys while containing significantly lower amounts of strategic elements. The composition of the alloy is Cr(15)-Mn(15)-Mo(2)-C(1.5)-Si(1.0)-Nb(1.0)-Fe(bal.), and it can be produced with chromite ore deposits located within the United States. Studies were also made on the properties of Cr(20)-Mn(10)-C(3.4)-Fe(bal.), a eutectic alloy processed by chill casting and directional solidification (D.S.) which produced an aligned microstructure consisting of M_7C_3 fibers in an γ-Fe matrix. This good alignment vanishes when molybdenum or aluminum is added in higher concentrations. Thermal expansion of the M_7C_3 (M = Fe, Cr, Mn) carbide lattice was measured up to 800 °C and found to be highly anisotropic, with the a-axis being the predominant mode of expansion. Repetitive impact-sliding wear experiments performed with the Fe-rich eutectic alloy showed that the directionally solidified microstructure greatly improved the alloy's wear resistance as compared to the chill-cast microstructure and conventional nickel-base superalloys. Studies on the molybdenum cementite phase have proven that the crystal structure of the ξ phase is not orthorhombic. The molybdenum cementite has a monclinic cell (space group C2/m) a = 10.870, b = 7.761, c = 6.563 Å and β = 120.1° with a volume approximately one-fourth the size of the previously proposed cell. The crystal structure of the ξ phase is made up of octahedra building elements consisting of four Mo and two Fe-atoms and trigonal prisms consisting of four Fe and two Mo-atoms. The voids are occupied by carbon atoms. The previous chemical formula for the molybdenum cementite "$MoFe_2C$" is now clearly seen to be $Mo_{12}Fe_{22}C_{10}$.

17. Key Words (Suggested by Author(s))	18. Distribution Statement
Iron-rich; Low-cost; Superalloys; Aligned structure; Eutectic; Manganese; Carbon	Unclassified - unlimited STAR Category 26

19. Security Classif. (of this report)	20. Security Classif. (of this page)	21. No. of pages	22. Price*
Unclassified	Unclassified	168	A08

*For sale by the National Technical Information Service, Springfield, Virginia 22161